Article

Glycerol-driven TNAP activation in thermogenesis and mineralization

https://doi.org/10.1038/s41586-026-10396-9

Received: 27 October 2023

Accepted: 10 March 2026

Published online: 22 April 2026

Check for updates

Mohammed Faiz Hussain[1,2,14], Shreya S. Krishnan[2,3,14], Brittany L. Carroll[2,3,14], Bozena Samborska[1], Aisha Mousa[4,5], Alice Williamson[6,7,8], Maria Delgado-Martin[1,2], Bindu Y. Srinivasu[9], Jakub Bunk[1,2], Janane F. Rahbani[1,10], Abel Oppong[1,2], Anna Roesler[1,2], Zafir Kaiser[1,2], Mina Ersin[1,2], Qiaoqiao Zhang[1,2], Maria Guerra Martinez[1,2], Abhirup Shaw[1,2], Jonathan Cheng[2], Hannah Klemets[2], Katalin Kocsis Illes[2,3], Victoria E. DeMambro[11], Clifford J. Rosen[11], José Luis Millán[12], Thomas E. Wales[9], Claudia Langenberg[6,7,13], Marc D. McKee[3,4,5], Alba Guarné[2,3] & Lawrence Kazak[1,2]✉

Tissue-nonspecific alkaline phosphatase (TNAP) promotes skeletal mineralization by hydrolysing pyrophosphate[1] and has been linked to uncoupling protein 1 (UCP1)-independent adipocyte thermogenesis through the futile creatine cycle through phosphocreatine hydrolysis[2,3]. Despite TNAP's broad physiological roles, endogenous regulators of its activity have not been defined. Furthermore, the activation mechanism of UCP1-independent thermogenesis has remained unresolved. Here we identify glycerol as an allosteric activator of TNAP. Glycerol binds to a surface pocket distal to the active site, which we term the glycerol pocket, to enhance TNAP activity. Using biophysical, structural, bioenergetic and physiological approaches, we show that the glycerol pocket is required for TNAP-driven thermogenesis. Through this mechanism, TNAP activates the futile creatine cycle, acting as a physiological complement to UCP1. The glycerol pocket is likewise required for optimal osteoblast-regulated mineralization. Human missense variants in this site reduce TNAP-dependent mineralization in vitro and are associated with lower alkaline phosphatase activity and bone mineral density, providing genetic evidence that its disruption impairs skeletal physiology.

TNAP hydrolyses diverse phosphorylated substrates[1]. In osteoblasts, TNAP is tethered to the plasma membrane through a C-terminal glycosylphosphatidylinositol (GPI) anchor[1], where its extracellular active site hydrolyses pyrophosphate (PP_i), a potent mineralization inhibitor, to control local inorganic phosphate (P_i) availability for calcium phosphate deposition in the skeleton[4]. Mice deficient in *Alpl*, the gene encoding TNAP, exhibit osteomalacia (soft bones) and reduced survival[5], and humans with *ALPL* mutations can develop hypophosphatasia—a spectrum of mineralization defects ranging from perinatal skeletal failure to adult-onset osteoporosis-like symptoms[6]. In brown adipocytes, mitochondrial-inner-membrane-localized TNAP hydrolyses phosphocreatine (PCr) generated by creatine kinase B (CKB), together driving the futile creatine cycle (FCC)—a creatine phosphorylation–dephosphorylation cycle that accelerates ATP turnover, oxygen consumption and thermogenesis[2,3,7–9]. Adipocyte-specific deletion of *Ckb* or *Alpl* causes susceptibility to diet-induced obesity and impaired glucose homeostasis in mice[3,9]. Notwithstanding its broad relevance, the physiological mechanisms that regulate TNAP activity have remained unclear.

Glycerol activates recombinant TNAP

Thermogenesis is orchestrated by intracellular mediators that relay extracellular cues to effector proteins[10]. While free fatty acids activate UCP1-dependent thermogenesis[11], the mechanisms governing UCP1-independent pathways remain undefined. We therefore examined the FCC. Noradrenergic stimulation of immortalized and primary mouse brown adipocytes induced around 15-fold upregulation of *Alpl* mRNA (Extended Data Fig. 1a), consistent with a role for TNAP in thermogenesis. To identify regulatory metabolites that activate the FCC, we performed metabolomic profiling of brown adipose tissue (BAT) from mice housed at thermoneutrality (30 °C) or exposed to cold (6 °C) for 3 weeks. In total, 32 metabolites were significantly upregulated by cold (Fig. 1a and Supplementary Table 1), including succinate, a known thermogenic regulator[12]. To determine whether candidate metabolites directly regulate TNAP, we purified mature wild-type (WT) and catalytically inactive (S110A) mouse TNAP dimers and removed small molecules by buffer exchange (Extended Data Fig. 1b,c). TNAP activity, measured as P_i release

[1]Rosalind & Morris Goodman Cancer Institute, McGill University, Montreal, Quebec, Canada. [2]Department of Biochemistry, McGill University, Montreal, Quebec, Canada. [3]Centre de Recherche en Biologie Structurale, McGill University, Montreal, Quebec, Canada. [4]Faculty of Dental Medicine and Oral Health Sciences, McGill University, Montreal, Quebec, Canada. [5]Department of Anatomy and Cell Biology, McGill University, Montreal, Quebec, Canada. [6]Precision Healthcare University Research Institute, Queen Mary University of London, London, UK. [7]Computational Medicine, Berlin Institute of Health at Charité—Universitätsmedizin, Berlin, Germany. [8]Friede Springer Cardiovascular Prevention Center at Charité, Charité University Medicine Berlin, Berlin, Germany. [9]Department of Chemistry and Chemical Biology, Northeastern University, Boston, MA, USA. [10]Department of Medicine, University of Chicago, Chicago, IL, USA. [11]Maine Health Institute for Research, Scarborough, ME, USA. [12]Sanford Burnham Prebys Medical Discovery Institute, La Jolla, CA, USA. [13]Max Planck Institute for Molecular Genetics Berlin, Berlin, Germany. [14]These authors contributed equally: Mohammed Faiz Hussain, Shreya S. Krishnan, Brittany L. Carroll. ✉e-mail: lawrence.kazak@mcgill.ca

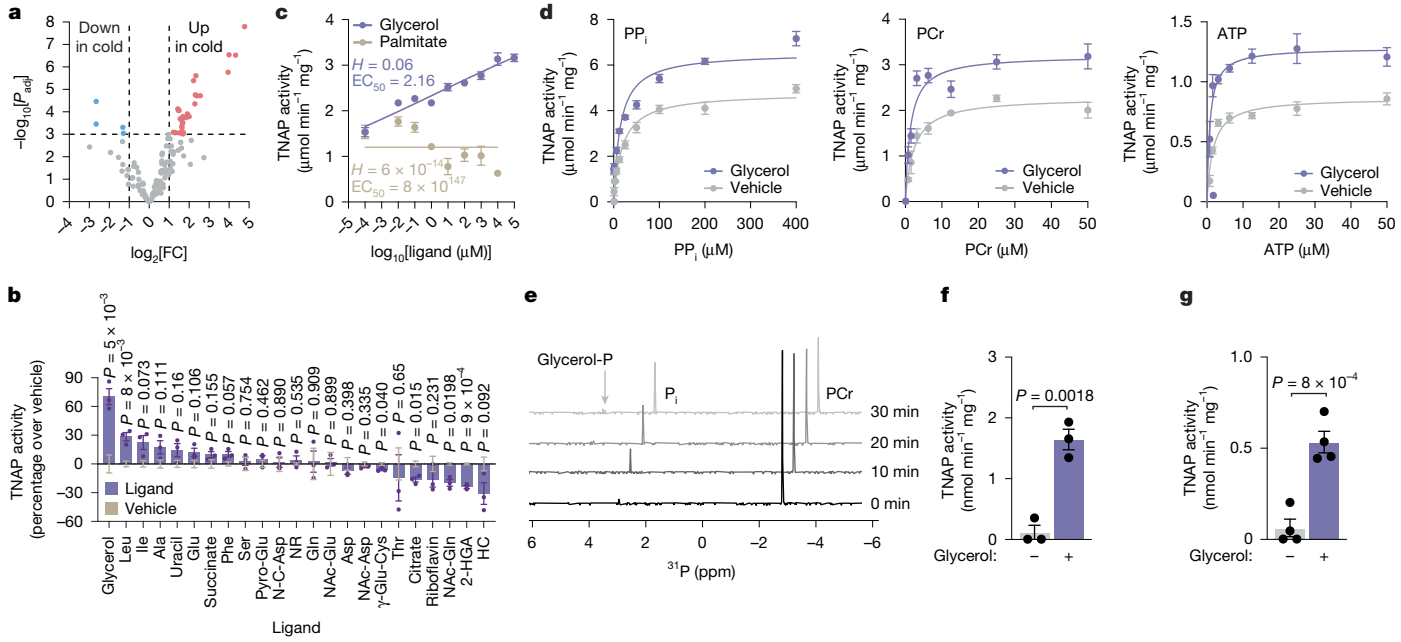

Fig. 1 | Activation of TNAP by glycerol. a, Cold-regulated metabolites in BAT. Data are shown for biologically independent mice ($n = 5$ per group). **b**, Ligand-induced (1 mM) hydrolysis of PCr (3 μM) by recombinant WT mouse TNAP. Data are shown for independent in vitro reactions ($n = 3$ per group). Pyro-Glu, pyroglutamate; *N*-C-Asp, *N*-carbamoyl aspartic acid; NR, nicotinamide riboside; NAc-Glu, *N*-acetyl glutamic acid; γ-Glu-Cys, γ-glutamate-cysteine; NAc-Gln, *N*-acetyl glutamine; 2-HGA, 2-hydroxyglutaric acid; HC, homocitrate. **c**, Hydrolysis of PCr by recombinant WT mouse TNAP. Data are shown for independent in vitro reactions ($n = 3$ per group). **d**, Glycerol-induced (1 mM) hydrolysis of PP_i, PCr and adenosine triphosphate (ATP) by recombinant WT mouse TNAP. Data are shown for independent in vitro reactions ($n = 3$ per group). **e**, PCr hydrolysis and P_i accumulation by recombinant WT mouse TNAP measured by ^{31}P NMR. **f**,**g**, Glycerol-induced (1 mM) PCr hydrolysis in intact mouse (**f**) and human (**g**) brown adipocyte mitochondria mediated by endogenous TNAP, defined as the portion of hydrolysis inhibited by SBI-425 (10 μM) at pH 7.2. Data are shown for biologically independent mitochondrial preprations ($n = 3$ (mouse) and $n = 4$ (human) per group). Error bars represent mean ± s.e.m. **a**, Nominal *P* values were adjusted for multiple comparisons using the Benjamini–Hochberg false-discovery rate method. Statistical analysis was performed using multiple two-tailed Student's *t*-tests (**b**), nonlinear regression (**c** and **d**) and two-tailed Student's *t*-tests (**f** and **g**).

from PCr, was abolished by a specific TNAP inhibitor (Extended Data Fig. 1d) and was absent in the catalytically inactive mutants (S110A, D60A and T167R) despite normal expression and folding (Extended Data Fig. 1e,f), validating the assay specificity. Phosphorylated metabolites were excluded as candidate regulators because they acted as TNAP substrates (Extended Data Fig. 1g). Among non-phosphorylated candidates, glycerol was the most potent TNAP activator in an enzyme-linked assay using purine nucleoside phosphorylase (PNP) as the coupling enzyme (Fig. 1b). Glycerol did not affect PNP activity, confirming the assay specificity for TNAP (Extended Data Fig. 1h,i). Noradrenergic stimulation increased intracellular glycerol in cultured brown adipocytes (Extended Data Fig. 1j and Supplementary Table 2). Glycerol, but not palmitate (another lipolytic product), stimulated TNAP-mediated PCr hydrolysis in a dose-dependent manner (Fig. 1c), an effect that was reproduced with isotopically labelled glycerol (Extended Data Fig. 1k,l). Glycerol also increased TNAP-dependent PP_i hydrolysis (Extended Data Fig. 1m). TNAP turnover (k_{cat}) was highest for PP_i, followed by PCr and ATP (Fig. 1d and Extended Data Fig. 1n). Catalytic efficiency (k_{cat}/K_M) was highest for PCr and was increased by glycerol across all substrates (Extended Data Fig. 1n). Recombinant human TNAP was similarly activated (Extended Data Fig. 1o). Although phosphate acceptors can accelerate TNAP activity in vitro[13], ^{31}P nuclear magnetic resonance (NMR) demonstrated that glycerol does not function as a phosphate acceptor (Fig. 1e and Extended Data Fig. 1p). We therefore conclude that glycerol acts as a signalling metabolite that enhances TNAP activity.

Glycerol activates mitochondrial TNAP

Recombinant TNAP lacks GPI anchoring, carries distinct glycosylation and contains a C-terminal His tag, features that may influence activity[14]. We therefore examined endogenous TNAP in BAT mitochondria, where it has been proposed to localize to the inner membrane[3]. Glycerol increased native TNAP-dependent PCr hydrolysis by around tenfold in intact mouse and human brown adipocyte mitochondria and in mitochondrial lysates (Fig. 1f,g and Extended Data Fig. 1q,r). Gas chromatography coupled with mass spectrometry (GC–MS) analysis confirmed the presence of glycerol within rapidly purified mitochondria (Extended Data Fig. 1s,t), indicating that mitochondrial TNAP can encounter glycerol in cells.

Glycerol drives futile creatine cycling

We next established an enzyme-linked assay coupling the FCC effectors (CKB and TNAP) to NADH oxidation, such that creatine-stimulated NADH oxidation reports CKB-dependent flux, whereas PCr-driven oxidation strictly requires both CKB and TNAP, together providing a functional readout of FCC activity (Fig. 2a). Glycerol was required for PCr to stimulate NADH oxidation in BAT mitochondria but had no effect in heart or liver (Fig. 2b), probably attributable to the absence of mitochondrial TNAP (Extended Data Fig. 2a–c). Glycerol amplified the super-stoichiometric effect of creatine on ATP turnover, as measured by oxygen consumption and NADH oxidation (Fig. 2c,d), supporting glycerol-dependent TNAP activation that enhances FCC-driven thermogenesis.

As CKB is essential for the FCC[9], we validated our enzyme-linked assay using genetic rescue in *Ckb*$^{-/-}$ brown adipocytes expressing either green fluorescent protein (GFP), WT CKB, a non-mitochondrial variant (CKB(ΔiMTS-L))[9] or a catalytically inactive mutant (CKB(C283S))[15] (Fig. 2e,f). In mitochondrial extracts, creatine and PCr stimulated NADH oxidation in control *Ckb*$^{fl/fl}$ adipocytes and in *Ckb*$^{-/-}$ adipocytes restored

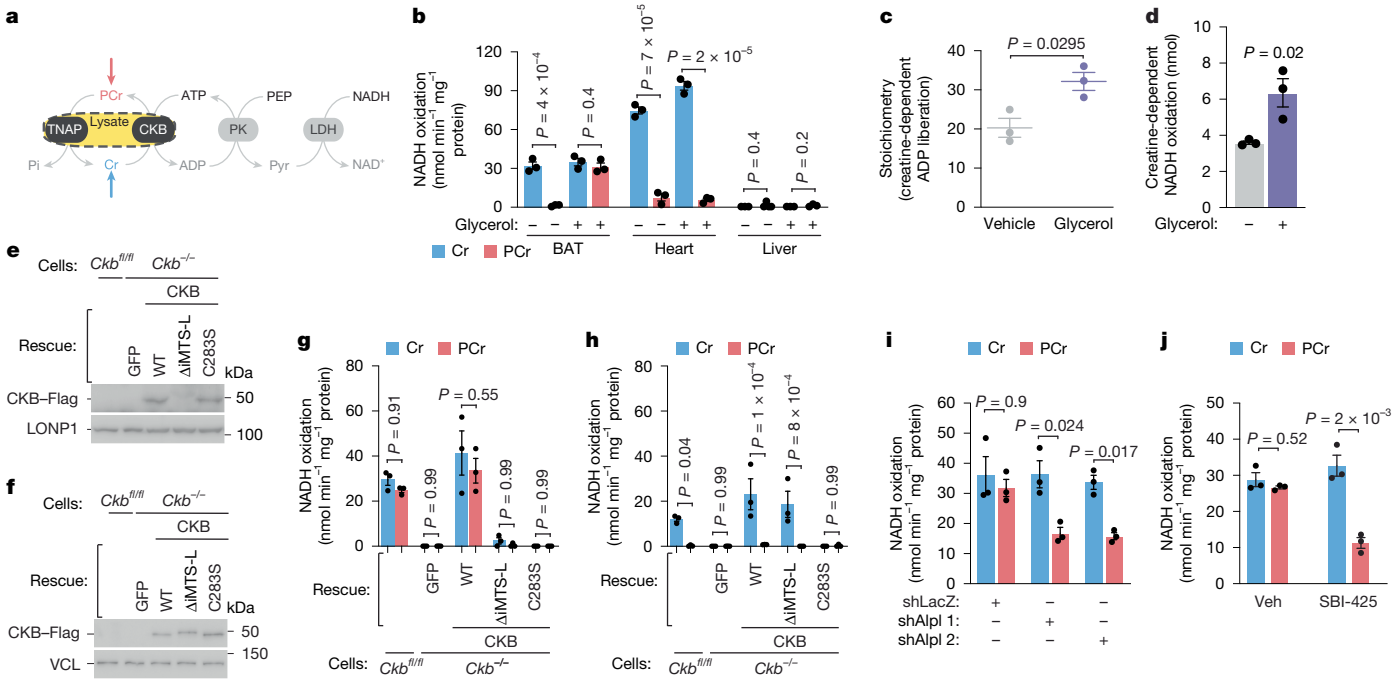

Fig. 2 | Acceleration of the FCC by glycerol. a, Schematic of the enzyme-linked assay used to measure the FCC. **b**, Creatine (Cr)- and PCr-driven NADH oxidation in mitochondrial lysates at pH 7.2. Data are shown for biologically independent mitochondrial preparations ($n = 3$ per group and tissue, except for the liver PCr group, for which $n = 4$). **c**, Stoichiometry of ADP release (calculated using a P/O ratio of 2.7) in response to 10 µM creatine, measured by respirometry (O_2 consumption). Data are shown for biologically independent mitochondrial preparations ($n = 3$ per group). **d**, NADH oxidation from mitochondrial lysates in response to 2 nmol creatine. Data are shown for biologically independent mitochondrial preparations isolated from immortalized brown adipocytes ($n = 3$ per group). **e**,**f**, Western blots of protease-protected mitochondrial (**e**) and cytosolic (**f**) lysates from in vitro differentiated immortalized brown adipocytes. **g**–**j**, Creatine- and PCr-driven NADH oxidation in mitochondrial lysates (from **e**) (**g**), cytosolic lysates (from **f**) (**h**), mitochondrial lysates from *Alpl*-silenced brown adipocytes (from Extended Data Fig. 2d,e) (**i**) and brown adipocyte mitochondrial lysates with or without SBI-425 (10 µM) (**j**). Data are shown for biologically independent mitochondrial preparations ($n = 3$ per group). Data are mean ± s.e.m. of biologically independent samples. Statistical analysis was performed using multiple two-tailed Student's *t*-tests (**b**), two-tailed Student's *t*-tests (**c** and **d**), two-way analysis of variance (ANOVA) with Šidák post hoc test (**g** and **h**) and two-way ANOVA with Tukey's post hoc test (**i** and **j**).

with WT CKB (Fig. 2g). In cytosol, creatine, but not PCr, stimulated NADH oxidation in control *Ckb*$^{fl/fl}$ adipocytes and in *Ckb*$^{-/-}$ adipocytes expressing WT CKB or CKB(ΔiMTS-L) (Fig. 2h). No activity was detected in *Ckb*$^{-/-}$ adipocytes expressing GFP or CKB(C283S). Thus, active mitochondrial CKB is required for FCC activity.

Alpl silencing in brown adipocytes reduced mitochondrial TNAP protein levels without affecting CKB expression (Extended Data Fig. 2d,e). In the enzyme-linked FCC assay, glycerol enhanced creatine-driven NADH oxidation in a TNAP-dependent manner (Extended Data Fig. 2f). Consistent with this requirement, TNAP was enriched in mitochondria (Extended Data Fig. 2g). Genetic or pharmacological TNAP inhibition selectively impaired PCr-stimulated, but not creatine-stimulated, NADH oxidation in mitochondria (Fig. 2i,j); by contrast, in cytosol, creatine stimulated NADH oxidation, whereas PCr had no effect (Extended Data Fig. 2h). Together, these findings demonstrate that mitochondrial CKB and TNAP are jointly required for FCC activity and that glycerol accelerates the cycle by enhancing TNAP-mediated PCr hydrolysis.

Structural basis for TNAP activation

To define the structural basis of glycerol-mediated activation, we solved the crystal structure of catalytically inactive mouse TNAP(S110A) bound to PCr and glycerol at a resolution of 2.3 Å. TNAP formed a canonical alkaline phosphatase dimer virtually identical to human TNAP[16] (root mean square deviation of 0.37 Å across 3,118 atoms) (Fig. 3a and Supplementary Table 3). The Ca^{2+}-binding site displayed octahedral coordination by Glu235 (α9–α10 loop), Glu291, Asp306, the carbonyl oxygen of Phe290 (β6–α12 loop) and one water molecule (Fig. 3b). The first metal binding site (M1) contained Zn^{2+} coordinated by Asp337 and His341 (α13), His454 (β10–β11 loop) and the PCr phosphate. The second site (M2) contained Mg^{2+} coordinated by Asp378 and His379 (β8–β9 loop) together with the PCr phosphate. In TNAP(S110A), the β-carbon of Ala110 is 3.4 Å away from M2, which is comparable to WT TNAP but prevents the formation of a competent active site. Anomalous difference maps at the Zn^{2+} edge confirmed the identities of the M1 and M2 metals (Extended Data Fig. 3a). The third metal site (M3) lacked density, consistent with previous evidence of exchange at this position[17,18]. The presence of Mg^{2+} rather than Zn^{2+} in M2 probably reflects weakened coordination in catalytically dead TNAP(S110A) together with the phosphate-rich crystallization conditions that readily chelate free Zn^{2+} ions[19]. PCr bound through its phosphate, coordinating M1 and M2, forming a salt bridge with Arg184 (α6–α7 loop), and approaching Asp337 (β8–β9 loop) and His454 (β10–β11 loop) for potential hydrogen bonding (Fig. 3c). ATP- and PPi-bound TNAP(S110A) structures exhibited similar phosphate coordination without additional stabilizing interactions (Extended Data Fig. 3b and Supplementary Table 3). The creatine moiety occupied a surface groove between the crown domain and TNAP core with weak density indicating conformational flexibility (Fig. 3a and Extended Data Fig. 3b), consistent with broad substrate specificity.

We identified five glycerol molecules bound per TNAP dimer (Extended Data Fig. 3c). One bound to a single protomer, and was a crystallography artefact; mutation of its anchoring residue (TNAP(D248A)) did not affect glycerol-stimulated activity (Extended Data Fig. 3d). The remaining four glycerol molecules bound to two identical sites on both protomers. One pair occupied a shallow pocket at the crown

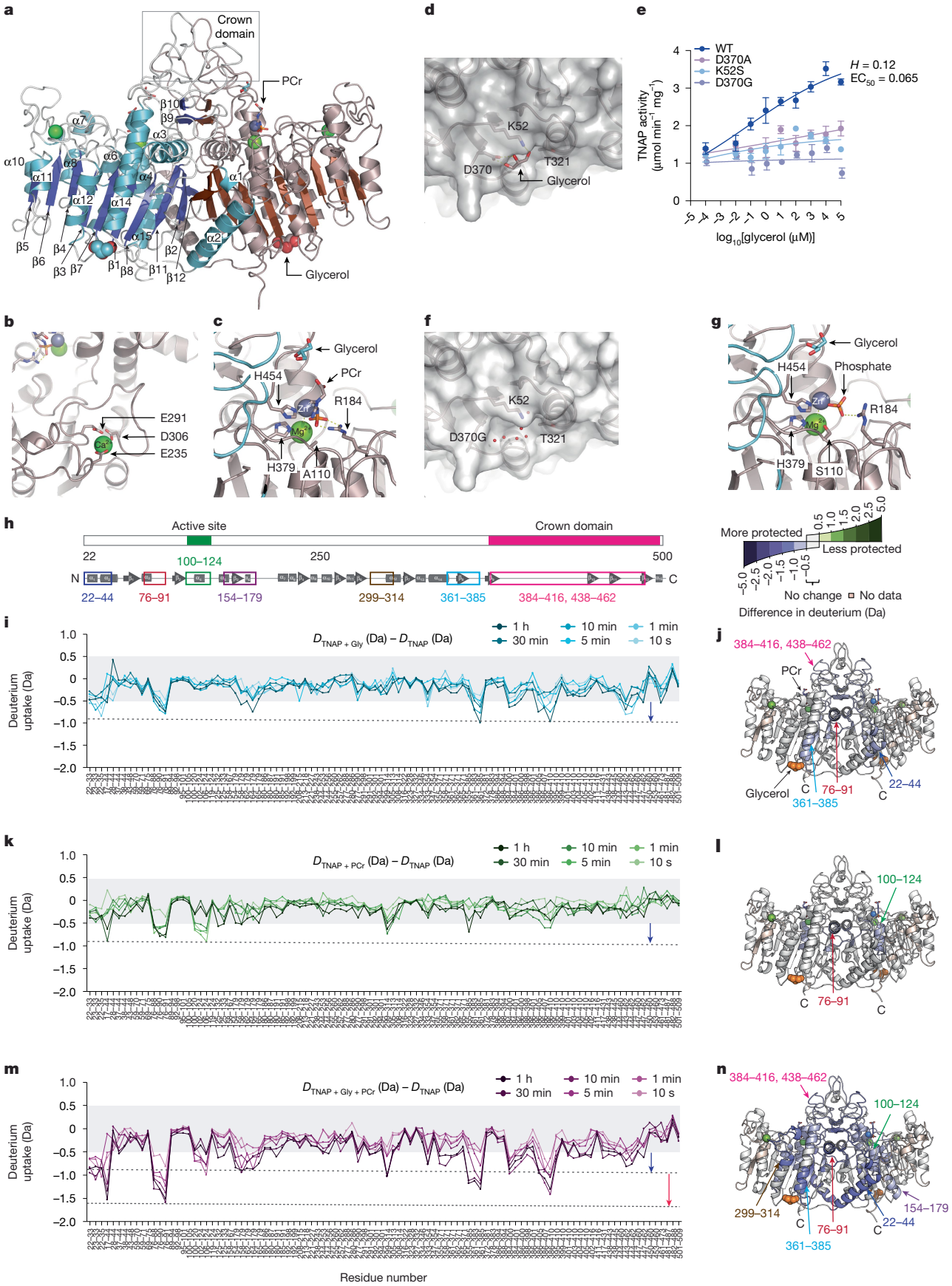

Fig. 3 | See next page for caption.

Fig. 3 | The structural basis of glycerol activation and substrate-induced changes in TNAP backbone dynamics. a, Ribbon diagram of the TNAP(S110A) dimer bound to PCr and glycerol, with protomers shown in different colours; PCr is shown as sticks, and glycerol and metal ions are shown as spheres. **b**, Magnified view of the Ca^{2+}-binding site; coordinating side chains are shown as sticks. **c**, The TNAP(S110A) active site bound to PCr, highlighting coordination of the two metal ions and the glycerol molecule bound at the base of the crown domain. **d**, Magnified view of the glycerol pocket in TNAP(S110A) crystallized with PCr in the presence of glycerol, shown as a semitransparent surface over the ribbon diagram; glycerol and coordinating residues are labelled and shown as sticks. **e**, Glycerol-induced PCr hydrolysis by recombinant WT TNAP and TNAP(D370G), TNAP(D370A) and TNAP(K52S) variants. Data are shown for independent in vitro reactions ($n = 3$ per group). **f**, Magnified view of the glycerol pocket in TNAP(D370G) bound to PCr and crystallized with glycerol, shown in the same orientation and style as in **d**; water molecules lining the pocket are shown as red spheres. **g**, Magnified view of the TNAP(D370G) active site bound to PCr in the presence of glycerol, with the phosphate ion generated by PCr hydrolysis shown as sticks, in the same orientation and style as in **c**. **h**, Linear map showing key regions and secondary structural elements of TNAP. **i**,**k**,**m**, HDX MS difference profiles showing the relative differences in deuterium incorporation (*D*) between two states. TNAP + glycerol versus TNAP (**i**), TNAP + PCr versus TNAP (**k**) and TNAP + glycerol + PCr versus TNAP (**m**). **j**,**l**,**n**, Regions of HDX differences at 10 min are shown on the cartoon structure of TNAP and coloured according to the scale shown, showing the effect of glycerol (**j**), PCr (**l**) and glycerol + PCr (**n**). Error bars represent mean ± s.e.m. Statistical analysis was performed using nonlinear regression (**e**).

domain base near the dimer interface and adjacent to the active site, contacting Asp404 of one protomer and the main chain of His451 of the other (Extended Data Fig. 3c). Mutation of Asp404 (TNAP(D404A)) abolished catalytic activity (Extended Data Fig. 3e,f), and analysis using hydrogen-deuterium exchange MS (HDX-MS) indicated a more dynamic and destabilized conformation (Extended Data Fig. 3g and Supplementary Table 4). The second glycerol pair occupied a conserved distal surface pocket adjacent to the GPI anchor, defined by Lys52, Thr321 and Asp370 (Fig. 3a,d). Glycerol formed hydrogen bonds with the side chains of Asp370 and Lys52 and the backbone nitrogen of Ser367. Notably mutation of Asp370 or Lys52 abolished glycerol-stimulated PCr hydrolysis without affecting basal activity (Fig. 3e), identifying this distal pocket as necessary for inducible activation. We next solved the crystal structure of TNAP(D370G) bound to PCr at a resolution of 2.1 Å. This structure revealed water molecules, but not glycerol, in this cavity, despite crystallization in the presence of glycerol (Fig. 3f and Supplementary Table 3). By contrast, glycerol persisted at the crown domain base of TNAP(D370G) (Fig. 3g), indicating that this site does not mediate inducible enzyme activation. The TNAP(D370G) active site remained intact and phosphate bound (Fig. 3g) but was more open than catalytically inactive TNAP(S110A), with Arg184 side-chain displacement shifting the phosphate 1.2 Å from the metals, disrupting the PCr salt bridge and potentially facilitating phosphate release after hydrolysis (Extended Data Fig. 3h).

Collectively, our data indicate that the distal GPI anchor-adjacent surface pocket is the site where glycerol binds to mediate inducible TNAP activation. Whereas WT TNAP binds to glycerol at this site and is activated, TNAP(D370G) neither binds to nor responds. On this basis, we designate this distal site as the allosteric glycerol pocket—a control node for TNAP activity. The specificity of this activation was notable. Neither protein-stabilizing cosolvents nor closely related metabolites (glyceraldehyde, glyceric acid or ethylene glycol) activated TNAP (Extended Data Fig. 3i–k). Moreover, the glycerol pocket contained only water molecules when glycerol was replaced by ethylene glycol as the cryoprotectant (Extended Data Fig. 3l and Supplementary Table 3). Thus, glycerol activates TNAP through specific binding at a distal allosteric site.

Additive allosteric reduction of HDX

HDX-MS analysis of WT TNAP with glycerol, PCr or both revealed localized changes in deuterium incorporation that mapped to regions proximal and distal to the glycerol pocket. A schematic of TNAP is shown for reference (Fig. 3h), with the regions affected by deuterium exchange modelled onto the structures we solved (Fig. 3i–n and Supplementary Table 4). Glycerol alone modestly stabilized (decreased HDX) segments at the N terminus (α1–α2, amino acids Lys22–Gln44), α3–β2 (amino acids Gln76–Lys91), α5–β3 (amino acids Ala154–Ala179), α13–β8 (amino acids Lys361–Phe385) and the crown domain (amino acids Thr384–Gly416 and amino acids His438–Phe462) (Fig. 3i,j). PCr alone stabilized the loop connecting α3–β2 (amino acids Gln76–Lys91), the active site (amino acids Thr100–Asn124) and β6–α12 (amino acids Leu299–Glu314) (Fig. 3k,l). Notably, combined glycerol and PCr produced additive reductions in exchange across all regions affected individually (Fig. 3m,n).

The HDX-MS profiles of TNAP in the presence of glycerol reveal several structural insights. The very mild decreases in exchange at the Lys22–Gln44, Gln76–Lys91 and Ala154–Ala179 regions, and the crown domain occur at sites distant from the glycerol pocket. By contrast, reduced HDX at α13–β8 (amino acids Lys361–Phe385), which lies adjacent to the glycerol pocket, points to a localized effect of ligand binding. These findings indicate that glycerol binding induces coordinated changes in backbone dynamics across both proximal and distal regions, consistent with allosteric regulation of TNAP activation. PCr binding alone produced additional alterations, yet the Gln76–Lys91 loop was consistently affected by both glycerol and PCr despite their distinct binding sites, suggesting that this region may serve as a key regulatory element. Moreover, reduced HDX at the N terminus and crown domain supports their roles as potential allosteric hubs transmitting conformational signals from glycerol and PCr binding. Thus, these coordinated alterations in backbone dynamics suggest that TNAP activation by glycerol is mediated by a reduction in conformational flexibility that stabilizes an activation-competent state.

Quantifying the FCC

The quantitative contribution of UCP1-independent thermogenesis has not been defined. Thus, we set out to measure the quantitative contribution of the FCC to energy expenditure using isolated mitochondria, intact brown adipocytes and in vivo physiological conditions. In mitochondria isolated from cultured brown adipocytes, glycerol markedly amplified creatine-dependent ADP-driven respiration and was required for creatine to elicit a sustained respiratory response (Extended Data Fig. 4a–d)—a defining feature of an energy-dissipating thermogenic pathway. When glycerol was present, TNAP inhibition specifically reduced ADP-stimulated respiration only in the presence of creatine (Extended Data Fig. 4e–g), but not in its absence (Extended Data Fig. 4e,f,h). This specificity demonstrates that TNAP preferentially hydrolyses PCr rather than ATP to drive the FCC. From these assays, we quantified an FCC activity of 5.0 ± 2.1 nmol min^{-1} mg^{-1} mitochondrial protein, representing the TNAP-dependent portion of the sustained respiratory response that was driven by creatine (Extended Data Fig. 4i,j). By comparison, UCP1-dependent respiration was 12.4 ± 3.4 nmol min^{-1} mg^{-1} mitochondrial protein (Extended Data Fig. 4k), indicating that the FCC provides around 40% of the thermogenic capacity relative to UCP1 in cultured brown adipocyte mitochondria. This value is probably conservative, as UCP1-dependent respiration was measured in the absence of purine nucleotides, which physiologically inhibit UCP1 and must be displaced by fatty acids during thermogenic activation.

To assess the FCC under physiologically relevant conditions, we quantified glycerol and creatine concentrations in BAT from mice

acclimatized to 30 °C or 6 °C, correcting for adipocyte diameter[20], adipocyte number[21] and tissue mass (Extended Data Fig. 5a). GC–MS analysis showed that glycerol levels ranged from 0.24 to 17.9 mM, increasing with cold exposure (Extended Data Fig. 5b,c) and falling within the range of concentrations that activate recombinant TNAP (Fig. 1c, Extended Data Figs. 1m and 3i,k). Creatine levels were then measured in vivo, where cellular levels are regulated by import through solute carrier family 6 member 8 (SLC6A8) and synthesis through glycine amidinotransferase (GATM)[22,23] (Extended Data Fig. 5d). To isolate the adipocyte-specific pool, we constructed adipocyte-selective *Slc6a8;Gatm* double-knockout (*Slc6a8;Gatm*$^{Adipoq\text{-}cre}$) mice and quantified creatine levels in the BAT relative to the controls. As expected, double-knockout mice exhibited reduced *Slc6a8* and *Gatm* mRNA levels in the BAT (Extended Data Fig. 5e). Liquid chromatography coupled with MS (LC–MS) analysis, based on the differential creatine abundance in BAT between double-knockout (*Slc6a8;Gatm*$^{Adipoq\text{-}cre}$) mice and littermate controls, revealed that parenchymal brown adipocytes contained 0.23 to 5.62 mM creatine, again with higher concentrations under cold conditions (Extended Data Fig. 5f–h).

Next, we quantified UCP1-dependent thermogenesis in BAT mitochondria to be 95.6 ± 12.2 nmol min^{-1} mg^{-1} mitochondrial protein, consistent with previous reports using identical substrates[24] (Extended Data Fig. 6a). In GDP-containing preparations, titration of the protonophore cyanide 4-trifluoromethoxy phenylhydrazone (FCCP) induced respiration comparable to purine nucleotide omission (Extended Data Fig. 6b), and around 25% of protonophore-stimulated respiration remained ADP-coupled, consistent with published values[25] (Extended Data Fig. 6c,d). Having confirmed the quality of our preparations, we modelled FCC activity under physiological thermogenic conditions, using moderate (mid-range) concentrations of glycerol (5 mM) and creatine (3 mM) concentrations measured in cold-acclimatized brown adipocytes (Extended Data Fig. 5c,h). Creatine potentiated ADP-dependent respiration, and TNAP inhibition selectively abolished the creatine-dependent sustained respiratory response, yielding an FCC rate of 5.7 ± 0.8 nmol min^{-1} mg^{-1} mitochondrial protein (Fig. 4a–c and Extended Data Fig. 6e). ADP-stimulated respiration in the absence of creatine was unaffected by TNAP blockade (Extended Data Fig. 6e), confirming FCC specificity. Physiologically, free fatty acids released during lipolysis must overcome purine nucleotide inhibition, particularly by ATP, to engage UCP1-dependent leak respiration[11]. To model this, we used GDP as a surrogate for ATP, at concentrations approximating those in thermogenically activated brown adipocytes[24,26,27], together with free palmitate levels reported to drive proton leak during thermogenesis[27]. This yielded fatty-acid-induced respiration rates ranging from 9.8 ± 1.9 nmol min^{-1} mg^{-1} to 25.0 ± 2.8 nmol min^{-1} mg^{-1} mitochondrial protein (Fig. 4d), with peak responses matching previous reports[11,24,28–33]. Under these conditions, FCC capacity reaches levels corresponding to around 23–37%, 25–50% and 40–60% of fatty-acid-induced leak respiration at 1, 3 and 5 mM GDP, respectively. These values align with recent in vivo studies demonstrating that the FCC operates alongside UCP1 and can independently sustain a substantial fraction of cellular and whole-body thermogenesis even in the absence of UCP1 (refs. 7,34).

FCC requires the TNAP glycerol pocket

To determine the contribution of the glycerol pocket to FCC-dependent thermogenesis, we engineered *Alpl*-deficient (knockout (KO)) brown adipocytes lacking TNAP activity (Extended Data Fig. 7a,b) and reintroduced into these cells (through adenoviral infection) either WT, catalytically dead (S110A) or allosteric glycerol pocket mutants (D370G and K52S) of TNAP (Extended Data Fig. 7c). After mitochondrial isolation (Fig. 4e), respirometry revealed that FCC-driven thermogenesis required TNAP activity and glycerol coordination by Asp370 or Lys52 (Fig. 4f). Consistently, glycerol-induced PCr hydrolysis was observed only in control *Alpl*$^{fl/fl}$ brown adipocytes and in *Alpl*$^{-/-}$ brown adipocytes restored with WT TNAP, and not with catalytically inactive TNAP(S110A) or TNAP with allosteric glycerol pocket mutants (K52S or D370G) (Extended Data Fig. 7d). BAT glycerol levels were comparable between mice lacking *Alpl* in adipose tissue (*Alpl*$^{Adipoq\text{-}cre}$) and littermate control (*Alpl*$^{fl/fl}$) mice (Extended Data Fig. 7e), indicating that TNAP does not regulate glycerol abundance in bulk tissue.

To investigate how thermogenic adipocytes support glycerol-driven FCC activation, we introduced empty adeno-associated virus (AAV) or TNAP variants (WT, S110A, K52S and D370G) into the BAT of mice genetically lacking *Alpl* in adipose tissue (*Alpl*$^{Adipoq\text{-}cre}$). In acutely purified mature brown adipocytes (Fig. 4g), TNAP variants were similarly expressed, with glycerol pocket mutants expressed at slightly higher levels, and UCP1 levels were comparable across groups (Extended Data Fig. 7f). Cells expressing WT TNAP exhibited significantly greater noradrenaline-stimulated thermogenesis compared with either control condition—empty AAV or the catalytically inactive TNAP(S110A) mutant, which were indistinguishable from one another—while basal and leak respiration were unchanged (Extended Data Fig. 7g–i). In WT-TNAP cells, around 40% of the noradrenaline response was ATP-linked, an effect similarly blunted in both empty AAV- and TNAP(S110A)-expressing cells (Extended Data Fig. 7j). To isolate the TNAP-dependent thermogenic contribution, we subtracted residual ATP-dependent oxygen consumption measured in empty AAV-infected cells, which matched responses in TNAP(S110A)-expressing cells (Extended Data Fig. 7j). As the TNAP glycerol-pocket mutants (D370G, K52S) retained substantial basal catalytic activity, whereas TNAP(S110A) and empty AAV had none (Extended Data Fig. 7k), we normalized respiratory responses to glycerol-independent TNAP activity to control for differences in rescued TNAP variant expression. Glycerol-pocket mutants exhibited a >90% reduction in TNAP-mediated thermogenesis, comparable to catalytically inactive S110A or empty AAV controls, and markedly lower than TNAP-WT rescue and endogenous TNAP controls (*Alpl*$^{fl/fl}$), which were indistinguishable from one another (Fig. 4h). Noradrenaline-stimulated lipolysis and mitochondrial targeting were unchanged across TNAP variants (Extended Data Fig. 7l–n), indicating that noradrenaline engages thermogenesis through allosteric activation of the TNAP glycerol pocket rather than altered substrate delivery or localization. Consistent with this model, glycerol-induced TNAP activity was detected exclusively in control *Alpl*$^{fl/fl}$ brown adipocytes and in *Alpl*$^{Adipoq\text{-}cre}$ brown adipocytes restored with WT TNAP, whereas those restored with the catalytically inactive TNAP(S110A) and empty AAV controls showed no detectable PCr hydrolytic activity (Extended Data Fig. 7o).

We next investigated the contribution of thermogenic adipocytes to TNAP-driven thermogenesis through the glycerol pocket in vivo. Given the compensatory interplay between UCP1 and futile cycles[34], we introduced empty AAV or TNAP variants (WT, S110A, K52S or D370G) into the parenchymal brown adipocytes of inducible double-knockout mice lacking both *Ucp1* and *Alpl* in all fat cells (*iADKO*$^{Alpl;Ucp1}$) (Fig. 4i and Extended Data Fig. 8a–c). Uncorrected indirect calorimetry after noradrenaline injection showed that *Alpl*$^{fl/fl}$*Ucp1*$^{fl/fl}$ controls and *iADKO*$^{Alpl;Ucp1}$ double-knockouts rescued with WT AAV displayed the strongest thermogenic responses (Extended Data Fig. 8f). We also quantified the noradrenaline-induced component of thermogenesis, revealing that WT AAV restored this response in double-knockout mice to control levels (Fig. 4j). Consistent with loss of catalytic activity in TNAP(S110A), noradrenaline-stimulated responses were indistinguishable from the empty AAV controls (Fig. 4j). Although TNAP allosteric glycerol pocket mutants (K52S and D370G) were expressed at comparable or higher levels and retained basal hydrolytic activity in the absence of glycerol (Extended Data Fig. 8c,d), neither restored thermogenesis. Instead, their responses were superimposable on catalytically dead TNAP(S110A) and empty AAV (Fig. 4j). While *Alpl* deletion modestly lowered endogenous *Ckb* mRNA, indicating coordinated regulation of FCC components, *Ckb* levels were indistinguishable across all rescued

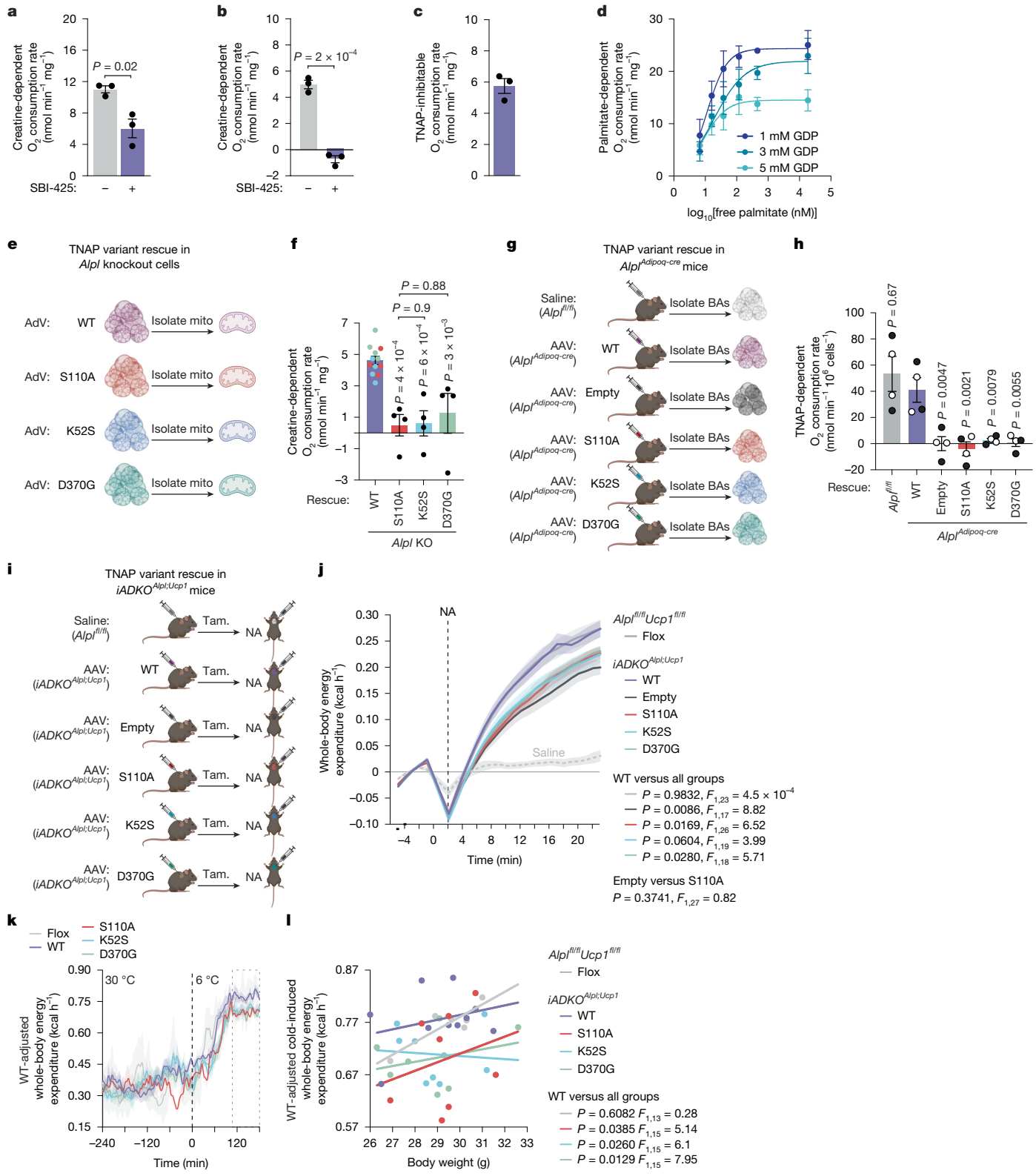

Fig. 4 | See next page for caption.

TNAP-variant groups (Extended Data Fig. 8e), excluding CKB abundance as a confounder. Together, these findings demonstrate that the glycerol pocket is essential for TNAP-mediated thermogenesis in vivo.

To independently validate these findings, we measured cold-induced energy expenditure in *iADKO*$^{Alpl;Ucp1}$ mice genetically restored with TNAP variants (Extended Data Fig. 8g–i). Analysis of uncorrected energy expenditure at cold steady state revealed no differences between the groups (Extended Data Fig. 8j,k). However, when the cold-induced response was analysed by normalizing all groups to a common internal reference (AAV-WT), TNAP WT fully restored the acute cold-induced increase in energy expenditure in *iADKO*$^{Alpl;Ucp1}$ mice to levels observed in the WT controls (*Alpl*$^{fl/fl}$*Ucp1*$^{fl/fl}$) (Fig. 4k,l), confirming robust rescue of thermogenic capacity. By contrast, TNAP glycerol-pocket mutants—despite comparable *Alpl* expression, basal

Fig. 4 | FCC contribution to thermogenesis. a, The respiratory rate at the state 3–4 transition. Data are shown for biologically independent BAT mitochondrial preparations ($n = 3$ per group). **b**, The sustained respiratory rate after reaching state 4 in BAT mitochondria. Data are shown for biologically independent BAT mitochondrial preparations ($n = 3$ per group). **c**, FCC was quantified as the TNAP-dependent component of sustained creatine-stimulated respiration in BAT mitochondria. Data are shown for biologically independent BAT mitochondrial preparations ($n = 3$ per group). **d**, Respiration in response to palmitate with increasing GDP in BAT mitochondria. Data are shown for biologically independent BAT mitochondrial preparations ($n = 3$ per group). **e**, Diagram of mitochondrial (mito) isolation. The diagram was created using BioRender; Kazak, L. https://BioRender.com/5hnzdv2 (2026). **f**, Rescue of FCC by TNAP variants after TNAP(S110A) mitochondria reached state 4. Data are shown for biologically independent mitochondrial preparations from in vitro differentiated brown adipocytes ($n = 4$ per group). WT datapoints are colour-matched to indicate paired sessions. **g**, Diagram of AAV rescue and brown adipocyte (BA) isolation. The diagram was created using BioRender. Kazak, L. https://BioRender.com/3oxjzad (2026). **h**, TNAP-dependent respiration in interscapular brown adipocytes isolated from 10–14-week-old male (black) and female (white) mice stimulated with noradrenaline (0.1 μM), corrected for ATP-dependent respiration measured in empty AAV-infected cells (Extended Data Fig. 7j) and glycerol-independent basal TNAP activity (Extended Data Fig. 7k). Data are shown for biologically independent brown adipocyte preparations isolated from interscapular BAT ($n = 4$ per group). **i**, Diagram of AAV rescue and noradrenaline BAT injection. The diagram was created using BioRender. Kazak, L. https://BioRender.com/jy08tig (2026). Tam, tamoxifen. **j**, Noradrenaline-stimulated whole-body energy expenditure in 12-week-old male control mice ($Alpl^{fl/fl}Ucp1^{fl/fl}$, $n = 16$) and $iADKO^{Alpl;Ucp1}$ mice expressing empty AAV, WT TNAP, TNAP(S110A), TNAP(K52S) or TNAP(D370G) ($n = 10$, 9, 19, 12 and 11, respectively), acclimatized to 22 ± 1 °C. **k**,**l**, WT-normalized whole-body energy expenditure (**k**) and cold-induced whole-body energy expenditure (100–180 min after ramp to 6 °C: hatched box) (**l**) in 12-week-old male control mice ($n = 6$) or $iADKO^{Alpl;Ucp1}$ mice expressing WT TNAP, TNAP(S110A), TNAP(K52S) or TNAP(D370G) ($n = 10$, 8, 8 and 8, respectively) acclimatized to 22 ± 1 °C and housed for 5 days at 30 °C before cold (6 °C) exposure. Data are mean ± s.e.m. of biologically independent samples. Statistical analysis was performed using two-tailed Student's *t*-tests (**a** and **b**), nonlinear regression (**d**), one-way ANOVA with Tukey's post hoc test (**f**), one-way ANOVA with Dunnett's post hoc test (**h**), two-way ANOVA with Tukey's post hoc test (**j**) and two-sided analysis of covariance (ANCOVA) with Bonferroni correction (**l**).

TNAP activity and endogenous *Ckb* levels (Extended Data Fig. 8i,l,m)—did not restore energy expenditure and phenocopied the catalytically inactive TNAP(S110A) mutant (Fig. 4k,l). Notably, the magnitude of the TNAP glycerol-pocket-dependent effect on energy expenditure was comparable to that reported for canonical thermogenic effectors such as *Ucp1*, and essential lipolytic regulators including adenylyl cyclase 3 (*Adcy3*) and CGI-58 (encoded by *Abhd5*)[35–37]. Food intake and locomotor activity did not differ among TNAP variant groups (Extended Data Fig. 8n,o). Together, these data establish the glycerol pocket as an essential determinant of TNAP-mediated thermogenesis in mitochondria, intact adipocytes and in vivo.

Mutations in the *ALPL* glycerol pocket

We hypothesized that the mechanism of TNAP activation identified in thermogenic adipocytes may also operate in other cell types. As reduced serum alkaline phosphatase, reflecting impaired TNAP activity, is the clinical hallmark of hypophosphatasia[38], we focused on skeletal mineralization. To investigate the phenotypic impact of *ALPL* variants in humans, we performed gene burden analyses using whole-exome sequencing data from the UK Biobank (UKBB; $n \approx 500{,}000$)[39]. Recognizing that variant grouping strategies affect the specificity of gene burden analyses[40], we applied multiple classification tools informed by experimental and structural data to evaluate missense variants across TNAP domains (Extended Data Fig. 9a and Supplementary Table 5). Deleterious variants in the glycerol pocket were strongly associated with lower plasma alkaline phosphatase activity and reduced bone mineral density (Fig. 5a,b, Extended Data Fig. 9b,c and Supplementary Table 6), aligning with TNAP's well-established role in skeletal mineralization. Notably, the strength of these associations exceeded those of variants in any other domain except the active site (Fig. 5b and Supplementary Table 7). Additional associations included nominal elevations in plasma calcium and phosphate (Extended Data Fig. 9d,e and Supplementary Table 6), phenotypes that are consistently observed in 15–20% of patients with hypophosphatasia, presumably attributable to impaired mineralization[41]. Supporting their pathogenicity, glycerol-pocket mutations are annotated in the *ALPL* mutation database (https://alplmutationdatabase.jku.at/) as causative for hypophosphatasia (Extended Data Fig. 9f). While other nominal associations were detected, none passed multiple-testing correction (Supplementary Tables 8 and 9), suggesting that most carriers exhibit milder, incompletely penetrant phenotypes. Notably, deleterious glycerol-pocket variants were nominally associated with reduced hip circumference (unadjusted for BMI), an effect not seen with variants in other TNAP domains, potentially reflecting altered pelvic bone structure. Nominal associations with HbA1c levels hint at a possible role for TNAP in glucose metabolism (Supplementary Table 8), although these findings require replication in larger cohorts. Sex-stratified analyses revealed no additional associations (Supplementary Table 10). *Z*-statistic comparisons confirmed the outsized phenotypic impact of glycerol pocket mutations relative to other regions (Supplementary Table 7). These findings establish the glycerol pocket as a critical functional domain of TNAP and underscore the clinical significance of *ALPL* mutations in this region.

The glycerol pocket optimizes mineralization

TNAP promotes bone mineralization by hydrolysing phosphate esters to generate P_i. Although its main physiological substrate is PP_i, a potent inhibitor of mineralization[4,42], β-glycerophosphate is widely used in osteoblast cultures in vitro as a source of TNAP-dependent P_i release[43]. Hydrolysis of β-glycerophosphate by TNAP would release both P_i and glycerol, raising the possibility that the liberated glycerol could engage the glycerol pocket to allosterically activate TNAP. As TNAP is not restricted to the plasma membrane but can also be released extracellularly on matrix vesicles or as a soluble enzyme[1], this mechanism could operate in the mineralizing milieu of bone. Using a well-established osteoblast-driven mineralization assay[42], we found that recombinant WT TNAP fully neutralized PP_i inhibition of mineralization by day 8, whereas TNAP glycerol pocket mutants (K52S, D370G) significantly delayed mineralization and the catalytically inactive TNAP(S110A) did not rescue it (Fig. 5c,d and Extended Data Fig. 10a).

To examine this mechanism further, we purified WT human TNAP (hTNAP) and four glycerol pocket variants (N49K, N49I, F327C and F327L) associated with reduced bone mineral density in UKBB and annotated in *ALPL* mutation databases (*ALPL* gene variant database; Leiden Open Variation Database, https://www.lovd.nl/). Glycerol stimulated PPi hydrolysis by WT hTNAP but did not activate most mutants, except for hTNAP(N49K), which retained partial responsiveness (Extended Data Fig. 10b). Structural modelling showed that Asn49 stabilizes the Thr366–Thr371 loop through a hydrogen-bond network essential for positioning Asp370 and shaping the pocket. N49K/I mutations disrupt this interaction, whereas F327C/L mutations probably enlarge the pocket and reduce glycerol affinity (Extended Data Fig. 10c–e). In the absence of glycerol, mutant and WT enzymes hydrolysed PP_i similarly, except for Asn49 variants, which showed reduced baseline activity (Extended Data Fig. 10f). To isolate the role of the glycerol pocket, we introduced hTNAP variants with equalized baseline enzyme activity (no glycerol) into osteoblast

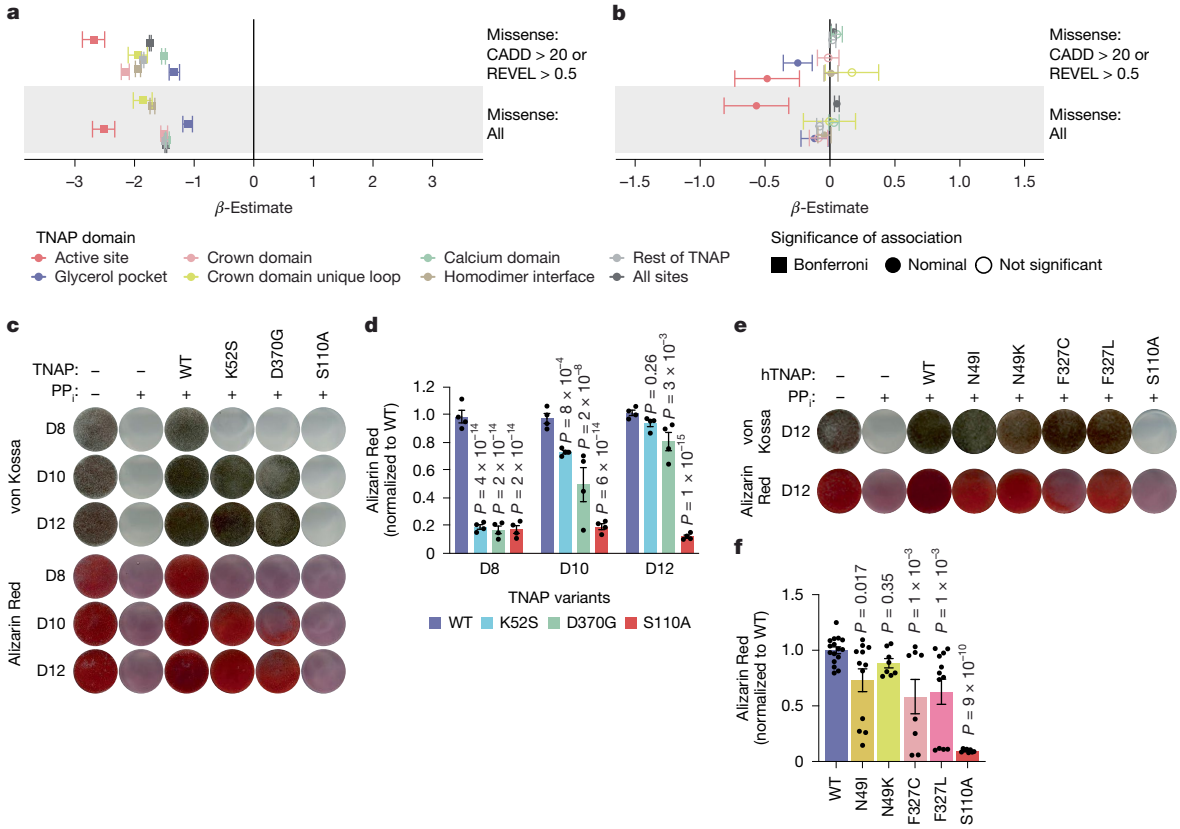

Fig. 5 | Associations between *ALPL* coding variants and human phenotypes. **a**,**b**, β-Estimates for associations between *ALPL* variant masks from the primary domain-stratified analyses (from Supplementary Table 6) and plasma alkaline phosphatase activity (**a**) and heel bone mineral density (BMD) (**b**). Points represent β-estimates of association for given variant masks (right), with standard errors. The squares indicate associations significant after Bonferroni correction ($P < 0.0016$), filled circles indicate nominal significance ($0.0016 < P < 0.05$) and open circles indicate non-significance ($P > 0.05$). Variant groupings include protein-truncating variants (PTVs) and three missense masks: (1) CADD > 20 or REVEL > 0.5; (2) CADD > 20 and REVEL > 0.5; and (3) all missense variants; masks 1 and 3 are shown here; PTVs and mask 2 are shown in Extended Data Fig. 9b,c. **c**, Representative von Kossa and Alizarin Red staining of mineral deposition in MC3T3-E1 osteoblast cultures after PP_i-mediated inhibition and rescue with TNAP variants. **d**, Calcium quantification by Alizarin Red staining. Data are shown for biologically independent cell cultures ($n = 4$ per group). **e**, Representative von Kossa and Alizarin Red staining of MC3T3-E1 osteoblast cultures after PP_i-mediated inhibition and rescue with UKBB-identified human TNAP variants. **f**, Calcium quantification by Alizarin Red staining for WT TNAP, and the TNAP(N49I), TNAP(N49K), TNAP(F327), TNAP(F327L) and TNAP(S110A) variants. Data are shown for biologically independent cell cultures ($n = 16, 12, 8, 8, 12$ and 8 per group, respectively). Data are mean ± s.e.m. of biologically independent samples. Statistical analysis was performed using two-way ANOVA with Fisher's least significant difference test (**d**) and one-way ANOVA with Fisher's least significant difference test (**f**).

cultures. WT hTNAP fully rescued mineralization from PP_i inhibition by day 12, whereas all pocket mutants, except for hTNAP(N49K), showed impaired rescue, and the catalytically inactive hTNAP(S110A) mutant had no effect (Fig. 5e,f and Extended Data Fig. 10g). These findings demonstrate that glycerol-dependent allosteric activation through the glycerol pocket is essential for optimal regulation of mineralization by osteoblasts, providing a direct mechanistic link between *ALPL* mutations in this domain and defective bone mineralization.

Discussion

Here we identify glycerol as an allosteric activator of TNAP, driving both UCP1-independent adipocyte thermogenesis and osteoblast-mediated mineralization. These findings define the activation mechanism of the FCC, quantify its substantial contribution relative to UCP1 and advance our understanding of energy-dissipating pathways, an area that is central to the development of thermogenic fat-based therapeutics. Quantitative analyses indicate that FCC-dependent respiration reaches around 40% of the capacity of UCP1-dependent respiration in cultured brown adipocytes. In isolated BAT mitochondria, FCC-mediated respiration is quantitatively comparable to around 23–60% of fatty acid-induced leak respiration, depending on GDP and fatty acid concentrations. Experiments with glycerol-pocket mutants show that this allosteric site contributes around 30% of total thermogenesis in mature brown adipocytes and is required to restore noradrenaline- and cold-induced energy expenditure in double-knockout mice to WT levels, even in the absence of UCP1. These data align closely with previous estimates that around 30% of noradrenaline-stimulated respiration in mouse and golden hamster brown adipocytes is sensitive to atractylate and oligomycin[2,44], and with mitochondrial studies in cold-acclimatized Wistar rat BAT showing that ATP synthesis accounts for around 30% of total ETC activity even after 5 weeks of cold exposure[25]. Consistent with a central role for the FCC, pharmacological inhibition of TNAP suppresses around 25–30% of the noradrenaline-driven thermogenic response[2]. These findings are reinforced by genetic models, where loss of *Ckb* or *Alpl* in adipocytes impairs adrenergic-stimulated metabolism, and re-expression of WT, but not catalytically inactive or glycerol-pocket mutant, TNAP proteins in inducible *Ucp1/Alpl* double-knockouts restores thermogenic capacity. Together with recent studies from our group and others[7,34,45–49], these results establish that the FCC controls a substantial fraction of heat production alongside UCP1.

In brown adipocytes, intracellular glycerol accumulation during thermogenic stimulation, coupled with TNAP's unique mitochondrial localization, enables FCC engagement. In osteoblasts, plasma-

membrane-anchored or extracellular TNAP may be activated by glycerol released from neighbouring marrow adipocytes—a hypothesis that remains to be tested. The low Hill coefficient that we observed with recombinant TNAP suggests that glycerol does not operate as a binary on–off allosteric switch. Rather, it functions as a tuneable, concentration-dependent modulator of TNAP activity across the physiological glycerol levels we measure in BAT, which fall in the millimolar range. This is characteristic of negative cooperativity, a regulatory mechanism common among enzymes that must remain responsive over a broad range of allosteric metabolite concentrations[50]. We propose that this enables TNAP to sense intracellular glycerol levels and calibrate its activity to match nutrient catabolism and thermogenic demand.

The physiological importance of the glycerol pocket is reinforced by human genetics. *ALPL* variants in this domain are strongly associated with reduced plasma alkaline phosphatase activity and lower bone mineral density, effects rivalled only by mutations in the active site. Few gene burden analyses in population cohorts have compared protein functional domains, and this work highlights the power of domain-specific gene burden analyses to identify functionally critical substructures within proteins.

The broader implications may extend well beyond adipose and bone. The glycerol pocket is conserved across alkaline phosphatase isoforms, nominating parallel regulatory mechanisms in intestinal and placental enzymes. In liver and brain, where TNAP governs processes including bile production, LPS detoxification and vitamin B6 metabolism[51–53], glycerol-dependent modulation may likewise tune enzyme function. Moreover, the allosteric network connecting the glycerol pocket to the active site suggests that mutations beyond direct glycerol-contacting residues could impair this mechanism, expanding the mutational landscape of hypophosphatasia and refining its clinical diagnosis.

Together, our findings identify the glycerol pocket as a metabolite-sensitive allosteric site that integrates metabolic state with TNAP function. By linking adipocyte thermogenesis and skeletal mineralization through a common molecular mechanism, our work not only expands the conceptual framework of energy-dissipating pathways but also opens avenues for structure-guided design of TNAP activators, offering a targeted alternative to enzyme replacement therapy for skeletal disease, which currently requires burdensome tri-weekly injections[6].

Online content

Any methods, additional references, Nature Portfolio reporting summaries, source data, extended data, supplementary information, acknowledgements, peer review information; details of author contributions and competing interests; and statements of data and code availability are available at https://doi.org/10.1038/s41586-026-10396-9.

1. Millan, J. L. Alkaline phosphatases: structure, substrate specificity and functional relatedness to other members of a large superfamily of enzymes. *Purinergic Signal.* **2**, 335–341 (2006).
2. Rahbani, J. F. et al. ADRA1A–$G_{\alpha q}$ signalling potentiates adipocyte thermogenesis through CKB and TNAP. *Nat. Metab.* **4**, 1459–1473 (2022).
3. Sun, Y. et al. Mitochondrial TNAP controls thermogenesis by hydrolysis of phosphocreatine. *Nature* **593**, 580–585 (2021).
4. Reznikov, N. et al. Biological stenciling of mineralization in the skeleton: local enzymatic removal of inhibitors in the extracellular matrix. *Bone* **138**, 115447 (2020).
5. Narisawa, S., Frohlander, N. & Millan, J. L. Inactivation of two mouse alkaline phosphatase genes and establishment of a model of infantile hypophosphatasia. *Dev. Dyn.* **208**, 432–446 (1997).
6. Millan, J. L. & Whyte, M. P. Alkaline phosphatase and hypophosphatasia. *Calcif. Tissue Int.* **98**, 398–416 (2016).
7. Bunk, J. et al. The futile creatine cycle powers UCP1-independent thermogenesis in classical BAT. *Nat. Commun.* **16**, 3221 (2025).
8. Bunk, J. et al. Creatine kinase B mediates UCP1-independent beige fat thermogenesis via the futile creatine cycle in mice. *Mol. Metab.* **98**, 102193 (2025).
9. Rahbani, J. F. et al. Creatine kinase B controls futile creatine cycling in thermogenic fat. *Nature* **590**, 480–485 (2021).
10. Hsieh, A. C. & Carlson, L. D. Role of adrenaline and noradrenaline in chemical regulation of heat production. *Am. J. Physiol.* **190**, 243–246 (1957).
11. Locke, R. M., Rial, E., Scott, I. D. & Nicholls, D. G. Fatty acids as acute regulators of the proton conductance of hamster brown-fat mitochondria. *Eur. J. Biochem.* **129**, 373–380 (1982).
12. Mills, E. L. et al. Accumulation of succinate controls activation of adipose tissue thermogenesis. *Nature* **560**, 102–106 (2018).
13. Sergienko, E. et al. Identification and characterization of novel tissue-nonspecific alkaline phosphatase inhibitors with diverse modes of action. *J. Biomol. Screen.* **14**, 824–837 (2009).
14. Garcia, A. F. et al. Effects of GPI-anchored TNAP on the dynamic structure of model membranes. *Phys. Chem. Chem. Phys.* **17**, 26295–26301 (2015).
15. Furter, R., Furter-Graves, E. M. & Wallimann, T. Creatine kinase: the reactive cysteine is required for synergism but is nonessential for catalysis. *Biochemistry* **32**, 7022–7029 (1993).
16. Yu, Y. et al. The structural pathology for hypophosphatasia caused by malfunctional tissue non-specific alkaline phosphatase. *Nat. Commun.* **14**, 4048 (2023).
17. de Backer, M. et al. The 1.9 A crystal structure of heat-labile shrimp alkaline phosphatase. *J. Mol. Biol.* **318**, 1265–1274 (2002).
18. Hoylaerts, M. F. et al. Functional significance of calcium binding to tissue-nonspecific alkaline phosphatase. *PLoS ONE* **10**, e0119874 (2015).
19. Krezel, A. & Maret, W. The biological inorganic chemistry of zinc ions. *Arch. Biochem. Biophys.* **611**, 3–19 (2016).
20. Cinti, S. in *Adipose Tissue and Adipokines in Health and Disease* (eds Fantuzzi, G & Mazzone, T.) 3–19 (Humana Press, 2003).
21. Moser, C. et al. Quantification of adipocyte numbers following adipose tissue remodeling. *Cell Rep.* **35**, 109023 (2021).
22. Kazak, L. et al. Genetic depletion of adipocyte creatine metabolism inhibits diet-induced thermogenesis and drives obesity. *Cell Metab.* **26**, 660–671 (2017).
23. Kazak, L. et al. Ablation of adipocyte creatine transport impairs thermogenesis and causes diet-induced obesity. *Nat. Metab.* **1**, 360–370 (2019).
24. Shabalina, I. G., Jacobsson, A., Cannon, B. & Nedergaard, J. Native UCP1 displays simple competitive kinetics between the regulators purine nucleotides and fatty acids. *J. Biol. Chem.* **279**, 38236–38248 (2004).
25. Hittelman, K. J., Lindberg, O. & Cannon, B. Oxidative phosphorylation and compartmentation of fatty acid metabolism in brown fat mitochondria. *Eur. J. Biochem.* **11**, 183–192 (1969).
26. Fromme, T. et al. Degradation of brown adipocyte purine nucleotides regulates uncoupling protein 1 activity. *Mol. Metab.* **8**, 77–85 (2018).
27. Nicholls, D. G. Mitochondrial proton leaks and uncoupling proteins. *Biochim. Biophys. Acta Bioenerg.* **1862**, 148428 (2021).
28. Locke, R. M. & Nicholls, D. G. A re-evaluation of the role of fatty acids in the physiological regulation of the proton conductance of brown adipose tissue mitochondria. *FEBS Lett.* **135**, 249–252 (1981).
29. Locke, R. M., Rial, E. & Nicholls, D. G. The acute regulation of mitochondrial proton conductance in cells and mitochondria from the brown fat of cold-adapted and warm-adapted guinea pigs. *Eur. J. Biochem.* **129**, 381–387 (1982).
30. Rial, E., Poustie, A. & Nicholls, D. G. Brown-adipose-tissue mitochondria: the regulation of the 32000-Mr uncoupling protein by fatty acids and purine nucleotides. *Eur. J. Biochem.* **137**, 197–203 (1983).
31. Esteves, T. C., Parker, N. & Brand, M. D. Synergy of fatty acid and reactive alkenal activation of proton conductance through uncoupling protein 1 in mitochondria. *Biochem. J.* **395**, 619–628 (2006).
32. Rial, E. et al. Retinoids activate proton transport by the uncoupling proteins UCP1 and UCP2. *EMBO J.* **18**, 5827–5833 (1999).
33. Matthias, A., Jacobsson, A., Cannon, B. & Nedergaard, J. The bioenergetics of brown fat mitochondria from UCP1-ablated mice. Ucp1 is not involved in fatty acid-induced de-energization ("uncoupling"). *J. Biol. Chem.* **274**, 28150–28160 (1999).
34. Rahbani, J. F. et al. Parallel control of cold-triggered adipocyte thermogenesis by UCP1 and CKB. *Cell Metab.* **36**, 526–540 (2024).
35. Khani, S. et al. Cold-induced expression of a truncated adenylyl cyclase 3 acts as rheostat to brown fat function. *Nat. Metab.* **6**, 1053–1075 (2024).
36. Shin, H. et al. Lipolysis in brown adipocytes is not essential for cold-induced thermogenesis in mice. *Cell Metab.* **26**, 764–777 (2017).
37. Mills, E. L. et al. Cysteine 253 of UCP1 regulates energy expenditure and sex-dependent adipose tissue inflammation. *Cell Metab.* **34**, 140–157 (2022).
38. Whyte, M. P. Hypophosphatasia—aetiology, nosology, pathogenesis, diagnosis and treatment. *Nat. Rev. Endocrinol.* **12**, 233–246 (2016).
39. Sudlow, C. et al. UK biobank: an open access resource for identifying the causes of a wide range of complex diseases of middle and old age. *PLoS Med.* **12**, e1001779 (2015).
40. Povysil, G. et al. Rare-variant collapsing analyses for complex traits: guidelines and applications. *Nat. Rev. Genet.* **20**, 747–759 (2019).
41. Berkseth, K. E. et al. Clinical spectrum of hypophosphatasia diagnosed in adults. *Bone* **54**, 21–27 (2013).
42. Addison, W. N., Azari, F., Sorensen, E. S., Kaartinen, M. T. & McKee, M. D. Pyrophosphate inhibits mineralization of osteoblast cultures by binding to mineral, up-regulating osteopontin, and inhibiting alkaline phosphatase activity. *J. Biol. Chem.* **282**, 15872–15883 (2007).
43. Bellows, C. G., Heersche, J. N. & Aubin, J. E. Inorganic phosphate added exogenously or released from beta-glycerophosphate initiates mineralization of osteoid nodules in vitro. *Bone Miner.* **17**, 15–29 (1992).
44. Nedergaard, J. & Lindberg, O. Norepinephrine-stimulated fatty-acid release and oxygen consumption in isolated hamster brown-fat cells. Influence of buffers, albumin, insulin and mitochondrial inhibitors. *Eur. J. Biochem.* **95**, 139–145 (1979).
45. Wang, T. et al. Single-nucleus transcriptomics identifies separate classes of UCP1 and futile cycle adipocytes. *Cell Metab.* **36**, 2130–2145 (2024).
46. Vargas-Castillo, A. et al. Development of a functional beige fat cell line uncovers independent subclasses of cells expressing UCP1 and the futile creatine cycle. *Cell Metab.* **36**, 2146–2155 (2024).

47. Ni, J. et al. Celastrol targets CKB-mediated futile creatine cycle in human brown adipocytes thermogenesis. *Metabol. Open* **26**, 100359 (2025).
48. Hepler, C. et al. Time-restricted feeding mitigates obesity through adipocyte thermogenesis. *Science* **378**, 276–284 (2022).
49. Fang, J. et al. Creatinine promotes adipose tissue wasting in chronic kidney disease via creatine and futile creatine cycle. *Mol. Metab.* **98**, 102191 (2025).
50. Cornish-Bowden, A. The physiological significance of negative cooperativity revisited. *J. Theor. Biol.* **319**, 144–147 (2013).
51. Poupon, R. Liver alkaline phosphatase: a missing link between choleresis and biliary inflammation. *Hepatology* **61**, 2080–2090 (2015).
52. Briolay, A., Bessueille, L. & Magne, D. TNAP: a new multitask enzyme in energy metabolism. *Int. J. Mol. Sci.* **22**, 10470 (2021).
53. Hasegawa, A. et al. Prenatal enzyme replacement therapy for *Akp2*$^{-/-}$ mice with lethal hypophosphatasia. *Regen. Ther.* **18**, 168–175 (2021).

Methods

Materials

SBI-425 (MedChemExpress, HY-124756) was stored at −80 °C and dissolved in dimethyl sulfoxide (DMSO) fresh before use. Creatine monohydrate (Millipore Sigma, C3630) and sodium creatine phosphate dibasic tetrahydrate (Millipore Sigma, 27920) were stored at 4 °C and dissolved in assay buffer fresh before use. Glycerol was from Millipore Sigma (356350). L-(−)-malic acid (Millipore Sigma, M1000) was dissolved in water (pH 7.2) at 0.5 M, aliquoted and stored at −20 °C. Sodium pyruvate (Millipore Sigma, P2256) was dissolved in water (pH 7.2) at 0.5 M and used fresh. Palmitic acid (Millipore Sigma, P0500) was dissolved in 100% ethanol fresh before use. GDP (Millipore Sigma, G7127) and ADP (Millipore Sigma, A2754) were dissolved in water (pH 7.2) at 0.1 M, aliquoted and stored at −20 °C. FCCP (Millipore Sigma, C2920) was dissolved in DMSO at 0.5 M, aliquoted and stored at −20 °C. BSA, essentially fatty acid free (Millipore Sigma, A6003), was dissolved in water at 20%, aliquoted and stored at −20 °C. Pierce Anti-HA Magnetic beads (Thermo Fisher Scientific, 88836). d3 creatine (Cambridge Isotopes, DLM-1302) and glycerol-$^{13}C_3$ (Millipore Sigma, 489476) were dissolved in water for LC–MS and GC–MS.

Animals

Mouse experiments were performed according to procedures approved by the Animal Resource Centre at McGill University and complied with guidelines set by the Canadian Council of Animal Care. Mice were born and housed in groups of 3–5 per cage at 22 ±1 °C until experimental intervention (at 6–12 weeks old). The photoperiod was fixed at 12 h–12 h light–dark, with lights on at 07:00, and the mice had ad libitum access to drinking water and a low-fat diet (2920X, Envigo) at 40–60% humidity. WT C57BL/6N mice were purchased from Charles River Laboratories (027). *Adipoq-cre* mice (*B6;FVB-Tg(Adipoq-cre)1Evdr/J)*, 028020), maintained on a C57BL/6J background, were bred with *Slc6a8*$^{fl/fl}$ or *Slc6a8*$^{fl/y}$ mice[23] and *Gatm*$^{fl/fl}$ mice[22] to generate *Slc6a8;Gatm* double-knockout male mice (*Slc6a8;Gatm*$^{Adipoq\text{-}cre}$) and control (*Slc6a8*$^{fl/y}$*;Gatm*$^{fl/fl}$) male mice. *Ckb*^{FLAG} mice have been previously described[9]. Adipocyte-selective *Alpl* knockout mice (*Alpl*$^{Adipoq\text{-}cre}$) have been described previously[3]. *Ucp1*$^{fl/fl}$ (*B6(129S4)-Ucp1*$^{tm1c(EUCOMM)Hmgu}$*/KazJ*) are available at the Jackson Laboratory Repository (039539; http://jaxmice.jax.org/query). *Alpl*$^{fl/+}$ mice[3] were mated to *Ucp1*$^{fl/+}$ mice[34] to generate *Alpl*$^{fl/fl}$*Ucp1*$^{fl/fl}$ mice, which were then crossed to AdipoqCreERT2 mice[54] (C57BL/6N, Jax, 025124) to generate: (1) inducible adipocyte-selective *Alpl;Ucp1* double-KO mice (*iADKO*$^{Alpl;Ucp1}$) and (2) control floxed mice (*Alpl*$^{fl/fl}$*;Ucp1*$^{fl/fl}$). Mouse experiments used age-matched littermates. For GC–MS and LC–MS analyses, mice aged 6–8 weeks were singly housed at 30 °C or 6 °C for 3 weeks in cages with ad libitum access to drinking water and a chow diet. Mice were euthanized by cervical dislocation and tissues were processed for mitochondrial isolation or immediately flash-frozen in liquid nitrogen and stored at −80 °C until further analysis. Experimental mice in each genotype were randomly assigned to treatment groups. Investigators were not blinded to experimental conditions, as the procedures required knowledge of group assignments for appropriate treatment administration. Sample sizes were predetermined based on effect size, s.d. and significance level required to attain statistical significance of $P < 0.05$ with a 90% probability on the basis of previous experiments using similar methodologies and were deemed sufficient to account for any biological/technical variability[22,23,55,56]. For experiments without predetermination, sample sizes were chosen on the basis of previous experience and published standards in the field. Sample sizes are indicated for each experiment in the manuscript.

Inducible gene inactivation

Mice were housed at 22 ± 1 °C and maintained on a chow diet. At 6–9 weeks of age, 3 days after AAV-FLEX infection, tamoxifen (T5648, Sigma-Aldrich) was administered through intraperitoneal (i.p.) injection. The tamoxifen was prepared as a 20 mg ml^{-1} solution in corn oil and delivered to experimental and control mice at a dose of 75 mg per kg once daily for three consecutive days at room temperature (22 ± 1 °C). After completing the treatment, mice were given a 3 day recovery period at the same temperature.

RNA extraction

Total RNA was extracted from frozen mouse tissues using TRIzol Lysis Reagent (Life Technologies) and purified using RNeasy Mini spin columns (Qiagen) according to the manufacturer's instructions. RNA was quantified using the NanoDrop 8000 spectrophotometer (Thermo Fisher Scientific).

RT–qPCR

Purified RNA was reverse transcribed using a High-Capacity cDNA Reverse Transcription kit (Applied Biosystems) and the resultant cDNA was analysed using quantitative PCR (qPCR). In brief, 20 ng cDNA and 150 nmol of each primer were mixed with GoTaq qPCR Master Mix (Promega, A6002) in a 384-well format and amplified using the CFX384 real-time PCR system (Bio-Rad). Reaction conditions were as follows: initial denaturation at 95 °C for 3 min, then 39 cycles of denaturation at 95 °C for 5 s, annealing at 60 °C for 25 s and extension at 72 °C for 20 s. Normalized mRNA expression was calculated using the $\Delta\Delta C_t$ method, using *Ppib* as the reference gene. CFX Maestro 2017 was used for data collection. Primer sequences used for reverse transcription–qPCR (RT–qPCR) were as follows: *Ckb* (forward, GCCTCACTCAG ATCGAAACTC; reverse, GGCATGTGAGGATGTAGCCC); *Alpl* coding sequence (forward, CCAACTCTTTTGTGCCAGAGA; reverse, GGCTAC ATTGGTGTTGAGCTTTT); *Alpl* 3′-UTR (forward, CATAGTCACGGCC AGTCCTC; reverse, TGGGAGTCTCATCCTGAGCA); *Gatm* (forward, ATGCCTGTGTCGCACCATTC; reverse, TTGCACATCTCTTCGACCTCA); *Slc6a8* (forward, GTGTGGAGATCTTCCGCCAT; reverse, CCCGTGGAGAG CCTCAATAC); *Pparg2* (forward, TGCCTATGAGCACTTCACAAGAAAT; reverse, CGAAGTTGGTGGGCCAGAA); *Fabp4* (forward, AAGGTGAAG AGCATCATAACCCT; reverse, TCACGCCTTTCATAACACATTCC); *Adipoq* (forward, TGTTCCTCTTAATCCTGCCCA; reverse, CCAACCTGCACAAG TTCCCTT); *Ucp1* (forward, ACTGCCACACCTCCAGTCATT; reverse, CTTTGCCTCACTCAGGATTGG); *Ppib* (forward, GGAGATGGCACAGG AGGAA; reverse, GCCCGTAGTGCTTCAGCTT).

Western blotting

Samples were prepared in lysis buffer (50 mM Tris, pH 7.4, 500 mM NaCl, 1% NP-40, 20% glycerol, 5 mM ethylenediaminetetraacetic acid (EDTA), and 1 mM phenylmethylsulfonyl fluoride), supplemented with cOmplete EDTA-free protease inhibitor cocktail (Roche). The homogenates were centrifuged at 16,000*g* for 10 min at 4 °C, and the supernatants were used for subsequent analyses. Protein concentrations were determined using the bicinchoninic acid assay (Pierce). The quantity of protein lysate required for each antibody was determined empirically. Protein lysates were denatured in Laemmli buffer[57], resolved by 10% Tris/glycine SDS–polyacrylamide gel electrophoresis, transferred to polyvinylidene difluoride membranes and blocked for 1 h using Tris-buffered saline containing 0.05% Tween-20 (TBST) and 5% milk powder. Primary antibodies against VCL (Cell Signaling, 13901, 1:5,000), total-OXPHOS (Abcam, ab110413, 1:200), Flag (Cell Signaling, 2368, 1:1,000), TOM20 (Santa Cruz, sc-11415, 1:4,000), TOM70 (Santa Cruz, sc-390545, 1:1,000), calnexin (Abcam, ab22595, 1:4,000), PMP70 (Abcam, ab3421, 1:500), UCP1 (Abcam, ab10983, 1:2,000), CKMT2 (Abcam, ab189314, 1:1,000), TNAP (R&D Systems, AF2910, 1:200), TIM23 (BD Biosciences, 611222, 1:200), LONP1 (Abcam, ab103809, 1:1,500), CKB (Abclonal, ab12631, 1:1,000) and HSP60 (Abcam, ab46798, 1:10,000) were diluted in TBST, 5% BSA and 0.02% sodium azide. Membranes were incubated with primary antibodies overnight at 4 °C and with HRP-conjugated secondary antibodies anti-rabbit (Promega, W4011), anti-mouse (Promega, W4021) or anti-goat HRP (Promega, V8051) (1:10,000) for 45 min at room temperature. The results

were visualized with enhanced chemiluminescence western blotting substrates (Bio-Rad) on the Chemidoc Imaging system (Bio-Rad).

Creatine- and PCr-stimulated NADH oxidation in lysates

A coupled enzymatic reaction (pyruvate kinase and lactate dehydrogenase) was used to determine creatine kinase activity (as determined by ATP utilization by native creatine kinase in the biological sample). The absorbance at 340 nM was measured to determine the ATP turnover rate using the BioTek Synergy H1 plate reader in kinetic mode. The assay was performed at 25 °C under the following conditions: coupling substrates were added together (5 mM ATP, 4 mM PEP, 0.45 mM NADH), along with assay buffer (20 mM $MgCl_2$, 100 mM KCl, 50 mM Tris pH either at 7.2 or 9.0 (noted in the figure legends)) and 10 mM creatine. For K_M determination, the creatine concentration was varied between 0 and 10 mM. Approximately 100 µg of total native protein was used to determine creatine kinase activity from either whole cell extracts, mitochondrial extracts, or post-mitochondrial supernatants. To assay creatine cycling (PCr-stimulated NADH oxidation), 40 µg of mitochondrial protein lysate was pre-incubated with assay buffer and either 10 mM creatine or 10 mM PCr for 40 min before adding coupling substrates to initiate the reaction.

Cloning, expression and purification of TNAP variants

Full-length mouse *Alpl* was purchased from Biobasic. We subcloned residues Phe18–Gly501 of mTNAP (UniProt: P09242) into the pFast-bac dual vector (a gift from B. Nagar) downstream of the polyhedrin promoter. The endogenous signal peptide (residues 1–17) was replaced with a melittin signal peptide (MKFLVNVALVFMVVYISYIYADGS) to enable protein secretion from Sf9 insect cells infected with recombinant baculovirus. Recombinant TNAP also included a C-terminal 6×His tag for purification purposes. TNAP variants were generated by site-directed mutagenesis and verified by Sanger sequencing (Génome Québec Innovation Centre).

Protein expression was performed at 27 °C for 66 h in I-Max medium (Wisent). Proteins were isolated with Ni-NTA beads (Thermo Fisher Scientific). Contaminants were removed with wash buffer (20 mM HEPES pH 8.0, 0.2 M NaCl, 2 mM $MgCl_2$, 25 µM $ZnCl_2$, 10 mM imidazole), then TNAP was eluted from the beads with 250 mM imidazole and dialysed using a 30 kDa molecular weight cut-off concentrator (Cytiva) into storage buffer (20 mM HEPES pH 8.0, 0.2 M NaCl, 2 mM $MgCl_2$, 25 µM $ZnCl_2$ and 10% glycerol) and stored at −80 °C. To ensure complete glycerol removal for functional assays, TNAP was first buffer-exchanged over a micro bio-spin column P-6 (Bio-Rad) equilibrated with 20 mM HEPES pH 8.0, 0.15 M NaCl, 2 mM $MgCl_2$ and 25 µM $ZnCl_2$, then resolved over a Superdex 200 Increase 3.2/300 GL column (Cytiva) equilibrated with the same buffer. For structural studies, TNAP variants were subjected to size-exclusion chromatography using the Superdex 200 Increase 10/300 GL column (Cytiva) equilibrated with 50 mM Tris pH 8.0, 0.15 M NaCl, 2 mM $MgCl_2$ and 25 µM $ZnCl_2$.

TNAP activity

Recombinant TNAP was dialysed into storage buffer (20 mM HEPES, pH 8.0, 2 mM $MgCl_2$, 25 µM $ZnCl_2$, 150 mM NaCl). BAT mitochondrial lysates were solubilized at 4.8 mg ml^{-1} in lysis buffer (50 mM Tris, pH7.5, 500 mM NaCl, 1% NP-40, 2 mM EDTA). Recombinant TNAP (40 ng) or mitochondrial protein lysate (90–100 µg) was added to a reaction buffer (100 mM HEPES, pH 7.2, 40 mM $MgCl_2$, 10 mM PCr (or various PCr concentrations for Michaelis–Menten determination), 0.2 mM 7-methyl-6-thioguanosine (MESG), 0.1 U PNP) supplemented with or without 1 mM glycerol (or various ligand concentrations for Hill determination). The absorbance at 360 nM was measured using the BioTek Synergy H1 plate reader pre-equilibrated to 37 °C in kinetic mode. For general confirmation of TNAP activity, and to determine TNAP basal activity levels in lysates and for use in osteoblast-regulated mineralization assays, a standard assay using *p*-nitrophenyl phosphate (*p*-NPP) as substrate was used (SIGMAFAST, Millipore Sigma, N1891) where 1 U of TNAP is defined as the quantity required to hydrolyse 1 µmol of *p*-NPP per min at 37 °C (ref. 42).

Brown adipocyte immortalization and differentiation

Stromal vascular cells from BAT were infected with retrovirus (pBabe-Neo largeT; Addgene, 1780), passaged four times and frozen as immortalized stocks. Parental cell lines were tested empirically for differentiation capacity. Brown pre-adipocytes were grown to post-confluency and differentiated with adipogenic cocktail (1 µM rosiglitazone, 0.5 mM 3-isobutyl-1-methylxanthine, 5 µM dexamethasone, 0.114 µg ml^{-1} insulin, 1 nM triiodothyronine and 125 µM indomethacin). Cells were re-fed every 48 h with maintenance cocktail (1 µM rosiglitazone and 0.5 µg ml^{-1} insulin). Adipocytes were fully differentiated 6 days after initial exposure to the adipogenic cocktail. TNAP-knockout preadipocytes were generated from $Alpl^{fl/fl}$ immortalized preadipocytes using Cre-recombinase-expressing adenovirus and limiting dilution, as previously described[9].

Mitochondrial isolation from in vitro differentiated brown adipocytes

Two 15-cm dishes of differentiated adipocytes were gently scraped in 6 ml of hypotonic buffer (20 mM HEPES, pH 7.8, 5 mM KCl, 1.5 mM $MgCl_2$, 1 mg ml^{-1} fatty acid-free BSA), and placed onto ice for 10 min. Cells were homogenized on ice by 25 strokes with a tight-fitting Dounce homogenizer, and rapidly equilibrated to 1× MSH buffer (210 mM mannitol, 70 mM sucrose, 20 mM HEPES, pH 7.8) using a 2.5× MSH stock. The homogenate was spun at 8,500*g* for 10 min at 4 °C and the fat layer was discarded. The pellet was resuspended in 1× MSH buffer and spun at 600*g* for 5 min at 4 °C to pellet the nuclei and cell debris. The post-nuclear supernatant was spun at 8,500*g* for 10 min at 4 °C. The pelleted mitochondria were resuspended in storage buffer (100 mM KCl and 20 mM K-TES, pH 7.2) and the total protein was quantified using the Pierce BCA Protein Assay Kit (Thermo Fisher Scientific, 23225).

Mitochondrial isolation from BAT

BAT was excised from eight mice, minced in 10 ml of MSH buffer (210 mM mannitol, 70 mM sucrose, 20 mM HEPES, pH 7.8, and 2 mg ml^{-1} fatty acid-free BSA) and homogenized on ice with a mechanical Potter–Elvehjem homogenizer (15 strokes). The homogenate was spun at 8,500*g* for 10 min at 4 °C and the fat layer was discarded. The pellet was resuspended in MSH buffer and spun at 600*g* for 5 min at 4 °C to pellet the nuclei and cell debris. The post-nuclear supernatant was spun at 8,500*g* for 10 min at 4 °C to pellet the mitochondria. Mitochondria were resuspended in storage buffer (100 mM KCl and 20 mM K-TES pH 7.2) and the total protein was quantified using the Pierce BCA Protein Assay Kit (Thermo Fisher Scientific, 23225).

Protease protection assays

Mitochondria (0.4 mg) were treated with 5 µg trypsin in MSH buffer (210 mM mannitol, 70 mM sucrose, 20 mM HEPES, pH 7.8) in a final volume of 200 µl and rotated end over end for 20 min at room temperature. The reactions were spiked with FBS (25 µl) to inhibit the trypsin, the samples were spun at 10,000*g* for 2 min at 4 °C to pellet mitochondria and the supernatant was removed. The mitochondria were washed twice in MSH buffer by rotating the tubes 180° and spinning at 10,000*g* for 2 min at 4 °C to pellet the mitochondria on the other sides of the tubes. Mitochondrial pellets were lysed to a final concentration of 5 µg $µl^{-1}$ in adipocyte lysis buffer (50 mM Tris, pH 7.5, 500 mM NaCl, 1% IGEPAL, 20% glycerol, and 2 mM EDTA), supplemented with protease and phosphatase inhibitor cocktail tablets (Roche). The samples were stored at −80 °C until further analysis by western blotting.

Calculation of ADP:creatine stoichiometry (FCC)

A Clark-type electrode (Rank Bros) was used to determine futile creatine cycling using limited creatine. To this end, 10 µM creatine (7 nmol

in a 0.7 ml reaction volume) was added to 0.25 mg brown adipocyte mitochondria in respiration buffer (125 mM sucrose, 20 mM K-TES, pH 7.2, 2 mM $MgCl_2$, 1 mM EDTA, 4 mM KH_2PO_4, 4% fatty acid-free BSA, 10 mM pyruvate, 5 mM malate and 1 mM GDP) and 70 nmol ADP was added to initiate ADP-dependent respiration. Pilot experiments were conducted to determine the length of time and ADP concentration (100 µM) required to reach state 4 respiration, when the respiratory rate post-ADP addition matched the rate pre-addition. Once these parameters were established, the total nmol of oxygen consumed was measured over this time, based on the oxygen consumption rate (measured in nmol min^{-1}). The excess oxygen consumed by creatine supplementation was used to determine the super-stoichiometric action of creatine by quantifying ADP liberation based on a phosphorus/oxygen ratio of 2.7. The data (Fig. 2d) represent the number of moles of liberated ADP (measured as the creatine-dependent change in ADP-dependent O_2 consumption) over the moles of added creatine. Rank Brothers Dual Digital model 20: Picolog 6 data logging software was used for data collection.

Quantitative thermogenic contribution of the FCC in mitochondria

A Clark-type electrode was used to determine the quantitative contribution of futile creatine cycling in mitochondria isolated from cultured brown adipocytes or BAT. Mitochondria (0.075 mg) were added to respiration buffer (125 mM sucrose, 20 mM K-TES, pH 7.2, 2 mM $MgCl_2$, 1 mM EDTA, 0.5 mM KH_2PO_4, 4% fatty acid-free BSA, 10 mM pyruvate and 5 mM malate) supplemented with 1, 3 or 5 mM GDP. The total volume in the respiration chamber was 0.7 ml, and 280 nmol (400 µM) ADP was added to initiate ADP-dependent respiration. For mitochondria isolated from cultured cells, the respiration buffer was supplemented with creatine and/or glycerol (1 mM each) or vehicle (respiration buffer). For mitochondria isolated from BAT, the respiration buffer was supplemented with 5 mM glycerol and/or 3 mM creatine. SBI-425 was used at a final concentration of 10 µM. All reported respiratory rates were normalized to the state 2 respiratory rate (defined as the mitochondrial oxygen consumption rate before ADP addition). Rank Brothers Dual Digital model 20: Picolog 6 data logging software was used for data collection.

Quantifying the thermogenic contributions of UCP1 in mitochondria

A Clark-type electrode was used to determine the quantitative contributions of UCP1 in mitochondria isolated from cultured brown adipocytes or BAT. Mitochondria (0.075 mg) were added to respiration buffer (125 mM sucrose, 20 mM K-TES, pH 7.2, 2 mM $MgCl_2$, 1 mM EDTA, 0.5 mM KH_2PO_4, 0.1% fatty acid-free BSA, 10 mM pyruvate and 5 mM malate) supplemented with 1 mM, 3 mM or 5 mM GDP. The total volume in the respiration chamber was 0.7 ml. Palmitate was titrated during the respiratory trace (see the 'Calculating free palmitate concentrations' section). All of the recorded respiratory rates were normalized to the state 2 respiratory rate (defined as the mitochondria's oxygen consumption rate before ADP addition). Rank Brothers Dual Digital model 20: Picolog 6 data logging software was used for data collection.

Calculating free palmitate concentrations

To estimate free fatty acid concentrations in the respiration chamber, we applied a widely used[24,58,59] equation established to relate the equilibrium binding of palmitate to BSA[60]. In brief, the equation is as follows: $[FFA](\upsilon) = m\upsilon + b + ce^{k\upsilon}$, where υ is the molar ratio of nominal palmitate to BSA, m, b, c and k are taken from the relationship between free fatty acid concentrations and υ[60], and e is the Euler's constant. We used 0.1% fatty acid-free BSA (Sigma-Aldrich, A6003, molecular mass of 66,000 g mol^{-1}) in the respiration buffer, which equated to 15.15 mM. The nominal concentrations of palmitate added were 20, 40, 60, 80, 100 and 150 mM, which resulted in free palmitate concentrations of 0.0068, 0.017, 0.04, 0.13, 0.52 and 22.41 mM, respectively.

Adenovirus production for *Alpl* overexpression and silencing

For overexpression of TNAP, mouse *Alpl* ORF was cloned into pENTR-dTOPO according to the manufacturer's instructions (Invitrogen; K2400-20), and point mutations (S110A, D370G, K52S) were generated through site-directed mutagenesis. Constructs were Gateway cloned into pAD-V5-DEST, and adenovirus was prepared according to the manufacturer's instructions (Invitrogen; V493-20). For *Alpl* silencing, adenovirus was prepared as described previously[3,9].

AAV production for *Alpl* overexpression

After PCR amplification, *Alpl* was cloned in the reverse orientation as SalI-HindIII fragments, into pAAV-CA-FLEX (Addgene, 38042) that had been linearized with HindIII and SalI. AAV was prepared as described previously[61], and was concentrated using AAVanced Concentration Reagent according to the manufacturer's protocol (System Biosciences, AAV100A-1). The concentrated virus was flash-frozen in liquid nitrogen and stored at −80 °C until further use. Titration of virus was carried out with PureLink Viral RNA/DNA Mini Kit (Invitrogen, 12280050) according to the manufacturer's instructions. The DNA extracted from viral samples was quantified by qPCR against a standard curve of linearized pAAV-CA-FLEX. The following primers were used: forward, CGCTGCTTT AATGCCTTTGTA; reverse, GGGCCACAACTCCTCATAAA.

Surgical iBAT injection with AAV

Mice were anaesthetized using isoflurane (2.5% isoflurane at 0.8 l oxygen per min). Before surgery, the mice received an injection of 500 µl saline and carprofen (20 $mg.kg^{-1}$). Fur directly above interscapular BAT (iBAT) was shaved and disinfected with BAXEDIN (2% (w/v) chlorhexidine gluconate in 70% (v/v) isopropyl alcohol). Once deep anaesthesia was achieved, a small incision was made above the iBAT, parallel to the spinal column. The iBAT was then separated from the subcutaneous tissue by blunt dissection. The iBAT was held in place while four AAV injections or saline for controls ($Alpl^{fl/fl}Ucp1^{fl/fl}$) were administered to each lobe (10 µl per lobe, equivalent to 1×10^{11} to 1.5×10^{11} viral infectious units). The incision site was treated with a local analgesic (lidocaine) and sutured. Mice were given daily injections of carprofen for the following 2 days, and their health was monitored after surgery for 1 week.

Preparation of Avertin

To prepare the Avertin stock solution, 25 g of 2,2,2-tribromoethanol (Millipore Sigma, T48402) was dissolved in 15.5 ml of *tert*-amyl alcohol (Millipore Sigma, 152463). The mixture was heated to 50 °C until completely dissolved while being shielded from light. For the working solution (20 mg ml^{-1}), 0.5 ml of the stock solution was diluted in 39.5 ml of sterile isotonic saline. The solution was then heated to 40 °C until fully dissolved, filtered using a 0.2-µm filter and stored at 4 °C for up to 4 months before use.

In vivo noradrenaline-induced energy expenditure

Mice were anaesthetized using an i.p. injection of Avertin (0.5 g kg^{-1} body weight, diluted in isotonic saline, administered at 25 µl g^{-1} body weight). Anaesthetized mice were then placed into individual metabolic cages (Promethion high-definition behavioural phenotyping system, Sable Systems International) set to 33 °C. Each experiment included data collection from four mice simultaneously. After anaesthesia, mice were positioned in the prone position within the metabolic cages. After an initial 8 min baseline measurement of energy expenditure, the cages were briefly opened for subcutaneous administration of noradrenaline (Sigma-Aldrich, A9512) diluted in isotonic saline to a final concentration of 0.1 mg ml^{-1}. Each mouse received 200 µl of the solution, corresponding to a dose of 20 µg (60 nmol) noradrenaline,

injected above the iBAT. Data analysis was performed using the 1-min One-Click Macro (v.2.53.2).

Cold-induced whole-body energy expenditure

iADKO$^{Alpl;Ucp1}$ mice overexpressing TNAP variants were housed in individual metabolic cages (Promethion high-definition behavioural phenotyping system, Sable Systems International) set to 30 °C for 5 days with a 12 h–12 h light–dark schedule (light from 07:00 to 19:00). For cold-mediated thermogenesis, metabolic parameters were measured for 4 h at 30 °C (20–40% humidity), then the incubator temperature was reduced in the morning (at zeitgeber time 0 (ZT0)) to 6 °C with no ramp (taking approximately 75 min to reach 6 °C) and measurements continued for an additional 3 h. To quantify cold-induced whole-body energy expenditure, we first calculated the mean basal energy expenditure (EE; −240 to −120 min at 30 °C) of the WT-rescue (AAV-WT) group, which served as the common experimental reference. For each experimental group, the difference between its mean basal EE and the mean basal EE of the WT-rescue group was then calculated. This group-level offset was subsequently subtracted from every EE measurement of all mice within that group across the entire time course, thereby adjusting basal EE across groups to the WT-rescue reference while preserving within-group interanimal variability. Cold-induced energy expenditure was quantified during the steady-state cold period (100–180 min after the start of ramp down to 6 °C, denoted by the hatched box), and group differences in the cold-evoked response were assessed using ANCOVA with body weight included as a covariate. Mice had ad libitum access to drinking water and a chow diet (3.1 kcal g^{-1} energy density) with 24%, 16% and 60% of calories from protein, fat and carbohydrate, respectively (2920X, Envigo) throughout the experiment. Data analysis was performed using the 1 min One-Click Macro (v.2.53.2).

Quantification of the FCC in mature brown adipocytes

A Clark-type electrode (Rank Brothers) was used to measure oxygen consumption in mature brown adipocytes. DMEM/F12 (Gibco, 11320033) with 10% FBS (Millipore Sigma) was added to the chamber and allowed to equilibrate with atmospheric oxygen. Then, 10,000 cells were then introduced into the chamber (final volume of 0.7 ml), maintained at 37 °C, covered with a plunger and continuously stirred. The initial rate of cellular respiration, before the addition of a thermogenic activator, was termed the basal respiration. Noradrenaline was added at a final concentration of 0.1 µM to stimulate respiration, and 5 µM oligomycin (Oligo) was added to assess ATP-linked respiration. The ATP-linked respiration rate in empty AAV-expressing cells was subtracted from all the groups to quantify TNAP-dependent respiration. To isolate the thermogenic contribution of the glycerol pocket, TNAP-dependent respiration was corrected by basal TNAP activity, as assessed by *p*-NPP hydrolysis without glycerol from the cell lysates of the same cell preparations undergoing respirometry analysis. Correction was performed by normalizing the *p*-NPP hydrolysis rates to WT-infected cells, which was set to 1. The Rank Brothers Dual Digital model 20: Picolog 6 data logging software was used for data collection.

Glycerol concentration determination in BAT

Glycerol quantification was performed using GC–MS. Ice-cold 80% methanol containing glycerol-$^{13}C_3$ as an internal standard was added to 10 mg of pulverized BAT and four ceramic beads (2.8 mm; Omni International) and was lysed by bead beating for 3 cycles of 2 min at 30 Hz on an Eppendorf TissueLyser. The samples were centrifuged at 14,000 rpm for 10 min at 1 °C, and the supernatant was dried using a vacuum centrifuge at 4 °C (LabConco), followed by derivatization, as previously described[62].

Creatine concentration determination in BAT

Creatine quantification was performed using LC–MS. All LC–MS-grade solvents and salts were purchased from Thermo Fisher Scientific: water, acetonitrile, methanol, formic acid, ammonium acetate and ammonium formate. Authentic metabolite standards were purchased from Sigma-Aldrich. Ice-cold 50% methanol (1,140 µl) containing d3-creatine as an internal standard and ice-cold acetonitrile (660 µl) were added to 10 mg of pulverized BAT and four ceramic beads (2.8 mm diameter). The samples were lysed by bead beating for 2 min at 30 Hz on the Eppendorf TissueLyser. The resulting slurries were transferred to 5 ml Eppendorf tubes, to which 1,800 µl of dichloromethane and 600 µl of water (both ice-cold) were added. The samples were vortexed for 1 min and incubated on ice for 10 min, then centrifuged at 3,082*g* for 10 min at 4 °C. The upper aqueous phase was transferred to a new tube and dried using a vacuum centrifuge at 4 °C (LabConco). The samples were resuspended in 30 µl of water and analysed using LC–MS.

The relative creatine concentrations were measured using the 6470 triple quadrupole mass spectrometer equipped with a 1290 ultra high-pressure LC system (Agilent Technologies). Chromatography separation was achieved using a Scherzo SM-C18 column (3 µm, 3.0 × 150 mm). The chromatography gradient started at 100% mobile phase A (5 mM ammonium acetate in water) with a 5 min gradient to 100% B (200 mM ammonium acetate in 20% acetonitrile/80% water) at a flow rate of 0.4 ml min^{-1}. This was followed by a 5 min hold time at 100% mobile phase B and a subsequent re-equilibration time (6 min) before the next injection. To ensure proper instrumental duty cycle, the samples were injected twice, for nucleotide and deoxynucleotide analyses (5 µl per injection).

Multiple reaction monitoring transitions were optimized using creatine (132.1 → 44.2 and 90.0) and d3-creatine (135.1 → 47.2 and 93.0) standards. An Agilent JetStream electrospray ionization source was used in positive ionization mode with a gas temperature and flow of 300 °C and 5 l min^{-1}, respectively, a nebulizer pressure of 45 p.s.i. and a capillary voltage of 3,500 V. Absolute concentrations were determined from external calibration curves prepared in water containing d3-creatine as an internal standard to correct for matrix effects. Data were analysed using MassHunter Quantitative Analysis software (Agilent Technologies, v.10.0, build 10.0.707.0).

Calculation of intracellular metabolite concentrations

BAT metabolite concentrations were calculated using the total moles of a metabolite within 10 mg of BAT, the total weight of the BAT (106 ± 20.28 mg; Supplementary Fig. 6a), the total number of adiponectin$^+$ brown adipocytes per sample (assuming 25 million adipocytes per BAT depot in mice[21]) and the volume of brown adipocytes, calculated using the equation of a sphere and a range of reported diameters (between 10 and 25 µm)[20]. In brief, the number of moles of glycerol in each sample was calculated by comparison to a glycerol standard curve. For GC–MS, samples were extracted in ice-cold 80% methanol and derivatized. Glycerol-$^{13}C_3$ was used as an internal standard in all the samples and the standard curve, and the ratio of glycerol/glycerol-$^{13}C_3$ was used for quantification. Creatine abundance was quantified by LC–MS in the same manner: samples were extracted in ice-cold 50% methanol containing d3-creatine as the internal standard, and the ratio of creatine/d3-creatine was used for quantification. The difference in creatine levels in bulk BAT between adipocyte-selective *Slc6a8;Gatm* double-KO mice (*Slc6a8;Gatm*$^{Adipoq\text{-}cre}$) and control mice (*Slc6a8*$^{fl/y}$*Gatm*$^{fl/fl}$) was deemed to be the levels of creatine within only parenchymal brown adipocytes.

Metabolite measurements in BAT from warm- and cold-exposed mice

BAT metabolites were measured using GC–MS and LC–MS, as indicated above, using a library of 271 metabolites, of which 150 were detected.

Metabolite measurements in cultured brown adipocytes

Brown adipocyte metabolites were measured using GC–MS, as indicated above, using a library of 40 metabolites, of which 38 were detected.

Crystallization and structure determination

Crystals of TNAP(S110A) (70 μM) bound to either PCr (10 mM), ATP (10 mM) or PPi (10 mM) were obtained in 0.15 M phosphate/citrate pH 4.0, 0.2 M NaCl, 0–30 mM phosphate, 0–5% glycerol and 14–16% PEG 10,000. Crystals of TNAP(D370G) with PCr were obtained in the same conditions. Before data collection, crystals were cryo-protected by adding either 20% glycerol or 20% ethylene glycol and flash-frozen in liquid nitrogen. Data were collected at a temperature of 100 K using the CMCF-BM beamline of the Canadian Light Source and MxDC software (wavelength 1.18 Å). The data were processed using DIALS[63]. The structure was determined by molecular replacement using a model of the mouse TNAP monomer generated with Phyre2 (ref. 64). Iterative cycles of model building and refinement were performed using COOT[65] and Phenix[66], resulting in models with >95% of their residues in the most favourable regions of the Ramachandran plot and none in disallowed regions (Supplementary Table 3). To determine the identities of the metal ions bound to the active site, we collected a dataset at the zinc absorption edge (9.67 KeV, corresponding to a wavelength of 1.2822 Å) and confirmed that only one Zn^{2+} ion was present in each active site. POLDER maps[67] were calculated using Phenix to confirm the presence of PCr, ATP and PP_i in the active site, as well as the five glycerol molecules found in the TNAP(S110A) structure bound to PCr.

Measuring TNAP activity by ^{31}P NMR

^{31}P and ^{1}H NMR spectra were acquired on a Varian VNMRS 500 MHz NMR spectrometer. Each spectrum was recorded in 0.6 ml of aqueous solution sample in a 5 mm NMR tube at 25 °C, with a spectral width of 50 kHz, relaxation delay of 1 s and scan number of 64. The reaction buffer (50 mM Tris, pH 9.0, 10 mM glycerol, 10 mM PCr and 0.025 μM recombinant TNAP) was made up in deuterated water. MestReNova (v.14.2.1) was used for NMR data processing and analysis. The phosphorus in PCr, Pi and glycerol phosphate (Gro3P or Gro1P) resonates at −3.18, 2.6 and 4.4 ppm, respectively. For continuous PCr phosphatase activity measurement, each reaction was initiated by mixing 10 mM PCr with 0.025 mM recombinant TNAP in an NMR tube immediately before recording the ^{31}P and ^{1}H NMR spectra at 0 min. ^{31}P NMR spectra were acquired every 2.5 min until 50% of the PCr was hydrolysed (80 min), at which point we acquired ^{31}P and ^{1}H NMR spectra. The progressing reaction remained in the NMR tube at 25 °C between measurements for the entire time course. The rate of PCr hydrolysis over 40 min (linear phase) was used to determine the K_{cat} of TNAP.

Measuring glycerol-$^{13}C_3$ by NMR

Two-dimensional heteronuclear single quantum coherence (HSQC) spectra were acquired using the 600 MHz Bruker AVIIIHD NMR spectrometer equipped with a cryogenically cooled TCI probe. Experiments were performed at 298 K using a constant-time (CT) ^{13}C HSQC pulse sequence to improve resolution of ^{13}C–^{1}H correlations and minimize *J*-modulation effects. The CT delay was set to 13.3 ms. Spectra were collected with 64 scans, a ^{1}H sweep width of 9,615 Hz sampled over 1,536 complex points, and a ^{13}C sweep width of 4,529 Hz with 128 increments. A 25% non-uniform sampling scheme was applied in the indirect (^{13}C) dimension to reduce the acquisition time while maintaining spectral quality.

UKBB phenotype processing and quality control

The UKBB is a prospective population study of around 500,000 people of European genetic ancestry aged 40–69 years (at recruitment) that has generated comprehensive genetic profiling data, including WES and array genotyping and deep phenotypic data, such as blood biomarkers and anthropometric measures[39,68,69]. We used these data to assess the phenotypic impacts of predicted deleterious variations within *ALPL* (Extended Data Fig. 9a). All phenotypes included in the analysis were extracted from the baseline study visit. Anthropometric traits (height, sitting height, body mass index (BMI), total fat percentage by impedance) were included. The waist-to-hip ratio (WHR) was calculated as the ratio of the waist and hip circumferences. BMI-adjusted values for WHR, waist circumference and hip circumference were calculated by adjusting values by BMI, age and age^2 in a linear regression model, separately by sex. We also examined systolic and diastolic blood pressure levels, calculated as the mean of two automatic readings taken for each measurement. We assessed the association with circulating alkaline phosphatase (alp) activity, the protein for which ALPL/TNAP encodes. Moreover, we considered the following blood biomarkers: bone related: calcium (ca) and phosphate (phos); glycaemic: HbA1c and random glucose; lipid: triglycerides (tg), high-density lipoprotein (HDL) cholesterol and low-density lipoprotein (LDL) cholesterol; liver related: gamma glutamyl transferase (ggt), alanine transaminase (alt), aspartate amino transferase (ast). All blood biomarkers except for HbA1c were measured in the serum. Biomarkers that were not normally distributed were log transformed. Individuals with values more than 5 s.d. away from a trait's median value were set to missing. For triglycerides and HDL and LDL cholesterol, we excluded individuals who reported taking lipid lowering medications. For HbA1c, individuals who were diagnosed with diabetes at the time of measurement were excluded. All traits were normalized using inverse rank normal transformation so all effect sizes in the downstream analyses are comparable across phenotypes.

Genomic data quality control and annotation

We conducted all genotype quality control and downstream analyses on the UKBB Research Analysis Platform (RAP; https://ukbiobank.dnanexus.com). For WES data, we used the pre-processed .bgen files provided on the RAP and filtered variants to only include those with >90% genotypes (<10% missingness) and read depth (DP) > 10, using a helper file provided by DNAnexus on the RAP. We used the ENSEMBL Variant Effect Predictor (VEP; v.104) to annotate *ALPL* variants of interest[70], and the REVEL[71], CADD[72] and LOFTEE[73] plugins for variant annotation. We also extracted the predicted impacts of missense variants identified by AlphaMissense[74]. *ALPL* variants were sorted into the following gene burden analysis categories based on their annotations (Supplementary Table 11): Missense: any variant where a single base pair substitution results in an amino acid change. Four categories of missense variants were assessed: (1) all: all missense variants, regardless of predicted impact; loose: missense variants with a CADD score > 20 or REVEL score > 0.5; stringent: missense variants with a CADD score > 20 and REVEL score > 0.5; AlphaMissense pathogenic: missense variants predicted to be 'likely pathogenic' by AlphaMissense. PTVs: variants predicted to result in protein truncation, classed by the VEP as frameshift, stop gain or splice-site variants. Synonymous: single base pair substitutions that do not change the amino acid. For the genotype array data, which were used as a reference to estimate relatedness in the rare variant burden analysis (see below), we performed quality control and variant filtering using Plink2 (ref. 75) (v.2.00a3.1LM) with the DNAnexus Swiss Army Knife tool (v.4.9.1), using the following options to filter the data for input into REGENIE: --mac 100 --maf 0.01 --hwe 1e-15 --mind 0.1 --geno 0.1. The array single-nucleotide polymorphisms that met these criteria were used as an inclusion list for rare variant burden analysis.

Rare variant burden analysis

Rare variant burden analysis was conducted for all *ALPL* variants with a minor allele frequency <1% that could be categorized into the variant classes described above (Supplementary Table 11) using REGENIE

(v.3.1.1)[76] with the DNAnexus Swiss Army Knife tool (v.4.9.1), a two-step process that accounts for relatedness, population structure and polygenicity. First, we used step 1 to fit a model for each phenotype using a subset of genetic variants directly genotyped by the array. This enables the identification of phenotype variances attributable to genetic effects and generates leave-one-chromosome-out predictors for each trait. In both steps, models were adjusted for age, age^2, sex and the first 10 genetic principal components (PCs derived from the genotype array data). In step 1, we included an additional covariate to account for the type of genotyping array. In step 2, we included adjustments for the exome sequencing batch and the LOCO predictor generated in step 1.

In step 2, association analyses were performed in individuals of European genetic ancestry in the UKBB with WES and genotype array data (n = 421,787) for each trait of interest. The final sample sizes of traits varied due to differences in missingness. Variant sets were defined as described above, including all variants with a minor allele frequency (MAF) < 1%. Separate analyses were performed for variants in residues in homologous amino acid positions to the residues in the glycerol pocket (Asn49, Lys52, Asn53, Arg321, Gly326, Phe327, Ser367, Asp370, Thr371), and other functional domains of interest (Supplementary Table 5), and the remainder of variants outside of these *ALPL* domains grouped as a 'rest_of_TNAP' group. Analyses were additionally conducted for the full gene body: all sites. We also conducted the same analyses not restricting by MAF and in addition only considering common variants (MAF > 1%) to determine the contribution of more common variation on phenotypes of interest (Supplementary Table 12).

We conducted our analyses in two stages. In the first, we focused on traits that are clinically relevant to patients carrying pathogenic *ALPL* mutations—plasma alkaline phosphatase activity and traits related to bone mineralization (heel bone mineral density and circulating calcium and phosphate levels). We considered significant associations at a Bonferroni significance threshold (P < 0.0016) accounting for the number of phenotypes tested (n = 4) and number of gene burden masks assessed across both domains of interest (n = 4; total n tests = 32). Associations were considered nominally significant if 0.0016 < P < 0.05, and not significant if P > 0.05. In the second stage, we also assessed the associations of *ALPL* variant masks with other traits, particularly nominally significant (P < 0.05) variants in the glycerol pocket, to identify possible associations with a wider range of anthropometric and blood biomarker traits. This was to identify if there are any additional phenotypes associated with *ALPL* loss of function at the population level that were not reported in patient cohorts. We conducted further sensitivity analyses stratified by sex to identify any possible sexually dimorphic associations in both analysis stages.

To compare the effect estimates identified for different domains of interest on the four primary phenotypes of interest we also calculated the z-statistic and corresponding P values for this comparison, to compare the relative impact of these to the 'all sites' and 'rest of TNAP' variant groups. The z-statistic was calculated as follows: $z = \frac{\hat{\beta}_1 - \hat{\beta}_2}{\sqrt{SE^2_{\hat{\beta}_1} + SE^2_{\hat{\beta}_2}}}$.

Osteoblast differentiation and mineralization assays in vitro

Murine calvarial osteoblasts (MC3T3-E1, subclone 14) were provided by R. T. Franceschi. MC3T3-E1, subclone 14 was authenticated based on capacity to differentiate into osteoblasts with a collagen-rich matrix and mineralization[77]. The cells were cultured in a humidified incubator at 37 °C with 5% CO_2 in a modified minimum essential medium (MEM) (Thermo Fisher Scientific, Gibco) supplemented with 10% FBS (Thermo Fisher Scientific, Hyclone), along with 1% penicillin–streptomycin, 1% L-glutamine and 0.225 mM L-aspartic acid (Thermo Fisher Scientific, Gibco). All cultures were conducted in 24-well cell culture plates (Sarstedt) at a plating density of 50,000 cells per cm^2. Cell differentiation and mineralization were initiated 24 h after plating by replacing the medium with fresh MEM including 10% FBS, 50 μg ml^{-1} ascorbic acid (AA) (Sigma-Aldrich, A4034) and 10 mM β-glycerophosphate (β-GP) (Sigma-Aldrich, G9422) for baseline control mineralization conditions. The medium was changed every 48 h until the end of the experiment on day 12 (ref. 77). For mineralization inhibition experiments, starting from day 4, MEM was further supplemented with either 5.0 μM sodium pyrophosphate tetrabasic (PP_i) (Sigma-Aldrich, P8010) alone or in combination with mouse WT TNAP or various mouse mutant TNAPs (K52S, D370G and S110A, used at 5 U ml^{-1} final concentration) or with human WT or various human mutant TNAPs (N49I, N49K, F327C, F327L and S110A, used at a final concentration of 3 U ml^{-1}).

Assessment of osteoblast cell culture mineralization by von Kossa staining

Mineral was visualized in culture plates by von Kossa staining at each timepoint (days 8, 10 and 12). The cultures were rinsed once with 1× PBS and then fixed for 10 min with 95% ethanol at 37 °C. After fixation, the cultures were hydrated several times with distilled H_2O. In vitro mineralization was detected by incubating the cells with a 5% silver nitrate solution (Thermo Fisher Scientific, S181-25) for 1 h at 37 °C, followed by exposure to bright light after rinsing with distilled H_2O. The black-stained mineralized regions were recorded using an Epson Perfection 2400 Photo scanner[77].

Assessment of osteoblast cell culture mineralization and calcium content by Alizarin Red staining

Cultures were rinsed once with 1× PBS and fixed with 70% ethanol for 1 h at −20 °C. After rinsing with distilled H_2O, the mineral in the cultures was stained with 40 mM Alizarin Red S (pH 4.2) (Sigma-Aldrich, A5533) for 10 min at room temperature, followed by rinsing five times with distilled water and once with 1× PBS for 15 min. After air drying, the stained cultures were photographed using an Epson Perfection 2400 Photo scanner. For stain quantification to assess mineral deposition, the stain was then dissolved for each timepoint (day 8, 10 and 12) in 10% (w/v) cetylpyridinium chloride (CPC) (Sigma-Aldrich, C5460) in 10 mM sodium phosphate solution (pH 7.0) for 15 min and then transferred to a 96-well plate. Absorbance at 562 nm was measured using a spectrophotometer (Tecan INFINITE 200 PRO).

HDX–MS analysis

TNAP variants were buffer exchanged into equilibration buffer (20 mM HEPES, 200 mM NaCl, 2 mM $MgCl_2$, pH 8.0 in H_2O) using 30 kDa Amicon Ultra centrifugal filters (Sigma-Millipore) before HDX-MS analysis. Full-length recombinant TNAP (residues 17–498) stock solutions were prepared at a concentration of 30 μM for HDX-MS analyses. Deuterium labelling was initiated by a 19-fold dilution into D_2O buffer (20 mM HEPES, 200 mM NaCl, 2 mM $MgCl_2$, 25 mM $ZnCl_2$, pH 8.0). Labelling was performed at 20 °C and quenched at designated timepoints by adding an equal volume of ice-cold quench buffer (2 M GnHCl, 0.8% formic acid, pH 2.23). For the WT TNAP and TNAP(D404A) comparison, labelling timepoints were 10 s, 1 min, 10 min, 1 h and 4 h. For TNAP alone and in the presence of substrates, timepoints included 10 s, 1 min, 5 min, 10 min, 30 min and 1 h. Substrate incubations were performed as follows. For TNAP with glycerol, the protein was pre-incubated with 5 mM glycerol for 10 min and 10% (v/v) glycerol was maintained in the D_2O labelling buffer. For TNAP with PCr, 5 mM PCr was pre-incubated for 10 min, and 5 mM PCr was also maintained in the D_2O buffer. For TNAP incubated with both glycerol and PCr, 5 mM of each was pre-incubated with the protein and maintained at 10% and 5 mM, respectively, in the D_2O labelling buffer. Online protein digestion was performed using an Affipro pepsin column held at 15 °C and resultant peptides were trapped and desalted on a VanGuard Pre-column trap for 3 min at 100 μl min^{-1}. Peptides were then eluted from the trap and separated using a 5–35% gradient of acetonitrile over 6 min at a flow rate of 100 μl min^{-1} using an ACQUITY UPLC HSS T3 1.8 μm, 1.0 mm × 50 mm reversed-phase

column. Both the desalting and separation columns were housed in a Waters HDX cooling chamber that was held at 0 °C. Mass spectra were analysed using the Waters SELECT SERIES Cyclic IMS operated in HDMS^E. Peptide identification was performed from replicates of undeuterated control samples using PLGS v.3.0.3 (Waters) as described in Supplementary Table 4. The peptides identified in PLGS were then analysed in DynamX v.3.0 (Waters) with a minimum products per amino acid cut-off of 0.25 and at least two consecutive product ions (Supplementary Table 4). Those peptides meeting initial filtering criteria were further processed by DynamX 3.0. The relative deuterium incorporation of each peptide was calculated for each timepoint and condition tested by subtracting the centroid mass of the undeuterated from the deuterated form. The resulting values were used to produce the graphs of deuterium uptake and the difference maps. The average deuterium incorporation error for each peptide was at or below ±0.25 Da. The deuterium levels were not corrected for back exchange and therefore indicated as relative[78].

Statistical analyses

Statistical analyses were performed with GraphPad Prism 10. Data analyses were performed using Microsoft Office Excel (v.16.56). Data are mean ± s.e.m. of biologically independent samples. We used unpaired two-tailed Student's *t*-tests for pairwise comparisons and one-way and two-way ANOVA for multiple comparisons involving two independent variables, with $P < 0.05$ considered statistically significant. The specific *n* values noted in each figure legend represent independent biological replicates.

Statistics and reproducibility

Sample sizes (biological replicates) for each experiment are reported in the figure legends. The numbers of experimental repetitions were as follows: Fig. 1e: 2 times; Fig. 2e,f: 2 times; Fig. 3i,k,m: 2 times; Fig. 5c: 4 times; Fig. 5e: 8 times; Extended Data Fig. 1e: 2 times; Extended Data Fig. 1k: 1 time; Extended Data Fig. 1s: 2 times; Extended Data Fig. 2a–c: 2 times; Extended Data Fig. 4a,e: 4 times; and Extended Data Fig. 7c,f,m: 2 times.

Materials and resources availability

Please address correspondence and requests for materials, resources, and reagents to the corresponding author. All materials generated in this study are available from the corresponding author with a completed material transfer agreement.

Reporting summary

Further information on research design is available in the Nature Portfolio Reporting Summary linked to this article.

Data availability

All data supporting the findings of this study are available within the Article and its Supplementary Information. Any additional information required to reanalyse the data reported in this Article is available from the corresponding author on request. Atomic coordinates and structure factors have been deposited in the Protein Data Bank under accession codes 10TV (TNAP(S110A) with PCr and glycerol), 10TW (TNAP(D370G) with glycerol), 10TX (TNAP(S110A) with PP_i and glycerol), 10TY (TNAP(S110A) with PP_i and ethylene glycol), 10TZ (TNAP(S110A) with ATP and glycerol). HDX MS proteomics data have been deposited to the ProteomeXchange Consortium via the PRIDE[79] partner repository with the dataset identifier PXD067887. All individual-level data in the UKBB study are publicly available to bona fide researchers through the UKBB data access protocol. Information about registration for access to the data is available online (https://www.ukbiobank.ac.uk/enable-your-research/apply-for-access). Source data are provided with this paper.

Code availability

The code for the analyses of UKBB data included in this manuscript is freely available at GitHub (https://github.com/comp-med/tnap-alpl-ukb) and permanently archived at Zenodo (https://doi.org/10.5281/zenodo.18606385)[80].

54. Sassmann, A., Offermanns, S. & Wettschureck, N. Tamoxifen-inducible Cre-mediated recombination in adipocytes. *Genesis* **48**, 618–625 (2010).
55. Kong, X. et al. Brown adipose tissue controls skeletal muscle function via the secretion of myostatin. *Cell Metab.* **28**, 631–643 (2018).
56. Cohen, P. et al. Ablation of PRDM16 and beige adipose causes metabolic dysfunction and a subcutaneous to visceral fat switch. *Cell* **156**, 304–316 (2014).
57. Laemmli, U. K. Cleavage of structural proteins during the assembly of the head of bacteriophage T4. *Nature* **227**, 680–685 (1970).
58. Hofmann, W. E., Liu, X., Bearden, C. M., Harper, M. E. & Kozak, L. P. Effects of genetic background on thermoregulation and fatty acid-induced uncoupling of mitochondria in UCP1-deficient mice. *J. Biol. Chem.* **276**, 12460–12465 (2001).
59. Matthias, A. et al. Thermogenic responses in brown fat cells are fully UCP1-dependent. UCP2 or UCP3 do not substitute for UCP1 in adrenergically or fatty scid-induced thermogenesis. *J. Biol. Chem.* **275**, 25073–25081 (2000).
60. Richieri, G. V., Anel, A. & Kleinfeld, A. M. Interactions of long-chain fatty acids and albumin: determination of free fatty acid levels using the fluorescent probe ADIFAB. *Biochemistry* **32**, 7574–7580 (1993).
61. Johansen, O. S. et al. Lipolysis drives expression of the constitutively active receptor GPR3 to induce adipose thermogenesis. *Cell* **184**, 3502–3518 (2021).
62. Gravel, S. P., Avizonis, D. & St-Pierre, J. Metabolomics analyses of cancer cells in controlled microenvironments. *Methods Mol. Biol.* **1458**, 273–290 (2016).
63. Winter, G. et al. DIALS: implementation and evaluation of a new integration package. *Acta Crystallogr. D* **74**, 85–97 (2018).
64. Kelley, L. A., Mezulis, S., Yates, C. M., Wass, M. N. & Sternberg, M. J. The Phyre2 web portal for protein modeling, prediction and analysis. *Nat. Protoc.* **10**, 845–858 (2015).
65. Emsley, P. & Cowtan, K. Coot: model-building tools for molecular graphics. *Acta Crystallogr. D* **60**, 2126–2132 (2004).
66. Liebschner, D. et al. Macromolecular structure determination using X-rays, neutrons and electrons: recent developments in Phenix. *Acta Crystallogr. D* **75**, 861–877 (2019).
67. Liebschner, D. et al. Polder maps: improving OMIT maps by excluding bulk solvent. *Acta Crystallogr. D* **73**, 148–157 (2017).
68. Backman, J. D. et al. Exome sequencing and analysis of 454,787 UK Biobank participants. *Nature* **599**, 628–634 (2021).
69. Bycroft, C. et al. The UK Biobank resource with deep phenotyping and genomic data. *Nature* **562**, 203–209 (2018).
70. McLaren, W. et al. The Ensembl Variant Effect Predictor. *Genome Biol.* **17**, 122 (2016).
71. Ioannidis, N. M. et al. REVEL: an ensemble method for predicting the pathogenicity of rare missense variants. *Am. J. Hum. Genet.* **99**, 877–885 (2016).
72. Rentzsch, P., Witten, D., Cooper, G. M., Shendure, J. & Kircher, M. CADD: predicting the deleteriousness of variants throughout the human genome. *Nucleic Acids Res.* **47**, D886–D894 (2019).
73. Karczewski, K. J. et al. The mutational constraint spectrum quantified from variation in 141,456 humans. *Nature* **581**, 434–443 (2020).
74. Cheng, J. et al. Accurate proteome-wide missense variant effect prediction with AlphaMissense. *Science* **381**, eadg7492 (2023).
75. Purcell, S. et al. PLINK: a tool set for whole-genome association and population-based linkage analyses. *Am. J. Hum. Genet.* **81**, 559–575 (2007).
76. Mbatchou, J. et al. Computationally efficient whole-genome regression for quantitative and binary traits. *Nat. Genet.* **53**, 1097–1103 (2021).
77. Addison, W. N. et al. Extracellular matrix mineralization in murine MC3T3-E1 osteoblast cultures: an ultrastructural, compositional and comparative analysis with mouse bone. *Bone* **71**, 244–256 (2015).
78. Wales, T. E. & Engen, J. R. Hydrogen exchange mass spectrometry for the analysis of protein dynamics. *Mass Spectrom. Rev.* **25**, 158–170 (2006).
79. Perez-Riverol, Y. et al. The PRIDE database at 20 years: 2025 update. *Nucleic Acids Res.* **53**, D543–D553 (2025).
80. Williamson, A. Analysis code for Hussain et al (2026) Nature. *Zenodo* https://doi.org/10.5281/zenodo.18606386 (2026).

Acknowledgements UKBB analyses were conducted under application 44448. X-ray diffraction data were collected using beamline CMCF-BM at the Canadian Light Source, a national research facility supported by the Canada Foundation for Innovation (CFI), the Natural Sciences and Engineering Research Council (NSERC), the National Research Council (NRC), the Canadian Institutes of Health Research (CIHR), the Government of Saskatchewan and the University of Saskatchewan. We acknowledge technical assistance from S. Colville, D. Lang, T. Sprules and the staff at the Rosalind & Morris Goodman Cancer Institute Metabolomics Innovation Resource (MIR) at McGill University. MIR is supported by the Terry Fox Foundation, Quebec Breast Cancer Foundation, The Dr. R. John Fraser and Mrs. Clara M. Fraser Memorial Trust, and McGill University. This work was supported by CIHR Project Grants (PJT-159529 and PJT-180557 to L.K.; PJT-155941 to A.G.; and PJT-175089 to M.D.M.), NSERC Discovery Grants (to L.K. and A.G.) and the CFI John R. Evans Leaders Fund (37919 to L.K.); a NSERC Canada Graduate Scholarship—Doctoral (to M.F.H.); a Graduate Scholarship from the Fonds de Recherche de Quebec—Santé (FRQS) (to S.S.K. and J.B.); and a postdoctoral FRQS scholarship (to B.L.C.). M.D.M. and A.G. are members of the FRQS funded Centre de Recherche en Biologie Structurale. M.D.M. is also a member of the FRQS Network for Oral and Bone Health. M.D.M., A.G. and L.K. are Canada Research Chairs in biomineralization, macromolecular machines in DNA repair and adipocyte biology, respectively.

Author contributions L.K. and M.F.H. conceived the project. M.F.H., S.S.K., B.L.C., A.M., B.Y.S., J.F.R., T.E.W., C.L., M.D.M., A.G. and L.K. designed the experiments. M.F.H., S.S.K., B.L.C., B.S., A.M., B.Y.S., J.B., M.D.-M., J.F.R., A.O., A.R., Z.K., M.E., Q.Z., M.G.M., A.S., J.C., H.K. and V.E.D. performed experiments. M.F.H., S.S.K., B.L.C., B.S., A.M., A.W., B.Y.S., J.F.R., C.J.R., J.L.M., T.E.W., C.L., M.D.M., A.G. and L.K. analysed and interpreted data. K.K.I. assisted with insect cell protein expression. S.S.K., B.L.C. and A.G. designed, conducted and interpreted the structural studies. A.W. and C.L. conducted gene burden analyses using the UKBB. L.K. wrote the manuscript. All of the authors reviewed and edited the manuscript. L.K. supervised the project.

Competing interests The authors declare no competing interests.

Additional information

Supplementary information The online version contains supplementary material available at https://doi.org/10.1038/s41586-026-10396-9.

Correspondence and requests for materials should be addressed to Lawrence Kazak.

Peer review information *Nature* thanks Jonathan Brestoff and the other, anonymous, reviewer(s) for their contribution to the peer review of this work.

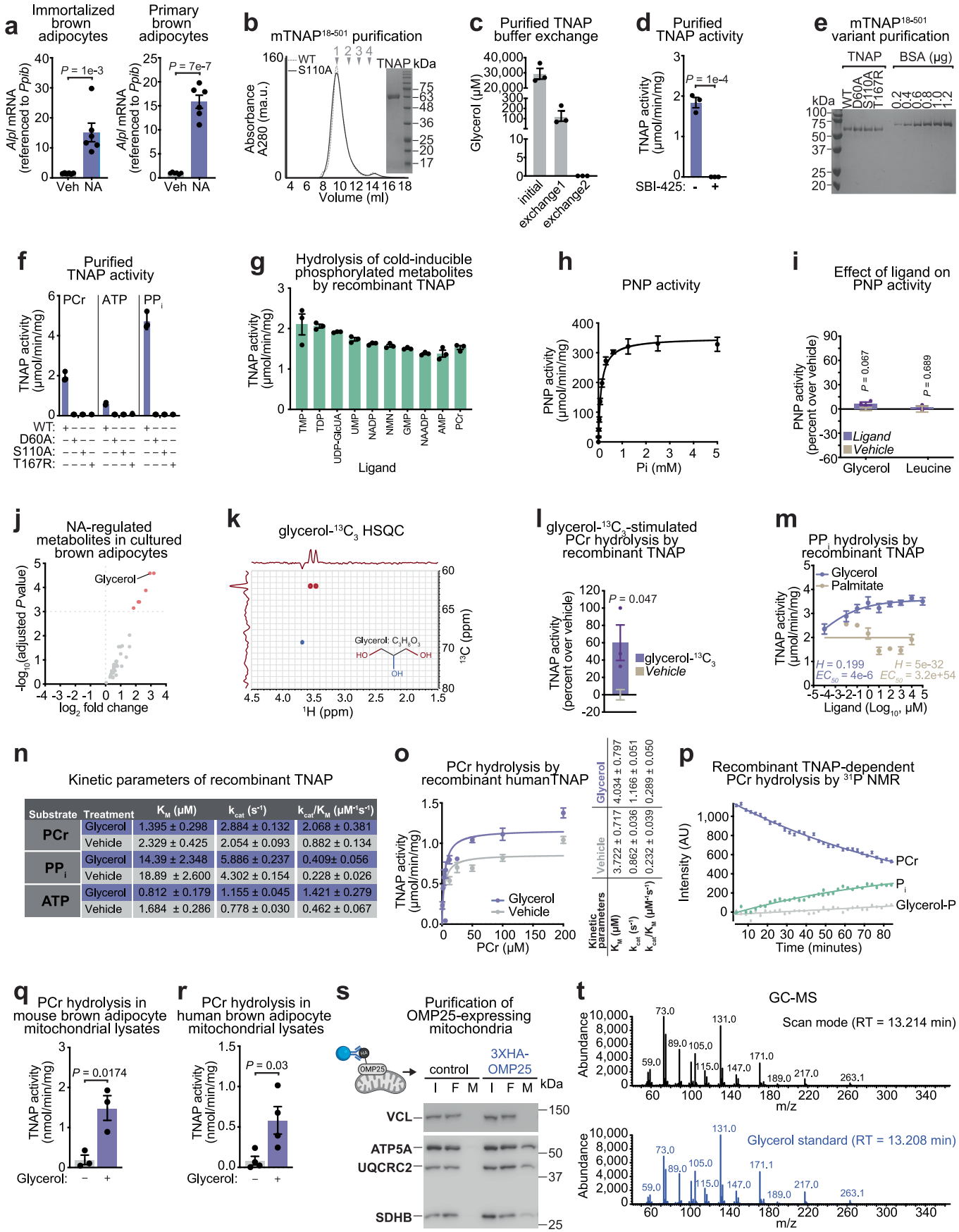

Substrate	Treatment	K_M (μM)	k_{cat} (s^{-1})	k_{cat}/K_M ($\mu M^{-1}s^{-1}$)
PCr	Glycerol	1.395 ± 0.298	2.884 ± 0.132	2.068 ± 0.381
	Vehicle	2.329 ± 0.425	2.054 ± 0.093	0.882 ± 0.134
PP_i	Glycerol	14.39 ± 2.348	5.886 ± 0.237	0.409± 0.056
	Vehicle	18.89 ± 2.600	4.302 ± 0.154	0.228 ± 0.026
ATP	Glycerol	0.812 ± 0.179	1.155 ± 0.045	1.421 ± 0.279
	Vehicle	1.684 ± 0.286	0.778 ± 0.030	0.462 ± 0.067

Glycerol	4.034 ± 0.797	1.166 ± 0.051	0.289 ± 0.050
Vehicle	3.722 ± 0.717	0.862 ± 0.036	0.232 ± 0.039
Kinetic parameters	K_M (μM)	k_{cat} (s^{-1})	k_{cat}/K_M ($\mu M^{-1}s^{-1}$)

Extended Data Fig. 1 | See next page for caption.

Extended Data Fig. 1 | Glycerol-induced TNAP activation and mitochondrial transit. a, *Alpl* mRNA levels after 24 h stimulation with noradrenaline (1 µM) (n = 6/group). **b**, Size-exclusion chromatography of catalytically inactive TNAP (S110A, solid) and wild-type TNAP (WT, dashed) on Superdex 200; elution volumes correspond to 156 (1), 142 (2), 114 (3), and 62 (4) kDa, with a Coomassie-stained gel of purified recombinant TNAP-WT shown. **c**, Glycerol levels during buffer exchange of purified recombinant TNAP-WT (n = 3/group). **d**, TNAP-dependent hydrolysis of phosphocreatine (PCr, 10 mM), with inhibition by SBI-425 (10 µM) (n = 3/group). **e**, Coomassie-stained polyacrylamide gel of purified recombinant TNAP variants. **f**, Enzymatic activity of TNAP variants toward distinct substrates (10 mM each; n = 3/group). **g**, Hydrolysis of phosphorylated metabolites by recombinant TNAP-WT (n = 3/group). **h**, Michaelis–Menten kinetics of inorganic phosphate (P_i)-stimulated purine nucleoside phosphorylase (PNP) activity (n = 3/group). **i**, Ligand (1 mM)-induced PNP activity using P_i (150 µM) (n = 3/group). **j**, NA-regulated metabolites in brown adipocytes (n = 3/group). **k**, glycerol-$^{13}C_3$ heteronuclear single quantum coherence (HSQC). **l**, glycerol-$^{13}C_3$ 1 mM)-induced PCr hydrolysis by recombinant TNAP-WT (n = 3/group). **m**, Hydrolysis of pyrophosphate (PP_i) by recombinant TNAP-WT (n = 3/group). **n**, Kinetic parameters for recombinant TNAP-WT hydrolysis of multiple substrates (n = 3/group, from Fig. 1d). **o**, Michaelis–Menten kinetics of PCr hydrolysis by recombinant TNAP-WT in the absence or presence of glycerol (n = 3/group). **p**, Accumulation of P_i and glycerol phosphate (Glycerol-P) during PCr (10 mM) hydrolysis by recombinant TNAP-WT measured by ^{31}P NMR (from Fig. 1e). **q-r**, Glycerol (1 mM)–induced PCr hydrolysis in (**q**) mouse and (**r**) human brown adipocyte mitochondrial lysates mediated by endogenous TNAP, defined as portion of hydrolysis inhibited by SBI-425 (10 µM), at pH 7.2 (mouse, n = 3/group; human, n = 3/group). **s**, Schematic and immunoblot of rapid HA-affinity mitochondrial purification (I, input; F, flowthrough; M, mitochondria). Created in BioRender. Kazak, L. (2026) https://BioRender.com/7kh1mnl. **t**, GC–MS analysis of glycerol in rapidly purified mitochondria (black trace) and a glycerol standard (blue trace). Data are presented as mean values ± SEM of biologically independent samples. **a, d, l, q, r**, two-tailed Student's t-tests; **i**, multiple two-tailed Student's t-tests; **j**, Nominal p-values were adjusted for multiple comparisons using the Benjamini-Hochberg false discovery rate (FDR) method; **m, o**, non-linear regression.

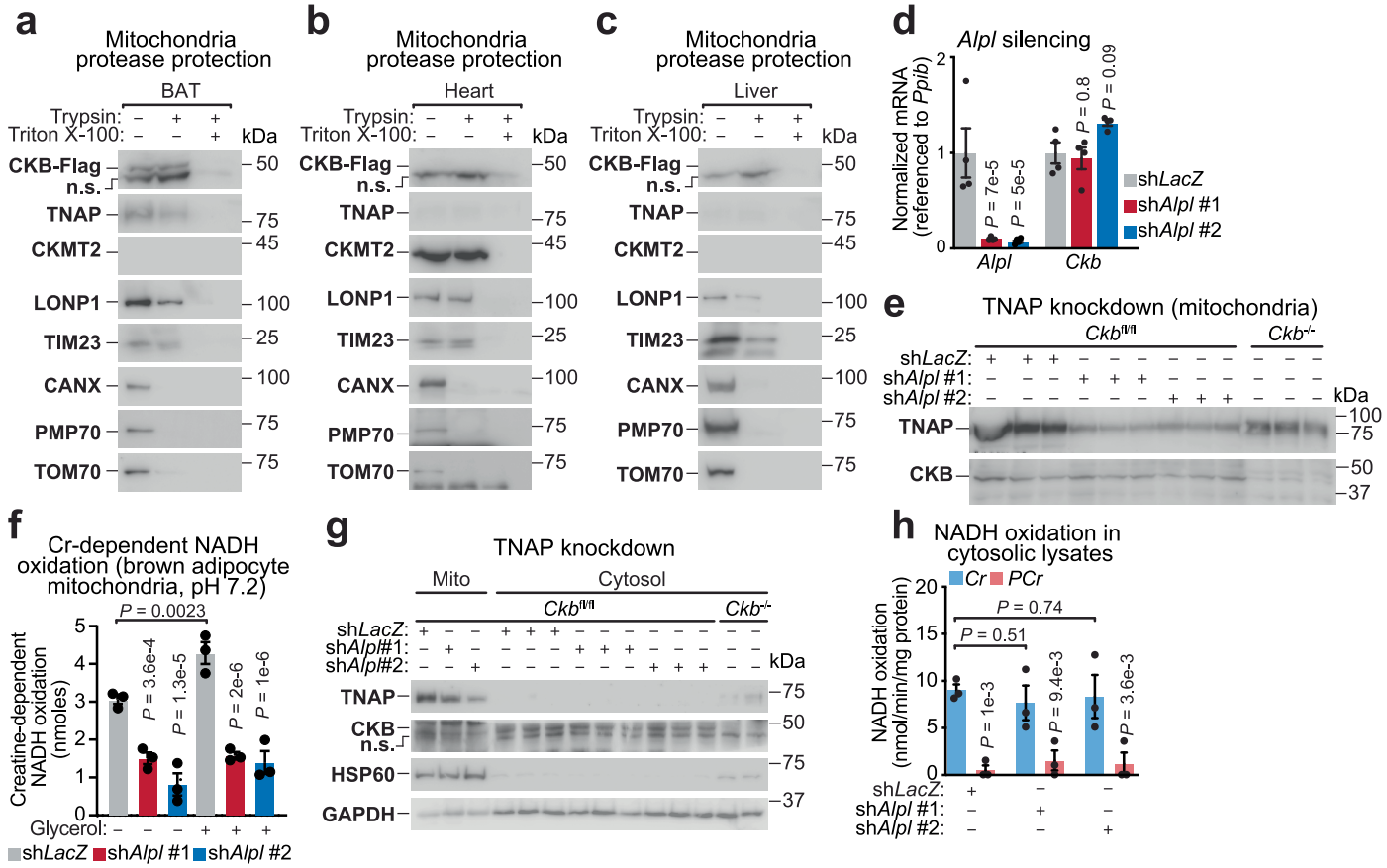

Extended Data Fig. 2 | TNAP-dependent FCC activation in brown adipocyte mitochondria. a-c, Protease protection assays of mitochondria isolated from (**a**) brown adipose tissue (BAT), (**b**) heart, and (**c**) liver of *Ckb*^{FLAG} mice housed at room temperature (22 °C ± 1 °C). **d**, RT-qPCR of immortalized brown adipocytes following *Alpl* silencing (n = 4/group). **e**, Western blot analysis of mitochondria isolated from immortalized brown adipocytes following *Alpl* silencing. **f**, NADH oxidation in mitochondrial extracts from immortalized brown adipocytes initiated with limiting creatine (2 nmol) at pH 7.2 (n = 3/group). **g**, Western blot analysis of cytosolic fractions from control and TNAP-depleted *Ckb*$^{fl/fl}$ brown adipocytes; mitochondrial extracts from *Ckb*$^{fl/fl}$ and cytosolic extracts from *Ckb*$^{-/-}$ brown adipocytes serve as controls for subcellular enrichment and CKB antibody validation, respectively. **h**, Creatine (Cr)- and phosphocreatine (PCr)-driven NADH oxidation in cytosolic lysates from immortalized brown adipocytes (n = 3/group). Data are presented as mean values ± SEM of biologically independent samples. **d, h, f**, two-way analysis of variance (ANOVA; Fisher's least significance difference (LSD)).

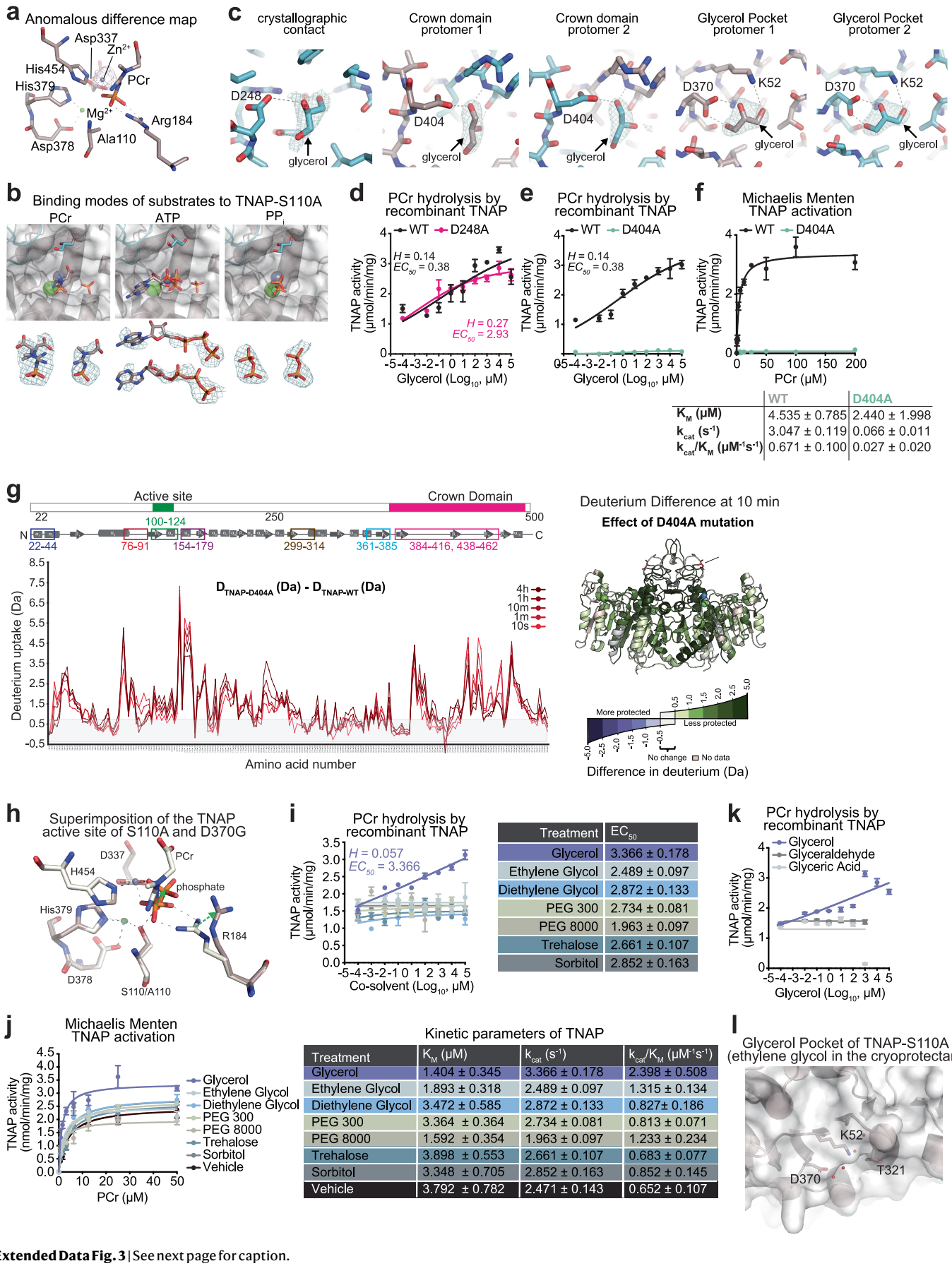

Extended Data Fig. 3 | See next page for caption.

Extended Data Fig. 3 | Structure-function analysis of TNAP. a, Active-site residues of TNAP-S110A bound to phosphocreatine (PCr) shown as sticks; the anomalous electron density map (contoured at 5σ) calculated from data collected at the Zn^{2+} anomalous scattering edge (9.67 KeV) is shown as a purple mesh. **b**, Comparison of PCr (left), ATP (centre), and PP_i (right) binding modes in the TNAP-S110A active site; PCr- and ATP-bound structures contain an additional phosphate ion. Bottom panels show polder omit maps for each ligand bound to both protomers, contoured at 6σ (PCr, PP_i) or 3σ (ATP). **c**, Close-up views of five glycerol molecules in the TNAP-S110A–PCr structure, coloured as in Fig. 3a, with polder omit maps contoured at 6σ; coordinating residues are labelled and hydrogen bonds shown as dashed lines. **d-e**, Glycerol-induced PCr (3 μM) hydrolysis by (**d**) recombinant TNAP-WT and TNAP-D248A or (**e**) recombinant TNAP-WT and TNAP-D404A (n = 3/group). **f**, Michaelis-Menten kinetics of PCr hydrolysis by recombinant TNAP-WT and TNAP-D404A (n = 3/group). **g**, Mutation-induced changes in TNAP backbone dynamics, shown as a linear map of secondary structural elements and HDX–MS difference profiles (TNAP-D404A minus TNAP-WT), with regions of differential deuterium incorporation mapped onto the TNAP structure. **h**, Superposition of PCr-bound TNAP-S110A (white) and TNAP-D370G (brown) active sites, highlighting hydrogen-bond networks coordinating PCr (TNAP-S110A) or the leaving phosphate ion (TNAP-D370G); Zn^{2+} and Mg^{2+} ions are shown as purple and green spheres, respectively. **i**, Effects of cosolvent ligands on PCr hydrolysis by recombinant TNAP-WT (n = 3/group). **j**, Michaelis-Menten kinetics of PCr hydrolysis by recombinant TNAP-WT in the presence of cosolvents (1 mM) (n = 3/group). **k**, PCr hydrolysis by recombinant wild-type mouse TNAP (n = 3/group). **l**, Close-up of the Glycerol Pocket in TNAP-S110A bound to PCr when glycerol is replaced by ethylene glycol in the cryoprotectant, shown in the same orientation and style as Fig. 3d,f. Data are presented as mean values ± SEM of biologically independent samples. **d-f**, **i**, **j**, **k**, non-linear regression.

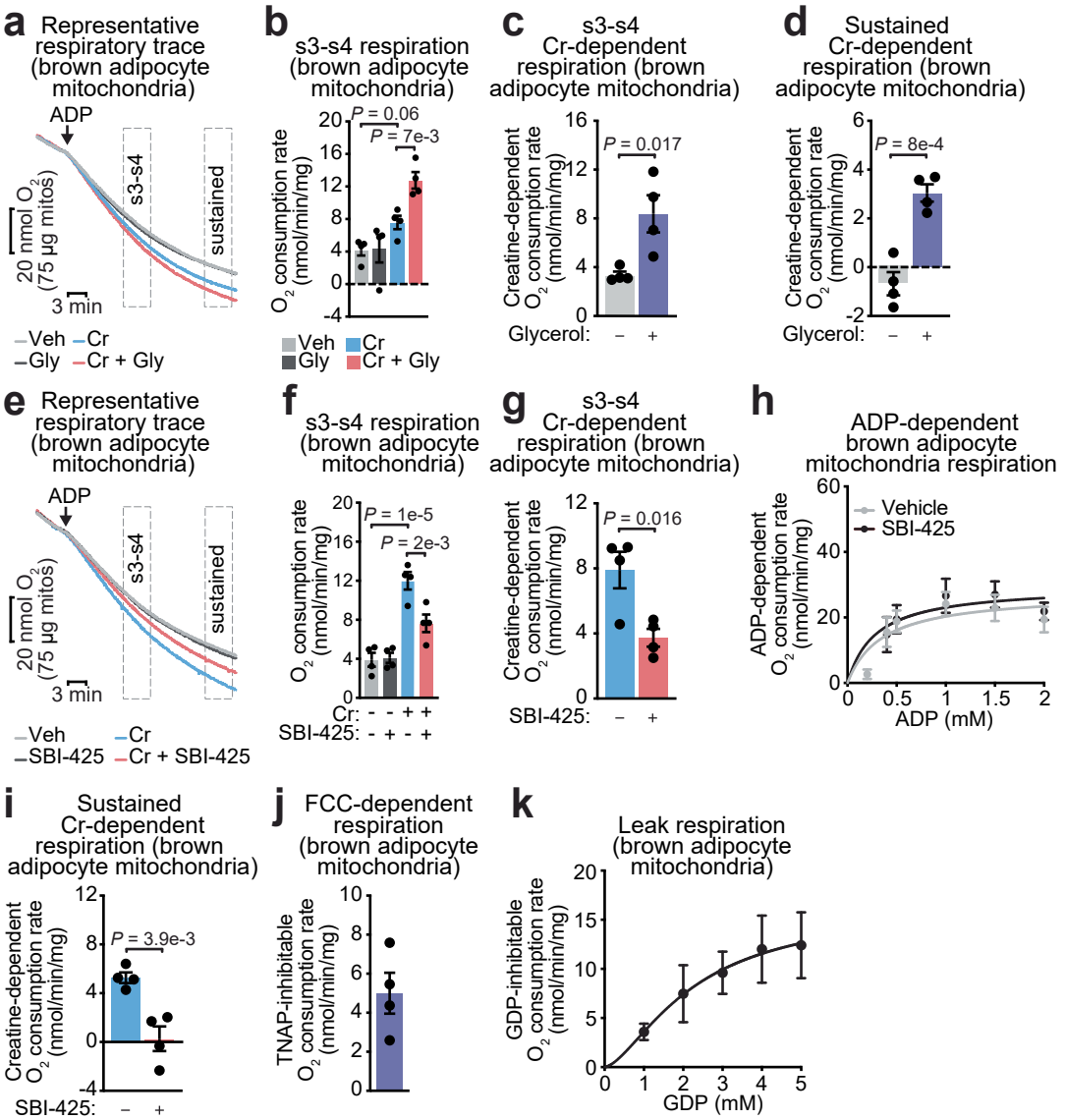

Extended Data Fig. 4 | The FCC in cultured brown adipocyte mitochondria. **a**, Representative oxygen consumption traces following addition of ADP (280 nmol). The transition from state 3 to state 4 respiration (s3-s4) is indicated by the hashed box labelled, and sustained state 4 respiration by the box labelled "sustained". Conditions: vehicle (Veh), glycerol (Gly, 1 mM), and creatine (Cr, 1 mM). **b**, Instantaneous O_2 consumption rates during the s3-s4 transition from Extended Data Fig. 4a ($n = 4$/group). **c**, Cr-dependent O_2 consumption rates from Extended Data Fig. 4b ($n = 4$/group). **d**, Sustained Cr-dependent O_2 consumption rates derived from Extended Data Fig. 4a ($n = 4$/group). **e**, Representative oxygen consumption traces as in Extended Data Fig. 4a, with glycerol present in all conditions (1 mM) and TNAP inhibition by SBI-425 (10 µM). **f**, Instantaneous O_2 consumption rates during the s3-s4 transition from Extended Data Fig. 4e ($n = 4$/group). **g**, Cr-dependent O_2 consumption rates from Extended Data Fig. 4f ($n = 4$/group). **h**, O_2 consumption rates during ADP titration in the absence or presence of SBI-425 (0.2 mM ADP, $n = 4, 0$; 0.4 mM ADP, $n = 4, 4$; 0.5 mM ADP, $n = 6, 4$; 1 mM ADP, $n = 6, 4$; 1.5 mM ADP, $n = 5, 4$; 2 mM ADP, $n = 6, 4$). **i**, Sustained Cr-dependent O_2 consumption rates derived from Extended Data Fig. 4e ($n = 4$/group). **j**, FCC quantified as the TNAP-dependent component of sustained Cr-stimulated respiration derived from Extended Data Fig. 4i ($n = 4$/group). **k**, GDP-inhibitable O_2 consumption rates ($n = 4$/group). Data are presented as mean values ± SEM of biologically independent samples. **b, f**, two-way ANOVA (Fisher's LSD); **c, d, g, i**, two-tailed Student's *t*-tests; **h, k**, non-linear regression.

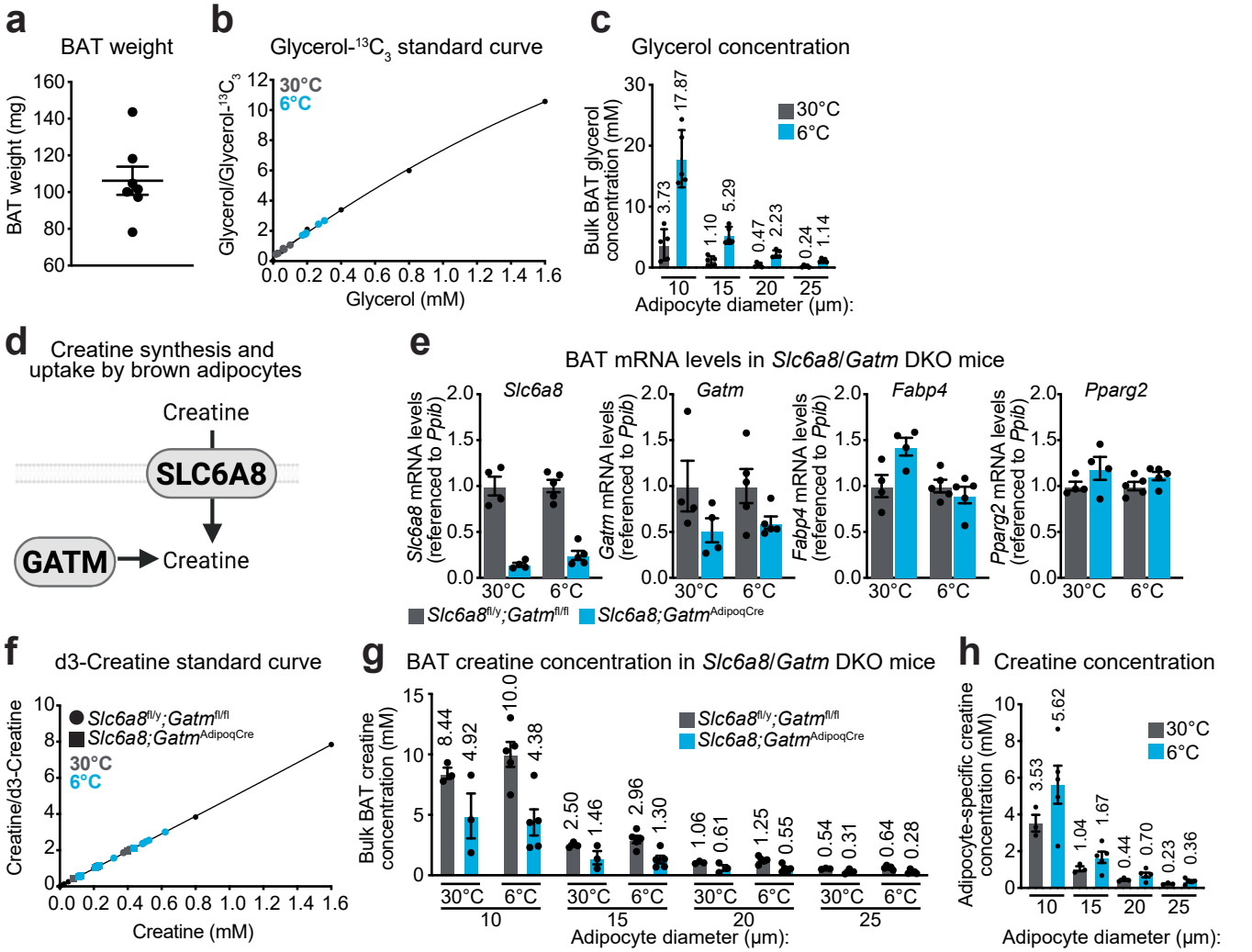

Extended Data Fig. 5 | Glycerol and creatine quantification in interscapular brown adipocytes. a, BAT weights ($n = 7$). **b**, Absolute glycerol quantification in BAT at 30 °C and 6 °C by GC–MS, using Glycerol-$^{13}C_3$ as an internal standard with a glycerol standard curve run in parallel (black circles) ($n = 5$/group). **c**, Brown adipocyte glycerol concentrations within bulk BAT derived from Extended Data Fig. 5b ($n = 5$/group). **d**, Schematic of creatine synthesis and transport in brown adipocytes. Created in BioRender. Kazak, L. (2026) https://BioRender.com/gklaigz. **e**, RT-qPCR of the total BAT RNA from *Slc6a8;Gatm*^{AdipoqCre} double-knockout and *Slc6a8*$^{fl/y}$;*Gatm*$^{fl/fl}$ control mice at 30 °C and 6 °C ($n = 4$ and 5/group). **f**, Absolute creatine quantification in BAT at 30 °C and 6 °C by LC–MS, using d_3-creatine as an internal standard with a creatine standard curve run in parallel (black circles) (30 °C and 6 °C: $n = 3$ and 5/group). **g**, Creatine concentration within bulk BAT of *Slc6a8;Gatm*^{AdipoqCre} double-knockout and *Slc6a8*$^{fl/y}$;*Gatm*$^{fl/fl}$ control mice as a function of adipocyte diameter and brown adipocyte number at 30 °C and 6 °C ($n = 3$ and 5/group). **h**, Brown adipocyte creatine concentrations within bulk BAT calculated from the difference between *Slc6a8;Gatm*^{AdipoqCre} double-knockout and *Slc6a8*$^{fl/y}$;*Gatm*$^{fl/fl}$ control mice in Extended Data Fig. 5g (30 °C and 6 °C: $n = 3$ and 5/group). Data are presented as mean values ± SEM of biologically independent samples.

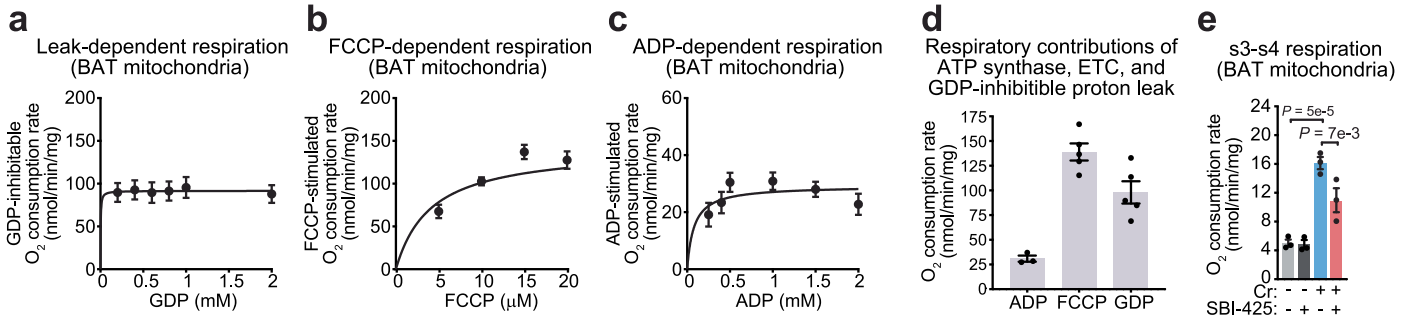

Extended Data Fig. 6 | Leak-, protonophore-, and ADP- stimulated BAT mitochondria respiration. a-c, O_2 consumption rates with titrations of (**a**) GDP (n = 5/group), (**b**) FCCP (n = 5/group), and (**c**) ADP (n = 3/group). **d**, Maximal O_2 consumption rates with ADP, FCCP, and GDP titration (n = 3, 5, and 5/group). **e**, Instantaneous O_2 consumption rates during the s3-s4 transition (n = 4/group). Data are presented as mean values ± SEM of biologically independent samples. **a-c**, non-linear regression; **e**, two-way ANOVA (Fisher's LSD).

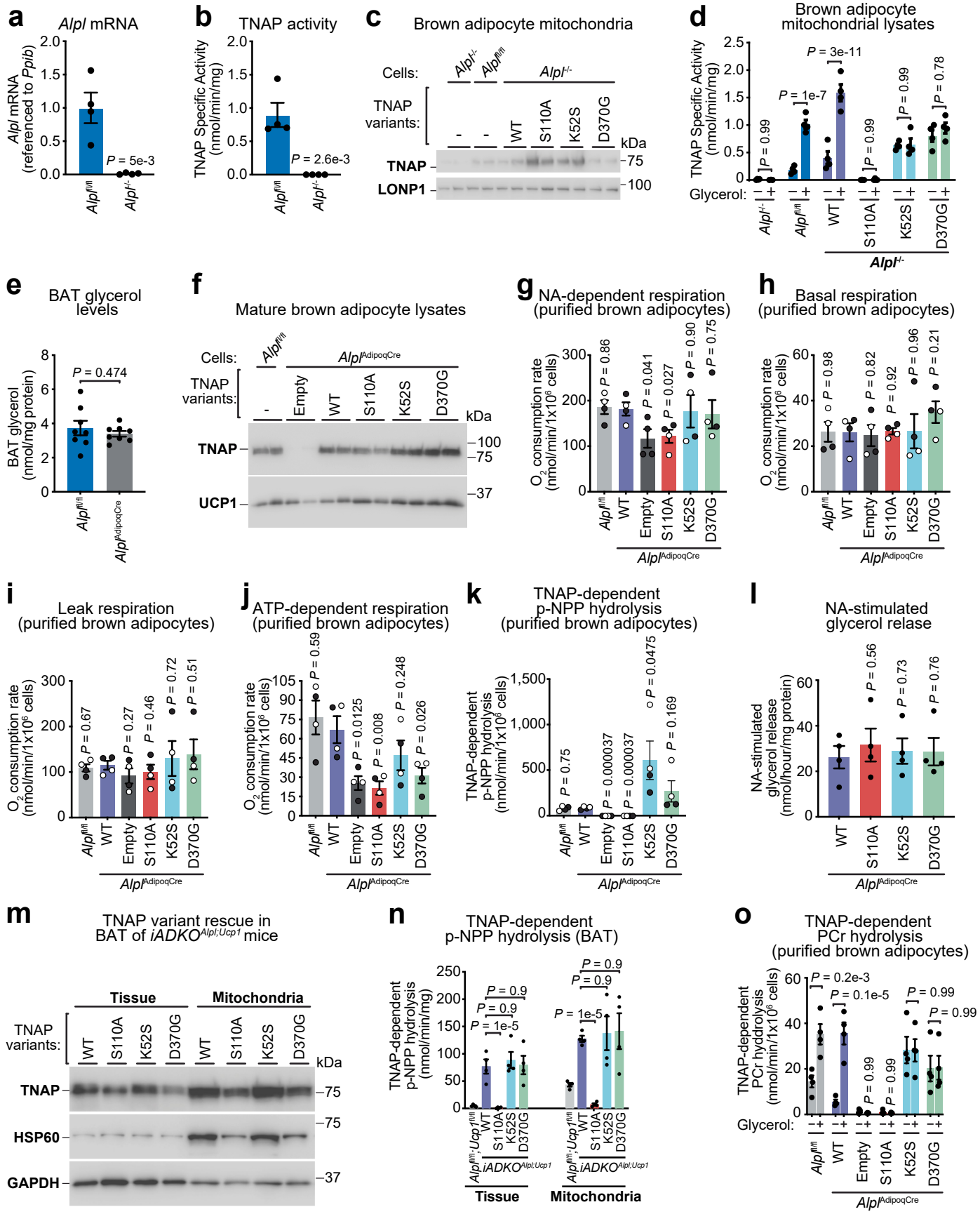

Extended Data Fig. 7 | See next page for caption.

Extended Data Fig. 7 | Contribution of the Glycerol Pocket to FCC-mediated thermogenesis. a, *Alpl* mRNA levels in immortalized brown adipocytes ($n = 4$/group). **b**, TNAP-dependent PCr hydrolysis in whole-cell lysates from immortalized brown adipocytes, defined as the SBI-425–sensitive fraction (10 μM) at pH 7.2 ($n = 4$/group). **c**, Western blot analysis of mitochondrial lysates from *in vitro*-differentiated immortalized brown adipocytes lacking TNAP ($Alpl^{-/-}$), and rescued by adenoviral expression of TNAP variants (WT, S110A, K52S, and D370G). **d**, TNAP-dependent PCr hydrolysis in mitochondrial lysates from $Alpl^{-/-}$ brown adipocytes rescued with TNAP variants, assayed in the absence or presence of glycerol (1 mM) ($n = 4$/group). **e**, BAT glycerol levels in 10–12 week-old male $Alpl^{fl/fl}$ mice or $Alpl^{AdipoqCre}$ mice ($n = 8$/group). **f**, Western blot analysis of mature brown adipocytes from 10–12 week-old male $Alpl^{fl/fl}$ and $Alpl^{AdipoqCre}$ mice rescued with empty AAV or AAV-mediated expression of TNAP variants (WT, S110A, K52S, and D370G). **g**, Basal-subtracted O_2 consumption rates in interscapular brown adipocytes from male (black circles) and female (white circles) mice following noradrenaline stimulation (0.1 μM) ($n = 4$/group). **h**, Basal (unstimulated) oxygen consumption rates in interscapular brown adipocytes ($n = 4$/group). **i**, Basal-subtracted leak respiration, defined as the oligomycin-insensitive (5 μM) component of noradrenaline-stimulated thermogenesis ($n = 4$/group). **j**, Basal-subtracted ATP-linked respiration, defined as the oligomycin-sensitive (5 μM) component of noradrenaline-stimulated thermogenesis ($n = 4$/group). **k**, p-Nitrophenyl phosphate (p-NPP) hydrolysis by TNAP in lysates from rescued mature brown adipocytes. **l**, Noradrenaline-stimulated (0.1 μM) glycerol release from $Alpl^{AdipoqCre}$ BAT restored with AAV-TNAP variants (WT, S110A, K52S, and D370G) ($n = 4$/group). **m**-**n**, (**m**) Western blot analysis and (**n**) TNAP activity in whole-tissue and mitochondrial fractions from tamoxifen-treated control ($Alpl^{fl/fl}$;$Ucp1^{fl/fl}$) and $iADKO^{Alpl;Ucp1}$ male mice expressing AAV-TNAP variants ($n = 4$/group). **o**, TNAP-dependent PCr hydrolysis in interscapular brown adipocyte lysates from $Alpl^{fl/fl}$ or $Alpl^{AdipoqCre}$ mice rescued with TNAP variants, assayed in the absence or presence of glycerol (1 mM) ($n = 4$/group). Data are presented as mean values ± SEM of biologically independent samples. **a, b**, two-tailed Student's *t*-tests; **d, n, o**, two-way ANOVA (Šidák post-hoc test); **e, g-l**, multiple two-tailed Student's *t*-tests.

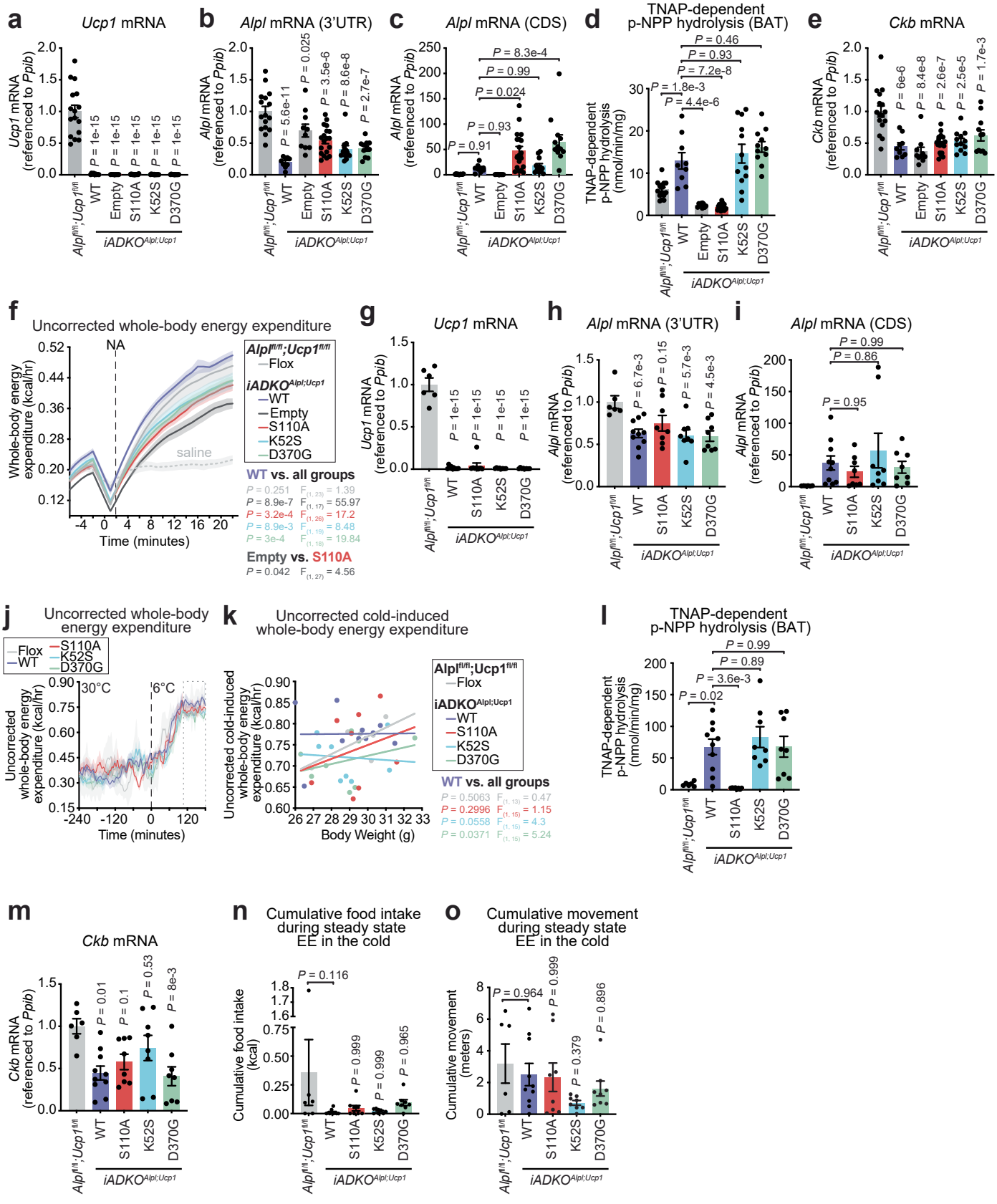

Extended Data Fig. 8 | See next page for caption.

Extended Data Fig. 8 | Genetic TNAP variant restoration in *iADKO*$^{Alpl;Ucp1}$ mice. a-b, Endogenous (**a**) *Ucp1* and (**b**) *Alpl* mRNA levels in tamoxifen-treated control (*Alpl*$^{fl/fl}$;*Ucp1*$^{fl/fl}$: $n = 16$) and *iADKO*$^{Alpl;Ucp1}$ male mice expressing either empty virus (Empty: $n = 10$) or TNAP variants (WT: $n = 9$; S110A: $n = 19$; K52S: $n = 12$; D370G: $n = 11$) acclimated to RT (22 °C ± 1 °C). **c-e**, (**c**) *Alpl* mRNA levels, (**d**) TNAP activity, and (**e**) *Ckb* mRNA levels in BAT from mice in Extended Data Fig. 8a,b. **f**, Uncorrected noradrenaline-stimulated whole-body energy expenditure in 12-week-old male control mice (*Alpl*$^{fl/fl}$;*Ucp1*$^{fl/fl}$, n = 16) and *iADKO*$^{Alpl;Ucp1}$ mice expressing empty AAV, WT TNAP, TNAP(S110A), TNAP(K52S) or TNAP(D370G) (n = 10, 9, 19, 12 and 11, respectively), acclimatized to 22 ± 1 °C. **g-i**, Endogenous (**g**) *Ucp1* and (**h, i**) *Alpl* mRNA levels in tamoxifen-treated control (*Alpl*$^{fl/fl}$;*Ucp1*$^{fl/fl}$: $n = 6$) and *iADKO*$^{Alpl;Ucp1}$ male mice expressing TNAP variants (WT: $n = 10$; S110A: $n = 8$; K52S: $n = 8$; D370G: $n = 8$) acclimated to RT (22 °C ± 1 °C). **j-k**, (**j**) Uncorrected energy expenditure of 12-week-old male control (*Alpl*$^{fl/fl}$;*Ucp1*$^{fl/fl}$: $n = 6$) and *iADKO*$^{Alpl;Ucp1}$ mice expressing TNAP variants (WT: $n = 10$; S110A: $n = 8$; K52S: $n = 8$; D370G: $n = 8$) acclimated to RT (22 °C ± 1 °C) and housed at 30 °C for five days before cold (6 °C) exposure and **(k)** energy expenditure averaged over 100 min steady-state (100–180 min following start of ramp-down to 6 °C). **l-m**, BAT (**l**) TNAP activity and (**m**) *Ckb* mRNA levels in mice from Extended Data Fig. 8g–i. **n-o**, (**n**) Cumulative food intake and (**o**) movement of mice during the final 100 min of cold exposure from Extended Data Fig. 8m. Data are presented as mean values ± SEM of biologically independent samples. **a-e**, One-way ANOVA (Tukey's post-hoc test); **f**, two-way ANOVA (Fisher's LSD); **g-i, l-o**, One-way ANOVA (Tukey's post-hoc test); **k**, analysis of covariance (ANCOVA; two-sided, Bonferroni).

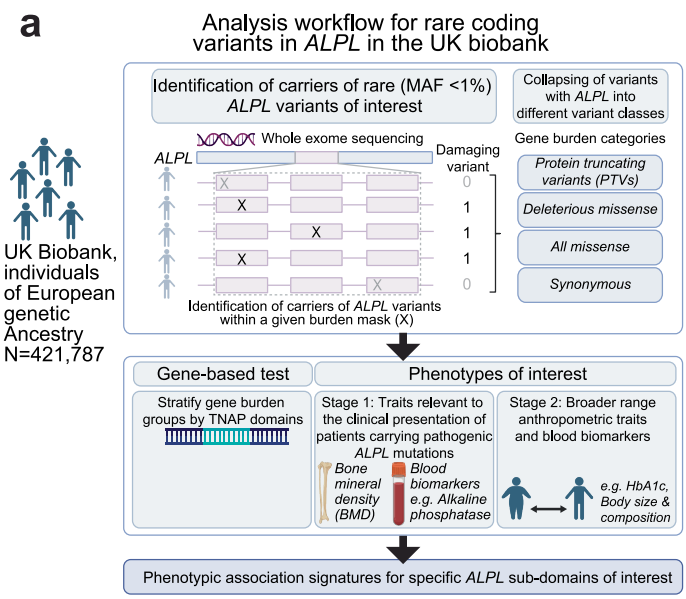

f

Mutations in UKBB and *ALPL* gene variant database

VarID	Position	Amino acid change in the UKBB	Pathogenicity of amino acid change in *ALPL* gene variant database
1:21573763:C:CG	321	R/RX	Not observed
1:21575846:ACT:A	371	T/X	Infantile HPP
1:21560711:C:A	49	N/K	Perinatal HPP
1:21560711:C:G	49	N/K	Perinatal HPP
1:21573763:C:T	321	R/W	Not observed
1:21573764:G:A	321	R/Q	Not observed
1:21573782:T:G	327	F/C	Perinatal HPP
1:21575835:C:T	367	S/F	Not observed

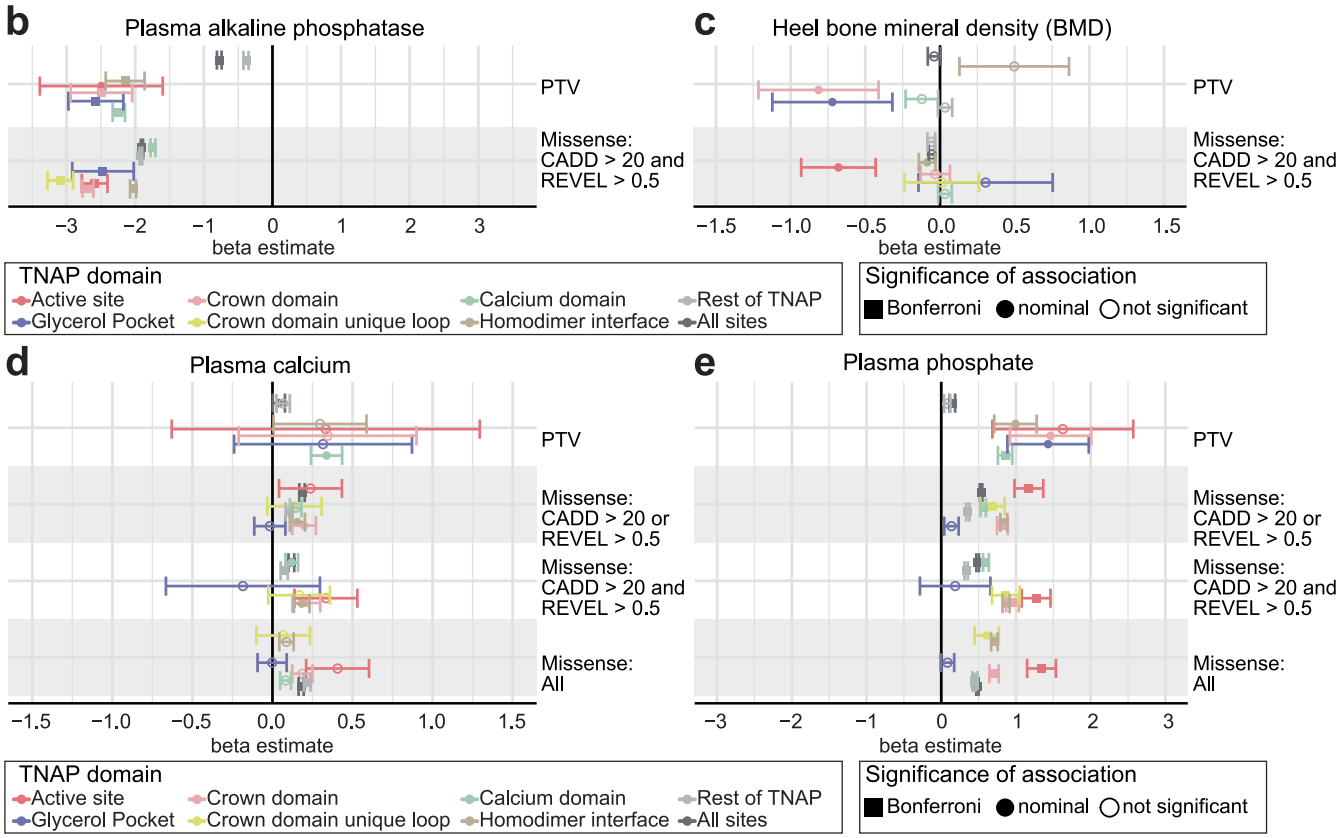

Extended Data Fig. 9 | Pathogenic human *ALPL* variants in the Glycerol Pocket. a, Workflow of our genetic analyses of *ALPL* coding variants in the UKBB. Created in BioRender. Williamson, A. (2026) https://BioRender.com/oe50906. **b-c**, Beta estimates for associations between domain-stratified *ALPL* variant masks (Supplementary Table 6) and (**b**) plasma alkaline phosphatase activity or (**c**) heel bone mineral density (BMD) (alkaline phosphatase: $N = 402{,}160$; heel bone mineral density: $N = 241{,}320$). Variant groupings include protein-truncating variants (PTVs) and three missense masks: (1) CADD > 20 or REVEL > 0.5, (2) CADD > 20 and REVEL > 0.5, and (3) all missense variants without deleteriousness filtering; PTVs and mask 2 are shown here, with masks 1 and 3 shown in Fig. 5a,b. **d-e**, Beta estimates for associations between domain-stratified *ALPL* variant masks and (**d**) plasma calcium or (**e**) plasma phosphate (phosphate: $N = 367{,}874$; calcium: $N = 368{,}088$). **f**, Table showing the position and nucleotide variants in *ALPL* found in the UKBB (VarID, column 1), the amino acid location of the variation in TNAP (Position, column 2), the change in TNAP amino acid sequence as a result of the nucleotide variation (amino acid change, column 3), and the associated phenotypes found in the *ALPL* variant database (https://alplmutationdatabase.jku.at/) from mutations at the sites identified in the UKBB (Pathogenicity of amino acid change, column 4). Not observed indicates variants in the UKBB that were not identified in the *ALPL* variant database. Data are presented as mean values ± SEM of biologically independent samples. In **b-e**, error bars indicate standard error; squares denote associations significant after Bonferroni correction ($P < 0.0016$), filled circles nominal significance ($0.0016 < P < 0.05$), and open circles non-significance ($P > 0.05$).

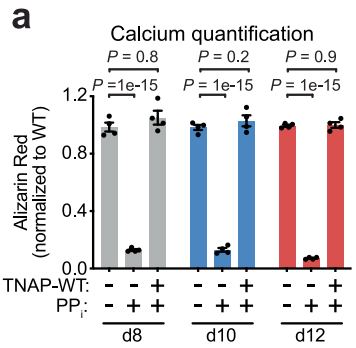

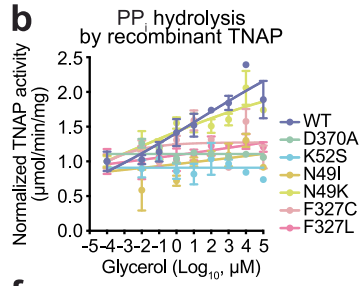

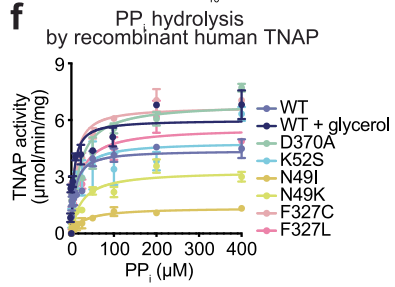

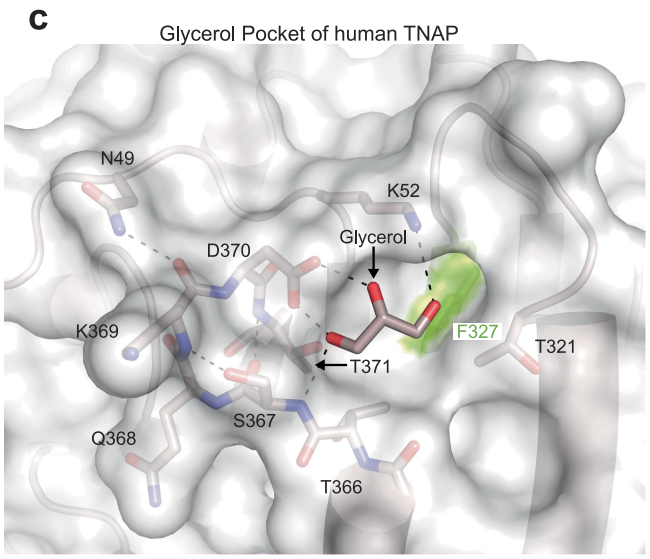

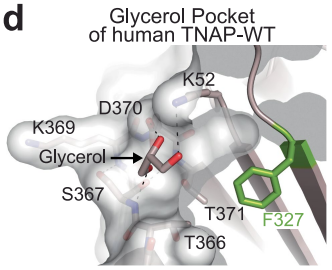

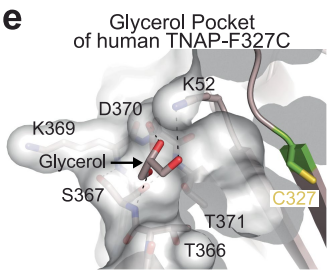

Kinetic parameters of human TNAP

Treatment	K_M (µM)	k_{cat} (s^{-1})	k_{cat}/K_M ($µM^{-1}s^{-1}$)
WT	8.42 ± 2.14	4.39 ± 0.25	0.52 ± 0.12
WT + glycerol	5.82 ± 1.29	6.01 ± 0.28	1.03 ± 0.20
D370A	18.77 ± 5.03	6.89 ± 0.48	0.37± 0.08
K52S	12.37 ± 4.82	4.83 ± 0.45	0.39 ± 0.13
N49I	29.05 ± 9.99	1.37 ± 0.13	0.05 ± 0.01
N49K	24.03 ± 6.09	3.30 ± 0.23	0.14 ± 0.03
F327C	8.67 ± 1.78	6.70 ± 0.31	0.77 ± 0.14
F327L	17.43 ± 4.16	5.58 ± 0.34	0.32 ± 0.06

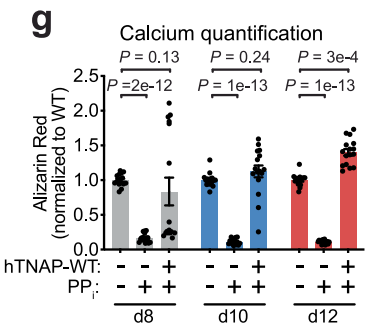

Extended Data Fig. 10 | Pathogenic human TNAP variants activity and mineralization. a, Calcium quantification by Alizarin red staining of osteoblast mineralization following PP_i inhibition and rescue with mouse TNAP-WT ($n = 4$/group). **b**, Glycerol-induced PP_i hydrolysis by recombinant human TNAP-WT, Glycerol Pocket mutants (D370A, K52S), and UKBB variants, normalized to activity at 0 mM glycerol ($n = 3$/group). **c**, Close-up of the Glycerol Pocket in TNAP-S110A bound to PCr and crystallized with glycerol, shown as a semitransparent surface over the ribbon diagram; glycerol and coordinating residues are shown as sticks with hydrogen bonds indicated. **d-e**, Side views of the Glycerol Pocket, as in Extended Data Fig. 10c, illustrating (**d**) closure of the pocket base by F327 and (**e**) and enlargement upon mutation to cysteine. **f**, Michaelis-Menten kinetics of PP_i hydrolysis by recombinant human TNAP-WT, Glycerol Pocket mutants (D370A and K52S), and UKBB variants, with kinetic parameters shown ($n = 3$/group). **g**, Calcium quantification by Alizarin red staining of osteoblast mineralization following PP_i inhibition and rescue with human TNAP-WT ($n = 16$/group). Data are presented as mean values ± SEM of biologically independent samples. **a, g**, two-way ANOVA (Fisher's LSD); **b, f**, linear regression.

nature portfolio

Corresponding author(s): Lawrence Kazak

Last updated by author(s): Feb/11/26

Reporting Summary

Nature Portfolio wishes to improve the reproducibility of the work that we publish. This form provides structure for consistency and transparency in reporting. For further information on Nature Portfolio policies, see our Editorial Policies and the Editorial Policy Checklist.

Statistics

For all statistical analyses, confirm that the following items are present in the figure legend, table legend, main text, or Methods section.

n/a	Confirmed	
☐	☒	The exact sample size (*n*) for each experimental group/condition, given as a discrete number and unit of measurement
☐	☒	A statement on whether measurements were taken from distinct samples or whether the same sample was measured repeatedly
☐	☒	The statistical test(s) used AND whether they are one- or two-sided *Only common tests should be described solely by name; describe more complex techniques in the Methods section.*
☒	☐	A description of all covariates tested
☐	☒	A description of any assumptions or corrections, such as tests of normality and adjustment for multiple comparisons
☐	☒	A full description of the statistical parameters including central tendency (e.g. means) or other basic estimates (e.g. regression coefficient) AND variation (e.g. standard deviation) or associated estimates of uncertainty (e.g. confidence intervals)
☐	☒	For null hypothesis testing, the test statistic (e.g. *F*, *t*, *r*) with confidence intervals, effect sizes, degrees of freedom and *P* value noted *Give P values as exact values whenever suitable.*
☒	☐	For Bayesian analysis, information on the choice of priors and Markov chain Monte Carlo settings
☒	☐	For hierarchical and complex designs, identification of the appropriate level for tests and full reporting of outcomes
☒	☐	Estimates of effect sizes (e.g. Cohen's *d*, Pearson's *r*), indicating how they were calculated

Our web collection on statistics for biologists contains articles on many of the points above.

Software and code

Policy information about availability of computer code

Data collection	QPCR: CFX Maestro 2017 Mitochondrial respiration: Rank Brothers Dual Digital model 20: Picolog 6 data logging software TNAP activity: BioTek Synergy H1 plate reader in kinetic mode Western blots: Chemidoc Imaging system (Bio-Rad) Glycerol concentrations by GC-MS: Agilent 5975C GC/MS equipped with a DB-5MS+DG (30 m x 250 µm x 0.25 µm) capillary column (Agilent J&W, Santa Clara, CA, USA). Creatine concentrations by LC-MS: Triple quadrupole mass spectrometer (QQQ 6470) equipped with a 1290 ultra high-pressure liquid chromatography system (Agilent Technologies, Santa Clara, California, USA). Online protein digestion was performed using an Affipro pepsin. Mass spectra for HDX-MS were analyzed using a Waters- SELECT SERIES Cyclic IMS operated in HDMS. The peptides identified in PLGS were then analyzed in DynamX 3.0 (Waters Corporation). Peptides meeting initial filtering criteria were further processed by DynamX 3.0. Alizarin red staining was measured using a spectrophotometer (Tecan INFINITE 200 PRO). Von Kossa staining was recorded using an Epson Perfection 2400 Photo scanner. No software was used for data collection for the population genetics analyses described.
Data analysis	GraphPad Prism, 10 Microsoft office Excel (v.16.78) MestReNova (v.14.2.1) was used for NMR data processing and analysis GC-MS and LC-MS analysis: MassHunter Quant (Agilent Technologies, version 10.0, build 10.0.707.0).

Sable Systems Macro Interpreter v23.6.0
Sable Systems 1 minute One - Click Macro (v.2.53.2)
Genetics analyses in UK Biobank: The code for the analyses of UK Biobank data included in this manuscript is freely available via GitHub https://github.com/comp-med/tnap-alpl-ukb and permanently archived via Zenodo at DOI: https://doi.org/10.5281/zenodo.18606385.
Software used: PLINK2 (v2.00a3.1LM), Regenie (v3.1.1). Analyses were run via the Swiss Army Knife tool (v4.9.1) provided by DNAnexus on the UK Biobank Research Analysis Platform.

For manuscripts utilizing custom algorithms or software that are central to the research but not yet described in published literature, software must be made available to editors and reviewers. We strongly encourage code deposition in a community repository (e.g. GitHub). See the Nature Portfolio guidelines for submitting code & software for further information.

Data

Policy information about availability of data

All manuscripts must include a data availability statement. This statement should provide the following information, where applicable:

- Accession codes, unique identifiers, or web links for publicly available datasets
- A description of any restrictions on data availability
- For clinical datasets or third party data, please ensure that the statement adheres to our policy

Availability statement:
All data supporting the findings of this study are available within the paper and its Supplementary Information. Any additional information required to reanalyze the data reported in this paper is available from the lead contact upon request. Atomic coordinates and structure factors have been deposited in the Protein Data Bank with accession codes 10TV (TNAP - S110A with PCr and glycerol), 10TW (TNAP - D370G with glycerol), 10TX (TNAP - S110A with PP i and glycerol), 10TY (TNAP - S110A with PPi and ethylene glycol), 10TZ (TNAP - S110A with ATP and glycerol). HDX mass spectrometry proteomics data have been deposited to the ProteomeXchange Consortium via the PRIDE partner repository with the dataset identifier PXD067887. All individual - level data in the UK Biobank study are publicly available to bona fide researchers through the UK Biobank data access protocol. Information about registration for access to the data is available at: https:// www.ukbiobank.ac.uk/enable - your - research/apply - for - access. The code for the analyses of UK Biobank data included in this manuscript is freely available via GitHub (https://github.com/comp - med/tnap - alpl - ukb) and permanently archived via Zenodo at https://doi.org/10.52 81/zenodo.18606385. All analyses in UK Biobank in this manuscript were conducted under application # 44448.

Research involving human participants, their data, or biological material

Policy information about studies with human participants or human data. See also policy information about sex, gender (identity/presentation), and sexual orientation and race, ethnicity and racism.

Reporting on sex and gender	In UK Biobank sex-combined analyses were used as the primary results, with sex included as a covariate. Sex-stratified analyses were also run as a sensitivity analysis to identify if there were any sex-differential effects.
Reporting on race, ethnicity, or other socially relevant groupings	Genetic analyses in UK Biobank were restricted to individuals of European genetic ancestry, derived from genotype array data. This represents the majority of participants in the study. We were not powered to investigate genetic associations of rare variants identified by WES in other ancestry groups in this study, due to small sample sizes for rare variant analysis.
Population characteristics	Population characteristics – UK Biobank UK Biobank is a prospective cohort study from the UK that contains more than 500,000 volunteers between 40 and 69 years of age at point of enrolment (baseline study visit). The cohort has been extensively described elsewhere (www.ukbiobank.ac.uk). Individuals included in this analyses were not directly selected for inclusion in the study on the basis of any disease or health parameter. Additional details of UK Biobank can be found via the following link: https:// www.ukbiobank.ac.uk/
Recruitment	UK Biobank: all people aged 40-69 years who were registered with the National Health Serivce and living up to 25 miles from one of the 22 study assessment centers were invited to participate in 2006-2010. Overall about 9.2 million invitations were mailed to recruit 503,325 participants (a response rate of 5.47%). The individuals in this study are known to be healthier than the general population which may lead to an underestimation of effect sizes for certain phenotypes (e.g. obesity).
Ethics oversight	UK Biobank had obtained ethics approval from the North West Multi-centre Research Ethics Committee which covers the UK (approval number: 11/NW/0382). All UK Biobank paricipants give written informed consent. All study procedures were performed in accordance with the World Medical Association Declaration of Helsinki ethical principles for Medical research. All analyses in this manuscript were conducted under a UK Biobank approved application for use of the data (application ID 44448).

Note that full information on the approval of the study protocol must also be provided in the manuscript.

Field-specific reporting

Please select the one below that is the best fit for your research. If you are not sure, read the appropriate sections before making your selection.

☒ Life sciences ☐ Behavioural & social sciences ☐ Ecological, evolutionary & environmental sciences

For a reference copy of the document with all sections, see nature.com/documents/nr-reporting-summary-flat.pdf

Life sciences study design

All studies must disclose on these points even when the disclosure is negative.

Sample size	Sample sizes were predetermined based on effect size, standard deviation, and significance level required to attain statistical significance of p<0.05 with a 90% probability on the basis of previous experiments using similar methodologies and were deemed sufficient to account for any biological/technical variability (PMIDs: 31161155, 30078553, 28844881, 24439384). For experiments without predetermination, sample sizes were chosen on the basis of prior experience and published standards in the field (see PMIDs above). Sample sizes are indicated for each experiment in the manuscript. For genetic analyses in UK biobank: all individuals of European genetic ancestry with available sequencing and genotype array data, and a given trait of interest were included in the analysis (N max = 421,787). We were sufficiently powered to detect several associations at a Bonferroni corrected significance threshold.
Data exclusions	No data were excluded For genetic analyses in UK biobank: individuals who did not have genotype/WES data, were ancestry outliers or not of European ancestry were excluded from the analysis. Variants which did not meet QC cut offs were also excluded from the analysis (see methods for details).
Replication	All attempts of replication were successful. Sample sizes for each experiment are reported in the figure legends. Western blots represent independent biological samples. For genetic analyses in UK biobank: we used all data available for discovery and therefore no replication was attempted to allow use of the maximum sample size to detect associations in the discovery
Randomization	Samples were processed in randomized order where feasible, and quantification was performed using predefined, objective criteria to minimize potential bias. In particular, for in vivo studies, mice in each genotype were randomly assigned to treatment groups. For cell-based experiments, cells were randomly seeded from a common plating source and subsequently allocated to treatment conditions to ensure comparable baseline characteristics across groups. For respirometry experiments, samples were processed in random order across multiple oxygen electrodes. For genetic analyses in UK Biobank: natural randomization is expected, since genetic variants are the exposure.
Blinding	Investigators were not blinded to experimental conditions, as the procedures required knowledge of group assignments for appropriate treatment administration. Outcome measures, including respirometry, X-ray crystallography, western blotting, enzyme kinetics, and RT-qPCR were obtained using automated, highly objective methodologies. In other experiments, blinding was not feasible because the same individual conducted and analyzed the experimental work. For genetic analyses in UK Biobank: genetic association analyses do not require blinding.

Reporting for specific materials, systems and methods

We require information from authors about some types of materials, experimental systems and methods used in many studies. Here, indicate whether each material, system or method listed is relevant to your study. If you are not sure if a list item applies to your research, read the appropriate section before selecting a response.

Materials & experimental systems

n/a	Involved in the study
☐	☒ Antibodies
☐	☒ Eukaryotic cell lines
☒	☐ Palaeontology and archaeology
☐	☒ Animals and other organisms
☒	☐ Clinical data
☒	☐ Dual use research of concern
☒	☐ Plants

Methods

n/a	Involved in the study
☒	☐ ChIP-seq
☒	☐ Flow cytometry
☒	☐ MRI-based neuroimaging

Antibodies

Antibodies used

VCL (Cell Signaling, cat#13901, 1:5000, clone E1E9V)
total-OXPHOS (Abcam, cat# ab110413, 1:200)
FLAG (Cell Signaling, 2368, 1:1000)
TOM20 (Santa Cruz, sc-11415, 1:4,000)
TOM70 (Santa Cruz, cat# sc-390545, 1:1000, clone A-8)
Calnexin (Abcam, cat# ab22595, 1:4000)
PMP70 (Abcam, cat# ab3421, 1:500)
UCP1 (Abcam, ab10983, 1:2000)
CKMT2 (Abcam, cat# ab189314, 1:1000)
TNAP (R&D Systems, cat#AF2910, 1:200)
TIM23 (BD Biosciences; cat. no. 611222, 1:200, clone 32)
LONP1 (Abcam, cat no. Ab103809, 1:1500)
CKB (Abclonal; cat. no. ab12631; 1:1,000)

HSP60 (Abcam, cat no. Ab46798, 1:10000)
anti-rabbit HRP (Promega; cat. no. W4011)
anti-mouse HRP (Promega; cat. no. W4021)
anti-goat HRP (Promega; cat. no. V8051)

Validation

All antibodies are commercial in origin. Validation statements can be found on the manufacturer's website for the following:

VCL (Cell Signaling; Cat. No. 13901; clone E1E9V): https://www.cellsignal.com/products/primary-antibodies/vinculin-e1e9v-xp-rabbit-mab/13901
FLAG (Cell Signaling, 2368, 1:1000): https://www.cellsignal.com/products/primary-antibodies/dykddddk-tag-antibody-binds-to-same-epitope-as-sigma-aldrich-anti-flag-m2-antibody/2368?srsltid=AfmBOorvZqHsnUBh7wFkTE9AH8b8dZ6-9ivGTZejXjIqinGvlXD-9Unl
TOM20 (Santa Cruz, sc-11415, 1:4,000): https://www.scbt.com/p/tom20-antibody-fl-145?srsltid=AfmBOoro2Tzt7ULhgZOKPYuDzDR5xlTYP_RknUYudWn0hYdrVHsEoJ5r
TOM70 Santa Cruz, cat# sc-390545, 1:1000, clone A-8) https://www.scbt.com/p/tom70-antibody-a-8: https://www.scbt.com/p/tom70-antibody-a-8
Calnexin (Abcam, cat# ab22595, 1:4000 : https://www.abcam.com/en-us/products/primary-antibodies/calnexin-antibody-er-marker-ab22595
PMP70 (Abcam, cat# ab3421, 1:500) : https://www.abcam.com/en-us/products/primary-antibodies/pmp70-antibody-ab3421
UCP1 (Abcam; Cat. No. ab10983): https://www.abcam.com/ucp1-antibody-ab10983.html
CKMT2 (Abcam, cat# ab189314, 1:1000) : https://www.abcam.com/en-us/products/primary-antibodies/ckmt2-antibody-ab189314
TNAP (R&D; cat. no. AF2910): https://www.rndsystems.com/products/mouse-alkaline-phosphatase-alpl-antibody_af2910
LONP1 (Abcam, cat no. Ab103809, 1:1500) : https://www.abcam.com/en-us/products/primary-antibodies/lonp1-lon-antibody-ab103809
CKB (Abclonal; Cat. No. ab1263): https://abclonal.com/catalog-antibodies/CKBPolyclonalAntibody/A12631
HSP60 (Abcam, cat no. Ab46798, 1:10000) : https://www.abcam.com/en-us/products/primary-antibodies/hsp60-antibody-mitochondrial-marker-ab46798

Eukaryotic cell lines

Policy information about cell lines and Sex and Gender in Research

Cell line source(s)

Immortalized brown adipocytes generated in-house, MC3T3-E1, subclone 14

Authentication

Immortalized brown adipocytes were authenticated based on the capacity to differentiate into lipid-laden fat cells. MC3T3-E1, subclone 14 were authenticated based on capacity to differentiate into osteoblasts with a collagenous mineral matrix, see PMID: 25460184 (https://pmc.ncbi.nlm.nih.gov/articles/PMC6342200/) for additional details on this cell line.

Mycoplasma contamination

Cell lines were not tested for mycoplasma.

Commonly misidentified lines
(See ICLAC register)

No commonly misidentified cells were used in this study.

Animals and other research organisms

Policy information about studies involving animals; ARRIVE guidelines recommended for reporting animal research, and Sex and Gender in Research

Laboratory animals

Mouse experiments were performed according to procedures approved by the Animal Resource Centre at McGill University and complied with guidelines set by the Canadian Council of Animal Care. Mice were born and housed in groups of 3–5 per cage at 22ºC +/- 1ºC until experimental intervention (at 6–12 weeks old). The photoperiod was fixed at 12 hours:12 hours with lights on at 0700 hours, and the mice had ad libitum access to drinking water and a low-fat diet (2920X, Envigo, Madison, WI, USA) at 40–60% humidity. WT C57BL/6N mice were purchased from Charles River Laboratories (strain code: 027). AdipoqCre mice (B6;FVB-Tg(AdipoQ-Cre)1Evdr/J), stock 028020), maintained on a C57BL/6J background, were bred with Slc6a8fl/fl or Slc6a8fl/y mice and Gatmfl/fl mice to generate Slc6a8;Gatm double-knockout male mice (Slc6a8;GatmAdipoqCre) and control (Slc6a8fl/y;Gatmfl/fl) male mice. Adipocyte-selective Alpl knockout mice (AlplAdipoqCre) have been described previously. Ucp1fl/fl (B6(129S4)-Ucp1tm1c(EUCOMM)Hmgu/KazlJ) are available at the Jackson Laboratory Repository with the Jax Stock No. 039539 (http://jaxmice.jax.org/query). Alplfl/+ mice3 were mated to Ucp1fl/+ mice to generate Alplfl/fl;Ucp1fl/fl mice, which were then crossed to AdipoqCreERT2 mice (C57BL/6N, Jax Stock No. 025124) to generate: (1) inducible adipocyte-selective Alpl;Ucp1 double knockout mice (iADKOAlpl;Ucp1) and (2) control floxed mice (Alplfl/fl;Ucp1fl/fl). Mouse experiments used age-matched littermates. For GC-MS and LC-MS analyses, 6 - 8-week-old mice were singly housed at 30ºC or 6ºC for 3 weeks in cages with ad libitum access to drinking water and a chow diet. Mice were euthanized by cervical dislocation and tissues were processed for mitochondrial isolation or immediately flash-frozen in liquid nitrogen and stored at -80ºC until further analysis.

Wild animals

The study did not involve wild animals.

Reporting on sex

Sex was not considered in the study design. Sex was considered in the phenotypic associations in the UKBB.

Field-collected samples

The study did not involve samples collected from the field.

Ethics oversight

Animal experiments were performed according to procedures approved by the Animal Resource Centre at McGill University and complied with guidelines set by the Canadian Council of Animal Care.

Note that full information on the approval of the study protocol must also be provided in the manuscript.

Plants

Seed stocks	*Report on the source of all seed stocks or other plant material used. If applicable, state the seed stock centre and catalogue number. If plant specimens were collected from the field, describe the collection location, date and sampling procedures.*
Novel plant genotypes	*Describe the methods by which all novel plant genotypes were produced. This includes those generated by transgenic approaches, gene editing, chemical/radiation-based mutagenesis and hybridization. For transgenic lines, describe the transformation method, the number of independent lines analyzed and the generation upon which experiments were performed. For gene-edited lines, describe the editor used, the endogenous sequence targeted for editing, the targeting guide RNA sequence (if applicable) and how the editor was applied.*
Authentication	*Describe any authentication procedures for each seed stock used or novel genotype generated. Describe any experiments used to assess the effect of a mutation and, where applicable, how potential secondary effects (e.g. second site T-DNA insertions, mosiacism, off-target gene editing) were examined.*